ALMA MATER STUDIORUM - UNIVERSITÀ DI BOLOGNA

SCUOLA DI INGEGNERIA E ARCHITETTURA

CIVIL, CHEMICAL, ENVIRONMENTAL AND MATERIALS ENGINEERING - DICAM

SECOND CYCLE DEGREE IN CIVIL ENGINEERING (LM-23)

Dissertation
In
Structural Safety

Design, Fabrication and Mechanical Characterization studies on Wire-and-Arc Additively Manufactured (WAAM) diagrid elements

CANDIDATE
Lidiana Arrè

SUPERVISOR
Prof. Tomaso Trombetti

CO-SUPERVISORS
Prof. Michele Palermo
Prof. Vittoria Laghi
Prof. Harald Kloft

Academic year 2020-2021
Session III

Table of Contents

List of Figures

List of Tables

1. Introduction

The design approach changed in the last decades, firstly with the innovation offered by software for Computer-Aided Design (CAD), to replace manual drawings, and Building Information Modelling (BIM), therefore not bringing to a change in the architectural shapes. We had to wait until the early years of the 21st century, when new forms were found by means of three-dimensional computer modelling and digital fabrication methods. New complex forms are now feasible and applicable in architectural, civil and structural engineering (Carpo 2013), resulting in free-form designs and shell structures (Adriaenssens 2014). Moreover, the topology optimization is an effective computational method for the design of efficient structures (S. L. Thomas 2021), with also the implementation of periodic design in which a single unit-cell is optimized and then replicated to form a larger periodic structure (X. X. Huang 2008).

The growth of automatic processes in the building construction sector is still at the beginning compared to other sectors. The challenge is due to the aim of building large-scale structures, which require the customization of conventional automated fabrication technologies, in addition, it is necessary to change the conventional design approaches (Khoshnevis 2004). The development in digital fabrication techniques is leading to the application of automatic processes in structural engineering sector, through Additive Manufactured (AM) based technologies, already commonly used in other sectors such as aerospace, automotive and biomedical engineering (Attaran 2017), (C. G. Thomas 1996), (Song 2015), (Giannatsis 2009). It offers numerous benefits over conventional manufacturing methods, such as greater structural efficiency, geometric freedom, customization, engineered material properties, reduced material usage, lessened construction waste, shortened build times and reduced transportation costs, along with the potential for repairing and strengthening opportunities. The construction sector is coming under increasing pressure from rapid urbanization, climate change and resource scarcity leading to a desire for more efficient construction techniques (C. G. Buchanan 2019). AM is expected to become a key manufacturing technology in the sustainability society of the future (S. L. Huang 2013).

The term Additive Manufacturing (AM) has been attempted to be standardized in ISO/ASTM 52900 (International 2015), where the general term has been adopted for all processes of making parts from 3D models and materials.

AM enables the design of more complex and optimized components due to greater freedoms in shape and geometry, along with simpler assemblies comprising fewer both parts and different materials. The free-form and lightweight structures are often inspired by nature and draw on biomimicry concepts. The benefits that can be realized occur over the whole life-cycle of the product and its materials. Examples of product improvements include greater operational efficiency, functionality and durability, and ease of manufacturing and maintenance (Despeisse 2015). The construction sector is a major material, energy and water consumer, consequently, it presents significant opportunities for resource efficiency improvements (Buyle 2013). Demonstrations of in-situ construction, such as the MX3D bridge, 3D Print Canal House and 3D printed apartment buildings in China, show what is becoming possible using AM techniques. This means that fewer materials can be brought to and from the construction site, also reducing waste overheads. The shift from a centralized system of manufacturing to a more decentralized one implies that the environmental impact of transportation will be reduced.

The economics of AM make it ideal for make-to-order component and product manufacturing, allowing production of spare parts for replacement, and lower cost customization and personalization. From a sustainability perspective, the additive nature of AM makes it a more resource efficient manufacturing process as less waste is generated compared to subtractive techniques. In addition, the non-processed raw materials can be recycled and re-used by AM. Even if, AM is more energy intensive per unit produced (relative performance), AM allows units to be produced to exactly match the demand (make-to-order) and thus offers the potential for better absolute performance (Ford 2016).

The workflow process of the methods related to AM consists of: firstly, a 3D CAD model is created; then, it is sliced into a series of building layers; this information is then sent to the processing machine, defining the location of the building head; and finally, the part is built up layer-by-layer. Today a wide range

of materials can be used in additive manufacturing processes including ceramics, chemicals, composites, concrete, foodstuffs, metallic materials, paper, plastics, sandstone, silicones, wax and wood (Gao 2015), (Symes 2012), (Wong 2012).

Several additive manufacturing applications in the construction sector are already realized, focusing the attention on concrete, polymer and metal ones. They are presented to demonstrate the viability of 3D printing at construction scale.

Firstly, the concrete is the most widely used material in construction, however the concrete additive manufacturing techniques offer opportunities for significant cost savings, highlighting the scaffolding high cost. Examples are: Winsun residential and office buildings (2016) with the walls built in a factory, then the components were assembled on site on traditional foundations with additional steel; Castilla-La Mancha 3D Bridge (2016), pedestrian bridge near Madrid in Spain; Gemert bicycle bridge (2017) in Netherlands, first 3D printed prestressed concrete bridge, which was built in parts and then joined together onsite; the FreeFAB process, in which the molds are built from wax and then concrete is applied using conventional techniques, and molds can be removed after the concrete hardening to be recycled. The lessons learnt from the concrete additive manufacturing may be put into practice in metal AM, such as the offsite manufacture to use the equipment in a more controlled environment and reduce the time and labor requirements onsite, the recycling of unused material, and the ability to produce new geometric forms. Current studies and applications of structural optimization for new classes of 3D printing concrete elements have been developed by Vantyghem et al. (Vantyghem 2020), as well as by ETH Zurich research team (Anton 2019).

Secondly, the polymer additive manufacturing in construction is typically limited to mechanical and electrical systems and facades, an example is the 3D Print Canal House in Amsterdam, Netherlands, made of polypropylene blocks.

Lastly, the metal additive manufacturing in construction has been experienced primarily on small-scale components such as façade nodes and connections, nevertheless a pioneering project is the full size MX3D 3D-printed steel pedestrian bridge. (i) The façade nodes often feature complex geometries, however the AM processes allows more optimized geometries with geometric freedom; the topology optimization is exploited to manufacture lighting nodes, showing that metal AM

can enable efficient structural forms that would be excessively time consuming and costly to manufacture with traditional forming techniques. (ii) The MX3D bridge is the first example of optimized shape manufactured using WAAM process (among the metal AM ones) (MX3D Webpage), awarded at the Dutch Design Week held in Eindhoven in October 2018, which exhibits that metal 3D printing is possible at a scale suitable for construction applications. Other explorations on innovative structural elements have been also carried out at University of Technology Darmstadt (Feucht 2020).

The current research comprises the overarching process, from the computational design to the mechanical characterization of the WAAM-produced elements. In the first part, the research was carried out at Technische Universität Braunschweig, Institut für Tragwerksentwurf, with the support of the institute director, Dr.-Ing. Harald Kloft, within the project A07 led by Dipl.-Ing. Christoph Müller, focused on "Wire-and-Arc Additive Manufacturing (WAAM) of complex individualized steel components". It was focused on the computational design and fabrication stages: starting from the digital model created with Rhinoceros software (Rhinoceros 5) up to the manufacturing phase by means of Universal Robot (UR16e) robotic arm, Fronius TPS 600i PULSE power source and ER70S-6 carbon steel wire. The outcomes are rod-like elements realized using the "dot-by-dot" printing strategy.

Afterwards, the second part was carried out at University of Bologna, where the work presented in this thesis represents a step of a wider campaign carried out on the WAAM "dot-by-dot" printed elements to assess their mechanical parameters taken into account for structural design and verification.

2. Wire-and-Arc Additive Manufacturing (WAAM)

The focus of this research is on the metal additive manufacturing methods, the metallic elements are produced by means of one of the processes, classified as:

(i) Powder Bed Fusion (PBF),
(ii) Directed Energy Deposition (DED),
(iii)Sheet lamination.

Each process has its own limitations and characteristics, such as the maximum built part size and the building speed (Williams 2016).

First applications of metal AM in construction used PBF technology, limited to realize ad-hoc parametrically designed joints (Galjaard 2015), (Raspall 2019), due to atmosphere requirements, which has implications on the building space size (enclosed in a box of typically 250-mm side), consequently the geometrical constraints influence the maximum dimensions of a single part (C. M. Buchanan 2017).

Nevertheless, the current research adopts the Directed Energy Deposition (DED) method, in particular the Wire-and-Arc Additive Manufacturing (WAAM) technique, which best suits the possibility to realize large-scale metal parts and to allow new geometric forms. This technique uses arc welder as a power source and welding wire as feedstock to build up a component. The motion system can be either a robotic system or a computer numerical controlled gantry. The WAAM hardware uses mainly welding equipment, which allows for a relatively fast (when compared to the other AM processes) large-scale production (up to few meters span), onsite fabrication, and relatively low costs for wire material and setup. Gas Metal Arc Welding (GMAW) has been established as a process for material deposition due to its comparable high deposition rates, about 4-9 kg/h. Notably, controlled short circuiting processes such as cold metal transfer (CMT) from welding manufacturer Fronius, and others, are applied, in order to control the wire deposition with reduced heat input (Heimig 2020). The temperature must be controlled to ensure suitable deposition conditions, allowing cooling during building. The manufacturing technique inherently produces a rough surface, therefore the surface finish may require additional post-processing.

The printing deposition strategies are:

- “continuous” printing, consisting in the layer-by-layer deposition strategy, suitable for planar and shell-like geometries;
- “dot-by-dot” printing, consisting in a spot-like deposition strategy, whose outcomes are metal rods suitable to realize grid shells and lattice structures.

The present work is based on the “dot-by-dot” printing strategy in which the steel wire is melted to create three-dimensional elements. WAAM-produced elements are realized through successive deposition of metal droplets on a discontinuous process along one axis (Joosten 2015), (Van Bolderen 2017), developing 3D one-dimension rod-like elements with a certain build direction (longitudinal main axis) and having a constant nominal diameter (within the range of 4 to 8 mm) related to the welding dot.

A linear (non-recursive) workflow is the most common way of robotic control: firstly, it begins with a design and its 3D representation, then, the robotic tool-path planning is derived from this digital product model, including the integration of additional tools such as welder power sources, finally, the robotic path is translated into machine code which controls the execution of the robot process (Snooks 2016). The enhancement is the change from linear to adaptive (recursive) workflows, where processes are constantly measured to dynamically inform following actions: sensors interpret processes, computer calculates the next appropriate robotic action, robot actuates the actions. This is necessary to deal with the growing demand for automated solutions capable of adapting dynamically to the change of processes, materials, factory environments and onsite conditions.

There is still limited research focused on the characterization of WAAM-produced metal elements for structural engineering applications, hence the research teams at University of Bologna and at ETH Zürich are both working to assess the geometrical, mechanical and microstructural properties of elements realized by means of different materials, such as stainless steel and carbon steel elements (V. P. Laghi 2020b), (V. P. Laghi 2020c), (V. P. Laghi 2019), (Silvestru 2021).

Effort is required to completely characterize the geometrical and mechanical features of the 3D-outcomes, pointing up the influence of surface roughness and imperfections on the mechanical response, with the aim to achieve a structural

design and verification of WAAM-produced elements. This is due to the different mechanical response of WAAM material with respect to the one of the corresponding wrought.

The WAAM printing process parameters are properly defined due to their influence on the microstructure, geometrical and mechanical properties of the printed outcomes (Wu 2019), (DebRoy 2018), (B. P. Wu 2018), (Ryan 2018), (Wang 2016), (Kim 2003), (Guan 2013), (Liberini 2017), (Xiong 2018). The manufacturing process requires high velocity to realize large-scale structures, resulting in non-negligible geometrical irregularities (cross-sectional variation and lack of straightness) to be considered. The proper process parameters are based on the type of outcomes, such as their length and inclination. In this direction, also other researchers at TU Braunschweig are working on the design and parametric identification of WAAM steel bars for use in construction (Müller 2019).

3. Structural design approaches for WAAM elements

Recently, the structural design workflow integrated also the use of the computational design concept, which refers to the use of computations for the exploration of structural solutions and the development of novel design ideas.

Within computational design framework, different approaches have been proposed so far. Cascone et al. recently proposed a structural grammar approach for the generative design of diagrid-like structures (Cascone 2021). A similar concept has also been adopted to realize a WAAM diagrid column (V. P. Laghi 2020a). Generative design has also been used by Wang et al. in an integrated method to create joints for tree-like columns to be realized in AM (H. D. Wang 2021). Alternatively, topology optimization algorithms have been implemented to consider the features proper of AM process (Saadlaoui 2017), (W. M. Wang 2020).

On the other hand, a "blended" structural optimization approach is proposed, in order to integrate the capabilities of optimization procedures in terms of new structural shapes with the limitations of the current stage of development of WAAM technology (i.e. manufacturing constraints, printing precision and material properties) together with the robustness and reliability of structural design verifications. Indeed, the approach is intended to "blend" a stiffness-based topology optimization approach (suitably tailored for WAAM stainless steel, see e.g. (Bruggi 2021)) with basic principles of structural design in terms of conceptual design and structural solutions to conceive an initial design, together with concepts of robustness and reliability to guide the designer from the purely mathematically optimized solutions toward the final design. In fact, the optimized designs need to comply with the manufacturing constraints proper of WAAM process, and then to be structurally verified through numerical simulations and an iterative process towards the final design. A "blended" structural optimization approach may be conveniently used to investigate effective solutions in an efficient way.

4. Computational design of a diagrid column

4.1. Overview

The “Innocenti” tube is well known in the construction sector, although this metal structure is realized with hollow section and constant thickness, determining an excess of used material. In addition, the structural elements present nodes realized by means of bolting or welding, using additional materials and components, resulting to be critical points of the structure, which require additional effort in the construction phase. Therefore, the innovation is represented by an innovative reticular pole realized with 3D printing technique, which has an “atomized” tubular cross-section, forming an external diagrid lattice surface composed by continuous straight elements. The Wire-and-Arc Additive Manufacturing (WAAM) technique is adopted, ensuring the realization of continuous elements, with no connections among multiple straight elements. The invention can be adopted also in case of variable external cross-section along the height of the pole. It allows to reduce the used material and the overall weight (V. G. Laghi 2021c).

New trends are focused on the originality of the form. The diagrid structures represent the latest mutation of tubular structures, ensuring an inherent esthetic quality, structural efficiency and geometrical versatility.

In this section, the computational design is performed, having the attention on the effect of the diagrid geometry on the structural behavior. This design approach employs algorithmic processes to generate multiple unexpected structural solutions, not based on standard topology.

The design is defined by some parameters with which some structural results are obtained. Firstly, there is the geometry definition, with a subsequent structural model creation, then the structural analysis are carried out under design loads, assuming the cross-section sizing. Finally, the structural verification leads to the optimal structural design.

4.2. Background

Existing buildings (Figure 4.1) represent the initial step to design a 3D-printed diagrid column realized by means of WAAM “dot-by-dot” printing deposition strategy. The aim is to obtain a structure able to sustain itself and a possible load applied on it, such as roof, water tank. However, the object is not the replication of already existing structures, the focus is on the “most efficient shape” of them, ensuring the same performances under certain applied loads and restraint conditions, providing new forms, which will be not feasible with traditional techniques. In literature, results by Keller show that the strongest column is not uniform but tapered, being thicker at its center and thinner at its ends (Keller 1960), increasing its critical buckling load. The hyperboloid structures are doubly curved, their simultaneous curvature in opposite directions leads to high resistance against buckling. Additionally, they are able to carry the same load with less amount of material with respect to traditional cylindrical shapes, due to their anticlastic curvature (Beckh 2014), (Krivoshapko 2002).

In 1896, the Russian engineer Vladimir Shukhov designed and realized the hyperboloidal water tower, exposed in the industrial exhibition in Nizhny Novgorod. He is recognized as the pioneer of hyperboloidal structures.

The first step of the work is the reproduction of the Shukhov’s water tower, 25.6m high (Figure 4.2). This model is the starting point to perform a computational design, then the selection criterion for the final design is performed.

(a)

(b)

(c)

(d)

Figure 4.1 Examples: (a) Vinarium tower in Dolgovaske Gorice, Slovenia, (b) Kobe port tower, (c) Haesley nine bridges golf clubhouse, in South Korea, (d) Water Tower by Shukhov in Polibino, in southern Russia.

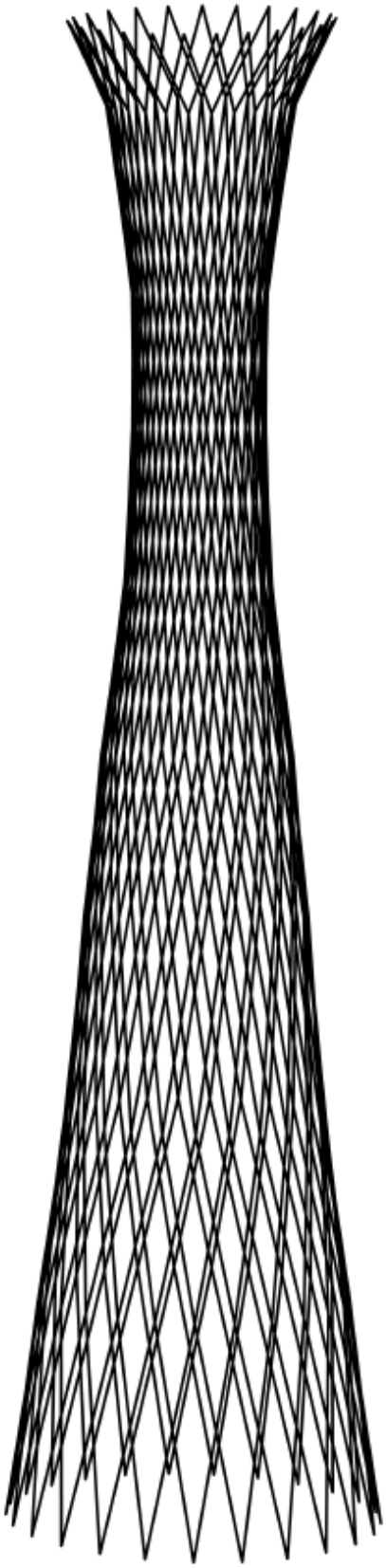

Figure 4.2 Reproduction of Shukhov Water Tower.

The fabrication of a complex structure starts from the calibration, assessing the printing process parameters and the manufacturing constraints, ensuring a structural design ready to be 3D-printed without the need of further iterations, referring to the limitations proper of the Wire-and-Arc Additive Manufacturing process.

By starting from the Shukhov's Tower, the new designs are found by varying some geometrical parameters:

- the minimum radius of the column, located in its middle cross-section,
- the radii variation proceeding from the bottom cross-section to the top one, by means of a parabolic function,
- the spacing between consecutive control sections was kept constant in some cases, and changed in others by means of an inverse function related to the radius.

The parametric design has been implemented using Grasshopper (Grasshopper) program in Rhinoceros (Rhinoceros 5) software environment, which allows to perform advanced algorithm-aided design directly on CAD drawings through a real-time iterative procedure up to the final design (V. P. Laghi 2020a).

4.3. Workflow

The computational design allows to design new structural solutions taking into account the manufactural constraints proper of the WAAM process. In this regard, a flowchart of this approach is presented (Figure 4.3) (V. P. Laghi 2022 (under review)).

(1) First step consists of an initial design, based on past solutions which are based on the basic principles of structural engineering,
(2) Then, definition of the modelling criteria and assumptions in terms of material behavior and manufacturing constraints,
(3) Definition of the boundary conditions based on the predicted application,
(4) Optimization process in order to explore the possible results based on the variation of the input data (radius and section spacing), then verified in terms of its structural performances through numerical simulations,
(5) Final design is selected among the optimized designs that comply the requested structural performances.

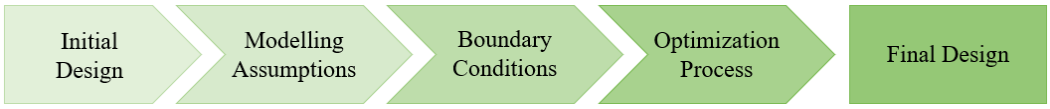

Figure 4.3 Conceptual flowchart of the computational approach.

4.4. Optimization process

The object is to determine the structural configuration. In each design step, specific geometrical parameters are chosen as the design variables, while the remaining ones are set to constant values.

The radii and the spacing between subsequent control sections are controlled by functions and related to each other.

The input are the column total height and the number of control sections along the column height, because with them there is the definition of the distance between subsequent cross-sections, which is kept constant for the definition of the radii. Additionally, another important input is the minimum radius, which is varied in the different cases debated in the Section 4.5.

4.4.1. Definition of the radius

The chosen function to define the radii is the parabolic one, by imposing that the reference system has the origin in the center of the middle control cross-section, which allows to create the column lateral surface with the revolution of the profile curve around the central axis of the considered column, with the orientation of the x axis upwards in the vertical direction, and the y axis oriented outward.

The parabolic function is:

$$y = ax^2 \tag{1}$$

Where:

- x is the distance of each control section from the origin along the x direction,
- a is the coefficient of the function,
- y is the spacing of each point from R_{min}
- R_{min} is the minimum radius of the column in correspondence of the middle control cross-section.

Constraint:

A constraint is imposed to the radius, by setting a minimum value for it different for each case. To compute the radius of each circle, the value y is added to the radius of the middle control cross-section:

$$R = y + R_{min} \tag{2}$$

4.4.2. Definition of the section spacing

Subsequently, the next step is the definition of the spacing between subsequent control cross-sections connected to the correspondent radius.

The function adopted is the inverse one, by considering an inverse relationship between the variation of the radii of two subsequent circles and the distance between them.

The inverse function is:

$$h_{rel} = \frac{b}{\Delta R} \tag{3}$$

Where:

- b is the coefficient of the function,
- ΔR is the difference between two subsequent radii,
- h_{rel} is the distance between two subsequent control cross-sections.

The section spacing h governs the length of the diagonal elements, hence a maximum value $(h_{rel})_{max}$ is imposed due to manufactural constraints.

The computation of the relative height of each cross-section is computed, and all the values are summed up to obtain the column total height, and to check if the result is equal to the input, hence a value of 3 m, therefore, the definition of b is performed by an iterative procedure, so that the right value will be the one which brings to the final height equal to the expected one.

The objective is the definition of more configurations, by varying minimum radius, parabolic and inverse functions, to be able to compare all of them, finding the better final relationship between the radius and the section spacing. The possible configurations are as follow:

- First design: the relative height remains constant, the radii of bottom and top cross-sections are the same,
- Second design: the relative height is related to the radii of the cross-sections, and the ones of the bottom and top cross-sections are assumed to be equal,
- Third design: the relative height is related to the radii of the cross-sections, the radius of the bottom cross-section is in one case larger than the top one, in the other one it is smaller.

4.4.3. Diagrid Design

The final configuration is not composed by circles, hence the next step is the realization of the external diagrid lattice surface composed by continuous straight elements.

The first step is the subdivision of the circles in equal segments with the aim to find 25 points equally spaced along the circumference, because the diagrid is obtained connecting the points of two adjacent circles: each point of one circle is connected to the shifted one of the circle above, the final outcome is the creation of diagonal elements, which are intersected along the entire column height.

The selection criterion for the final topology is based upon the manufacturing constraints proper of the WAAM process, in terms of:

- maximum angle of inclination of the diagonal elements with respect to the vertical direction,
- maximum allowable rod length.

The absence of horizontal hoops at the level of control sections determines the presence of an unbalanced outward “centrifugal” force, as presented in Figure 4.4, of the internal actions at the intersection of two bars, causing secondary bending moments, which increase the stresses in the diagonal bars. Consequently, most of the diagrid-based designs include horizontal elements (working as “hoops”) to contain and prevent these unbalanced forces in case of tall buildings (Moon 2007), (Zhou 2016), (Montuori 2014), (Mele 2014).

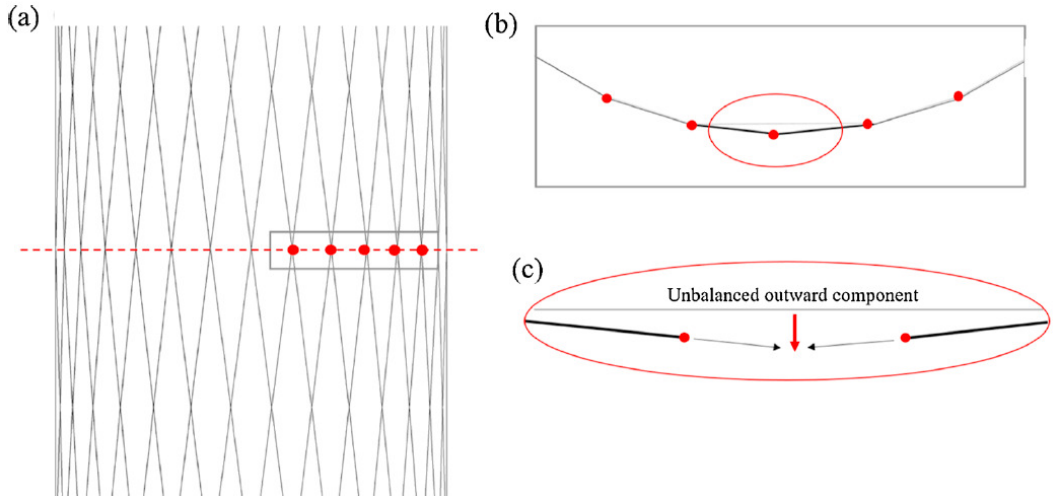

Figure 4.4 Geometrical considerations on unbalanced "centrifugal" actions on the diagrid column: (a) side view; (b) plane view; (c) close-up (V. P. Laghi 2020a).

4.5. Results of computational design process

4.5.1. First design

In this case the relative height of control cross-sections is kept constant, with the assumption of a minimum radius, being the same for both cases in which the variation of the final result is due to the different coefficient of the parabolic function, the one that allows the different final distribution of the radii along the whole length of the column.

$$R_{min} = 0.1\ m$$
$$y = ax^2\ with \begin{cases} a = 0.2 \\ a = 0.15 \end{cases} \tag{4}$$
$$R = y + R_{min}$$

Hence, the reported evaluations are presented for two cases, as follow:

(a) a = 0.2 with R_{min} = 0.1m,

(b) a = 0.15 with R_{min} = 0.1m.

Case (a):

The y dimension is computed with the input of the constant section spacing, bringing to the evaluation of the radius for each control cross-section. The Table 4.1 reports the input parameters used to compute the final radii together with the final top and bottom radii.

H	3	m
$\mathbf{n_{section}}$	21	-
$\mathbf{h_{rel}}$	0.150	m
$\mathbf{R_{min}}$	0.146	m
$\mathbf{R_{top}}$	0.596	m
$\mathbf{R_{bottom}}$	0.596	m

Table 4.1 First design (a)-geometrical parameters.

Case (b):

The y dimension is computed as for the case (a). The Table 4.2 reports the input parameters used to compute the final radii together with the final top and bottom radii.

H	3	m
$\mathbf{n_{section}}$	21	-
$\mathbf{h_{rel}}$	0.150	m
$\mathbf{R_{min}}$	0.146	m
$\mathbf{R_{top}}$	0.596	m
$\mathbf{R_{bottom}}$	0.484	m

Table 4.2 First design (b)- geometrical parameters.

The graph (Figure 4.5) shows the profile curve used to obtain the final column: the radii increase proceeding both to the top and to the bottom of the column. The point coordinates represent the radius of the circle on the horizontal axis, and the relative height of the circle, with respect to the middle one, on the vertical axis.

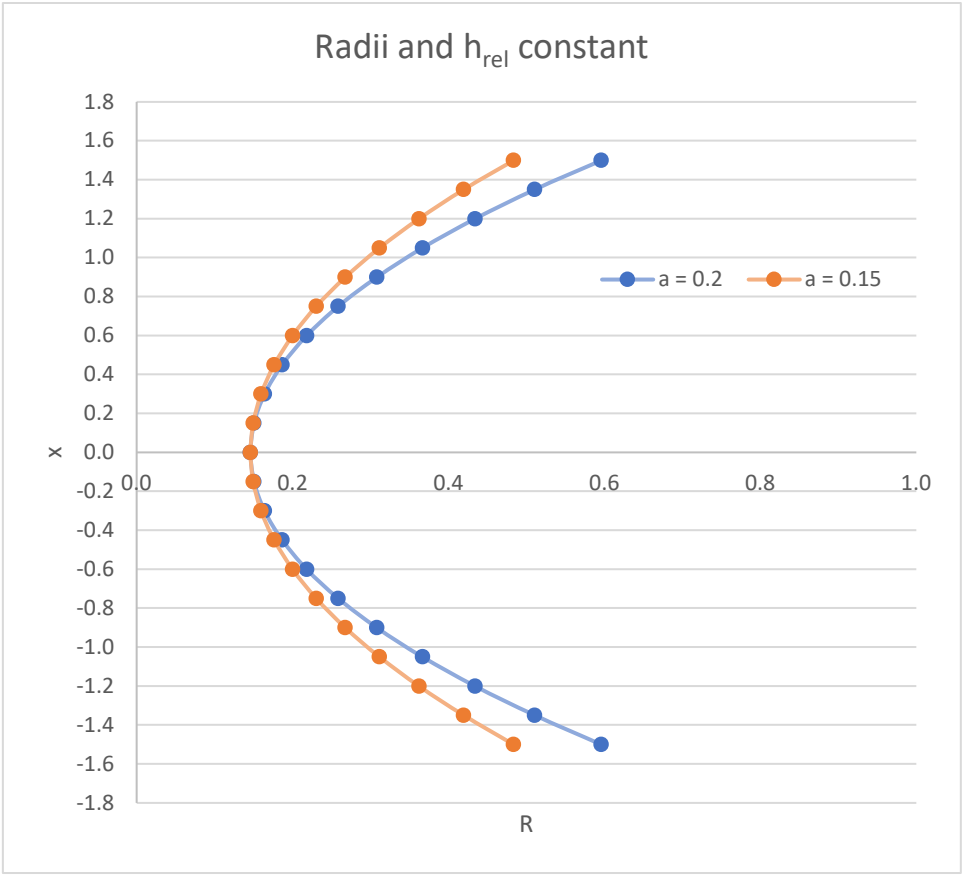

Figure 4.5 First design-parabolic variation of radii. Two different coefficients for the parabolic function are compared, a=0.2 and a=0.15.

The significant aspect is the influence of the coefficient *a* which governs the function, bringing to an higher and smaller curvature accentuation respectively in the case (a) and (b), guiding in the direction to reduce the curvature, hence to attenuate the variation of the control cross-sections dimension, to be able to obtain a more achievable column.

The following representations (Figures 4.6 and 4.7) ensure to have a better visualization of the two outcomes.

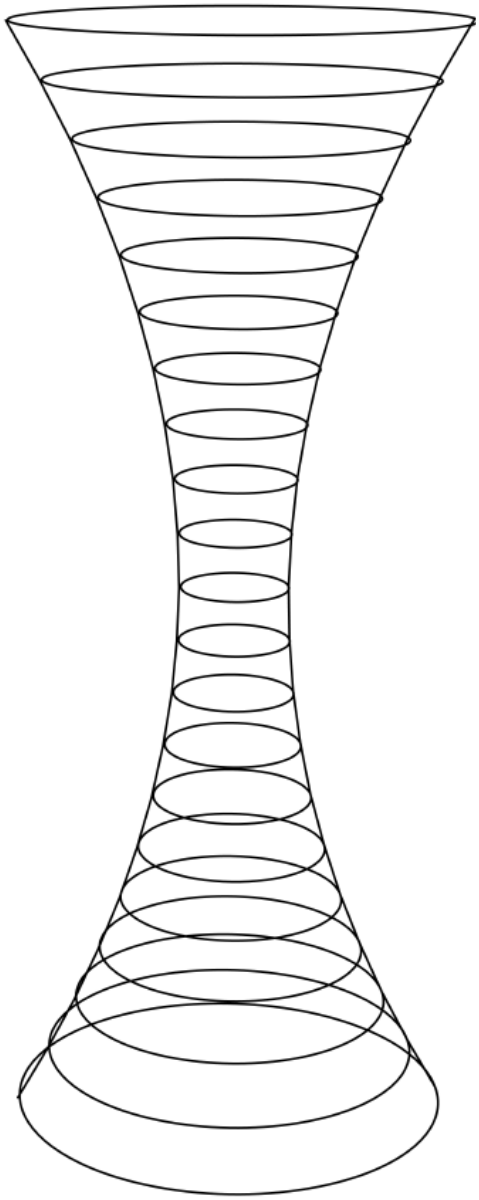

Figure 4.6 First design (a)-Realization of the circles with profile curve.

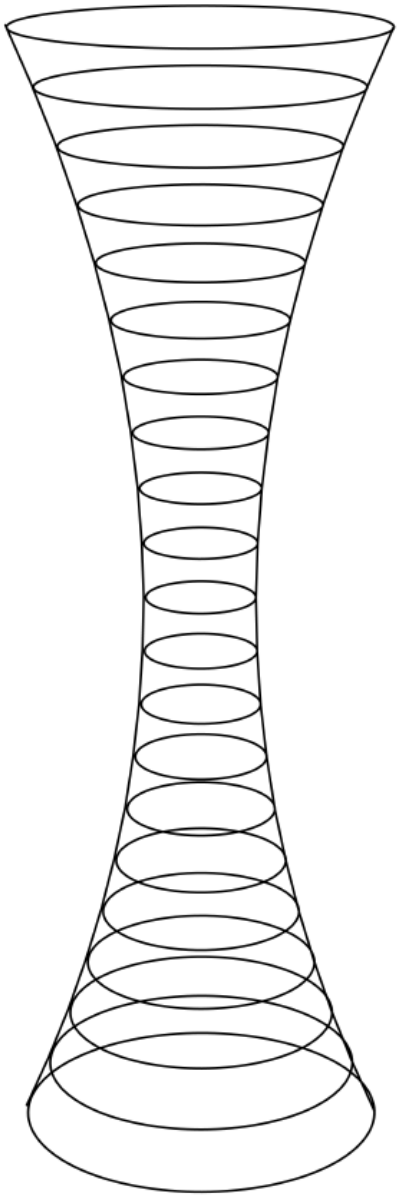

Figure 4.7 First design (b)-Realization of the circles with profile curve.

The next step is the realization of the external diagrid lattice surface.

Two important parameters to implement the design are the inclination of the elements and their length, hence this information are reported for the bottom portion, in which we are interested in:

Case (a):

- maximum inclination of the single elements with respect to the vertical direction: 47.3°
- maximum length of the elements: 5.95 cm

Case (b):

- maximum inclination of the single elements with respect to the vertical direction: 40.9°
- maximum length of the elements: 5.31 cm

The Figures 4.8 and 4.9 represent the two final cases (a) and (b).

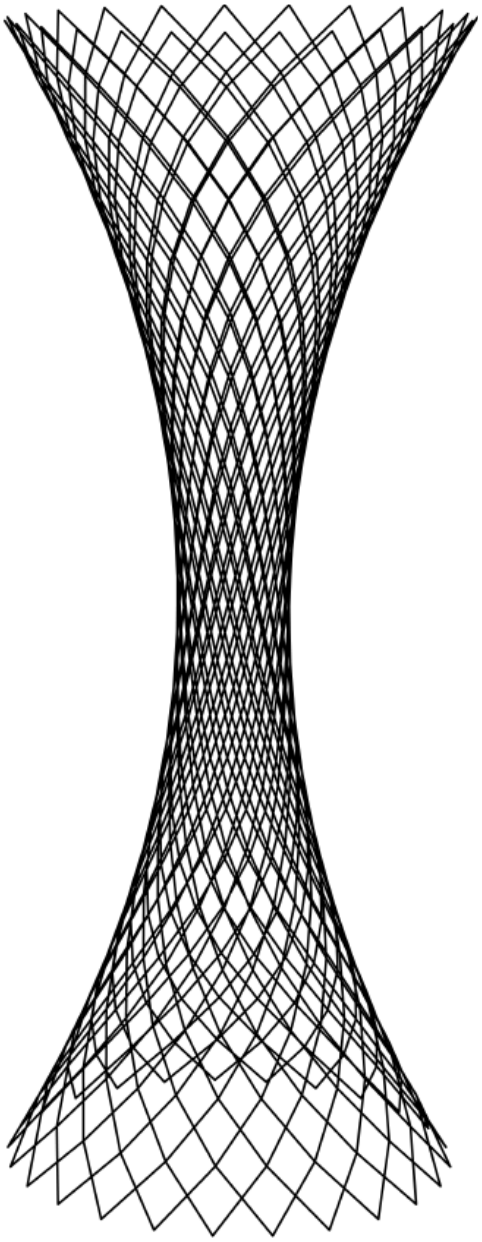

Figure 4.8 First design (a)-Diagrid column.

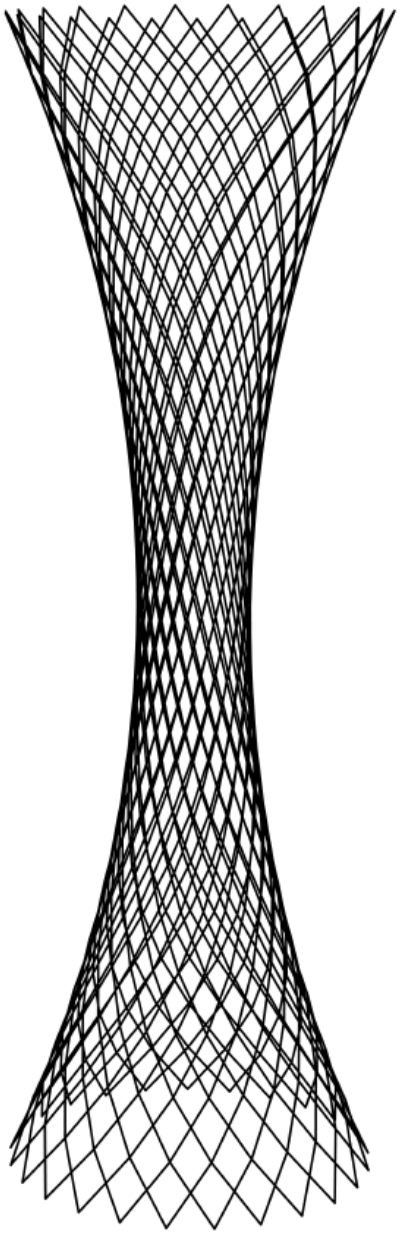

Figure 4.9 First design (b)-Diagrid column.

4.5.2. Second design

At the beginning the section spacing is kept constant with the aim to compute the distribution of radii along the height of the column.

The constrain is the coefficient of the parabolic function, it is constant for both cases, instead of the minimum radius is changed in the two cases to observe the different results.

$$\begin{gathered} y = ax^2 \; with \; a = 0.15 \\ (a) \; R_{min} = 0.146 \; m \\ (b) \; R_{min} = 0.1 \; m \\ R = y + R_{min} \end{gathered} \tag{5}$$

Hence, the reported evaluations are presented for two cases, as follow:

(a) a = 0.15 with R_{min} = 0.146m,
(b) a = 0.15 with R_{min} = 0.1m.

Case (a):

The y dimension is computed with the input of the constant section spacing, bringing to the evaluation of the radius for each control cross-section. The Table 4.3 reports the input parameters used to compute the final radii together with the final top and bottom radii.

H	3	m
$\mathbf{n_{section}}$	21	-
$\mathbf{h_{rel}}$	0.150	m
$\mathbf{R_{min}}$	0.146	m
$\mathbf{R_{top}}$	0.484	m
$\mathbf{R_{bottom}}$	0.484	m

Table 4.3 Second design (a)-geometrical parameters.

Case (b):

The y dimension is computed as for the case (a). The Table 4.4 reports the input parameters used to compute the final radii together with the final top and bottom radii.

H	3	m
$\mathbf{n_{section}}$	21	-
$\mathbf{h_{rel}}$	0.150	m
$\mathbf{R_{min}}$	0.100	m
$\mathbf{R_{top}}$	0.438	m
$\mathbf{R_{bottom}}$	0.438	m

Table 4.4 Second design (b)- geometrical parameters.

The graph (Figure 4.10) shows the profile curve used to obtain the final column: the radii increase proceeding both to the top and to the bottom of the column. The point coordinates represent the radius of the circle on the horizontal axis, and the relative height of the circle, with respect to the middle one, on the vertical axis.

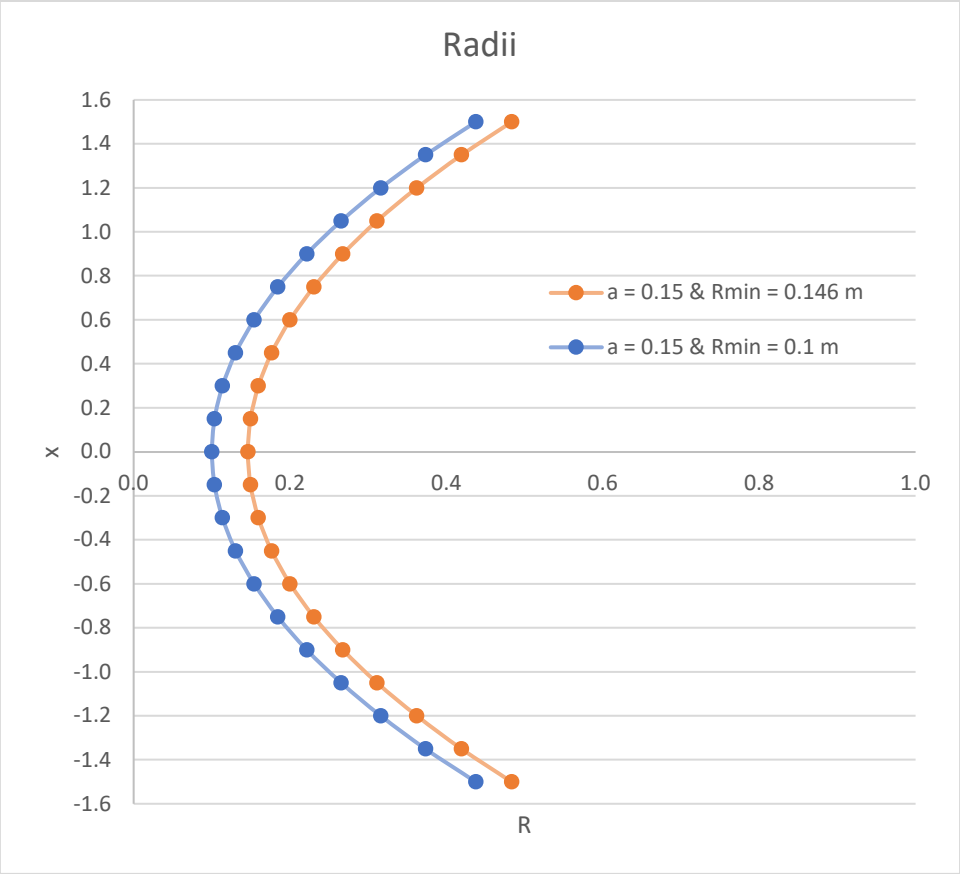

Figure 4.10 Second design-parabolic variation of radii. Two different radii are compared, (a) R_{min}=0.146m and (b) R_{min}=0.1m.

In the two cases the variation of radii is the same, due to the same parabolic function, only the initial point, represented by the minimum radius changes.

In this case the significant aspect is not related to the radii, as it can be seen, although the further change is computed in the subsequent phase, in which the section spacing is no more assumed constant, as at the beginning; the evaluation of the spacing is performed by taking into account an inverse proportionality between the radii and the above mentioned height.

The height is evaluated by using the equation (3).

The difference between the two cases is correlated to the upper bound of the relative height, bringing to a different value for the coefficient b to ensure the total height of 3 m.

Hence, the reported evaluations are presented for two cases, as follow:

(a) b = 0.003 with R_{min} = 0.146m,
(b) b = 0.0038 with R_{min} = 0.1m.

Tables 4.5 and 4.6 present the computed section spacings related to the bottom, middle and top cross-sections.

Case (a):

$$(h_{rel})_{max} = 0.5m$$

	R [m]	**h_{rel}** [m]
Bottom	0.484	0.046
Middle	0.146	0.500
Top	0.484	0.046

Table 4.5 Second design (a)-Evaluation of the new section spacings inversely proportional to the corresponding radius.

Case (b):

$$(h_{rel})_{max} = 0.3m$$

	R [m]	**h_{rel}** [m]
Bottom	0.438	0.059
Middle	0.100	0.300
Top	0.438	0.059

Table 4.6 Second design (b)-Evaluation of the new section spacings inversely proportional to the corresponding radius.

The graph (Figure 4.11) shows how the relative height changes with the relative variation of the radii.

The blue line represents the case (a) in which it is considered an higher maximum relative height, 0.5m, the orange line represents the case (b) in which it is considered a maximum relative height of 0.3m, having two equal relative height for different radius increment, they correspond to the middle portion of the column, where the variation between the radii is smaller, hence the height results to be higher than the upper bound, due to the inverse proportion between them, therefore it is assumed equal to the allowable maximum value.

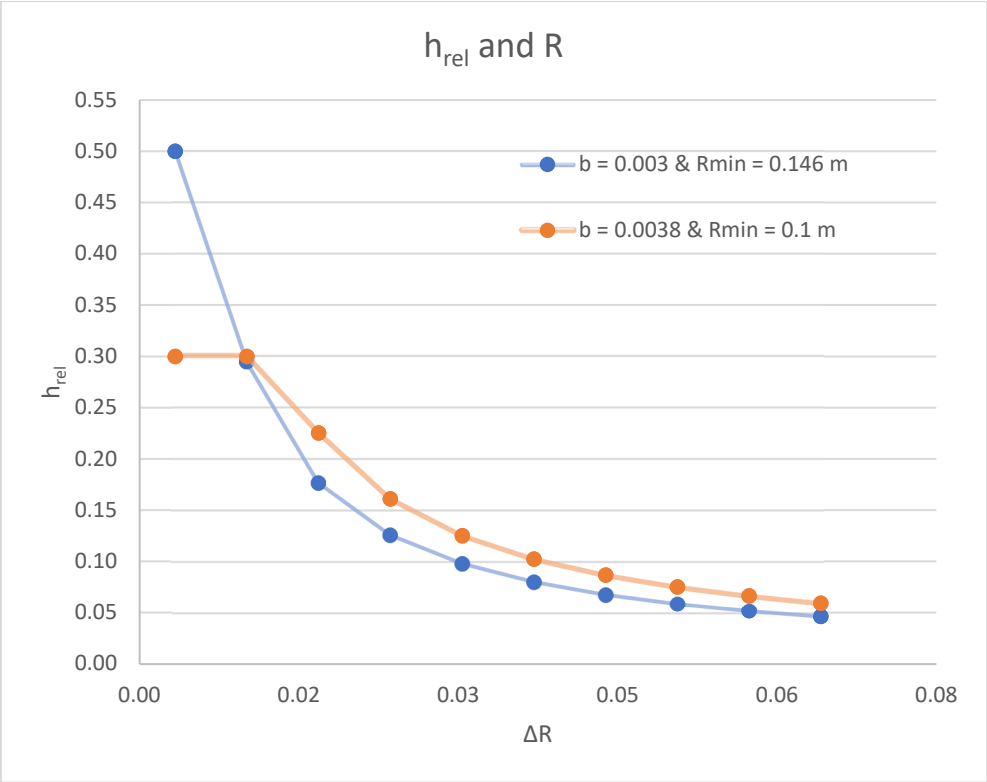

Figure 4.11 Second design-h_{rel} is computed as inversely proportional to R, for case (a) with b=0.003 and R_{min}=0.146m and for case (b) with b=0.0038 and R_{min}=0.1m.

The following representations (Figures 4.12 and 4.13) ensure to have a better visualization of the outcomes.

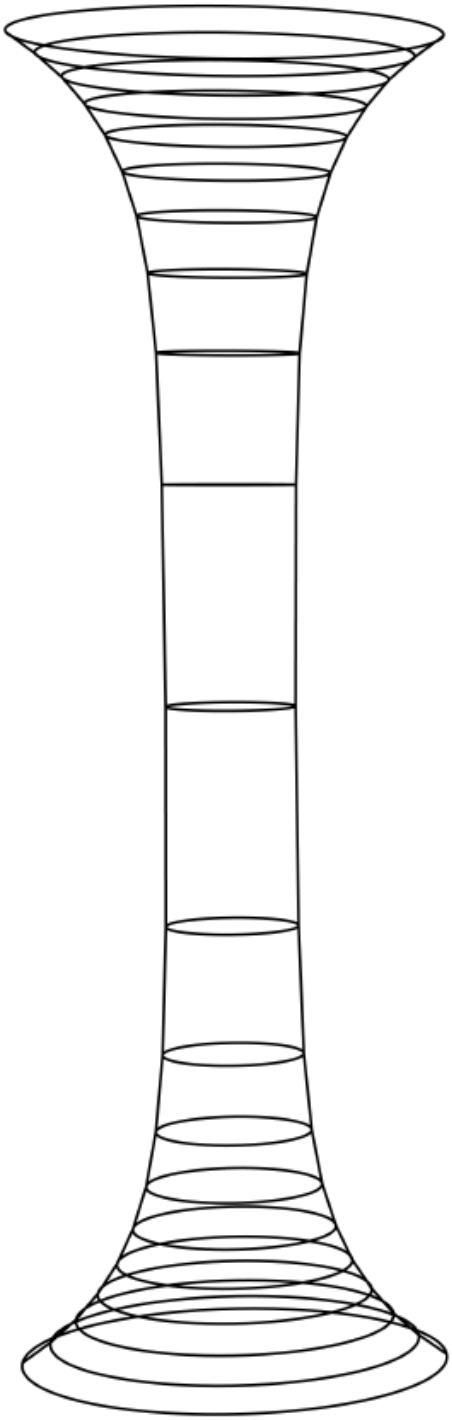

Figure 4.12 Second design (a)-Realization of the circles with profile curve.

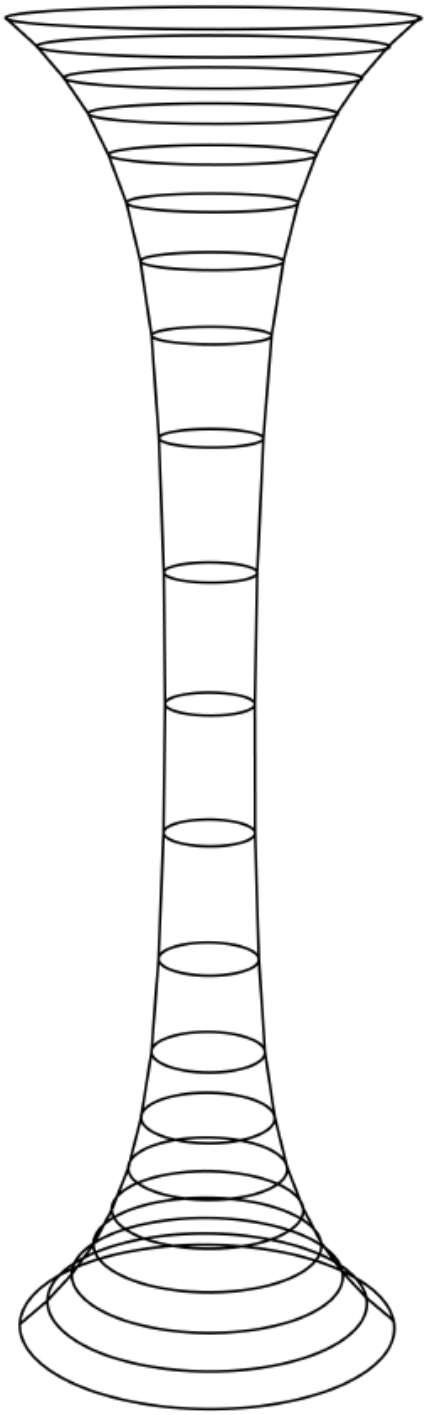

Figure 4.13 Second design (b)-Realization of the circles with profile curve.

The next step is the realization of the external diagrid lattice surface.

Two important parameters to implement the design are the inclination of the elements and their length, hence this information are reported for the bottom portion, in which we are interested in:

Case (a):

- maximum inclination of the single elements with respect to the vertical direction: 70.5°
- maximum length of the elements: 3.69 cm

Case (b):

- maximum inclination of the single elements with respect to the vertical direction: 63.9°
- maximum length of the elements: 3.62 cm

The Figures 4.14 and 4.15 represent the two final cases (a) and (b).

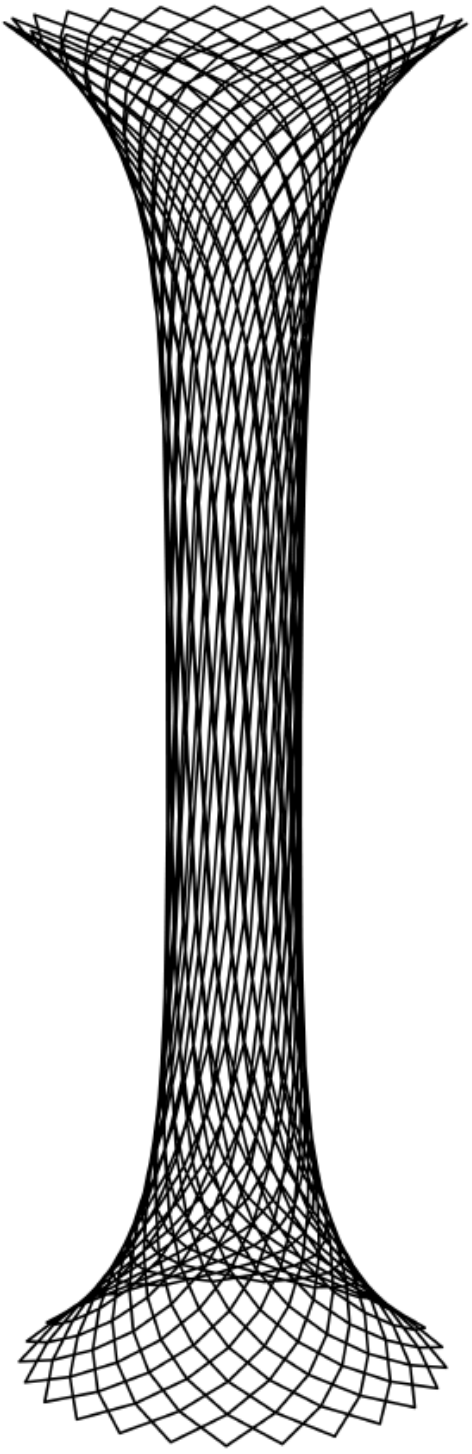

Figure 4.14 Second design (a)-Diagrid column.

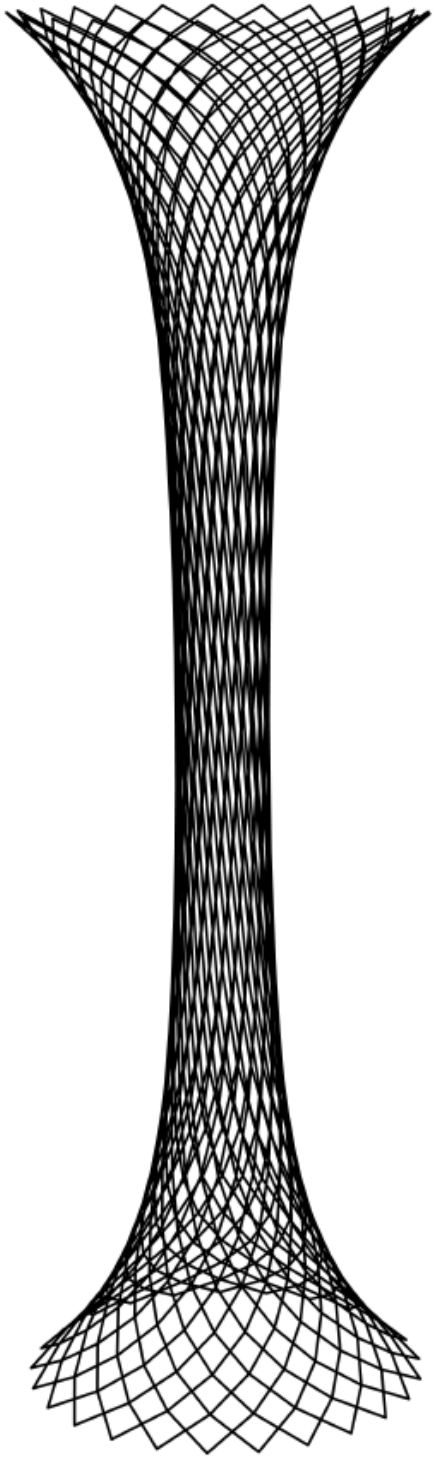

Figure 4.15 Second design (b)-Diagrid column.

4.5.3. Third design

At the beginning the section spacing is kept constant with the aim to compute the distribution of radii along the height of the column.

A minimum value for the radius of the middle cross-section is assumed, reported in the following data, and the distribution of the radii is found by means of the parabolic function.

The difference of this case, compared to the previous ones, is inherent in the assumption of two different parabolic functions to describe the top and bottom portions of the column with respect to the middle control cross-section, by changing the coefficient of the parabolic function, as described in (6), (7), (8) and (9). The two explored cases are referred to as the wider base cross-section and wider top one respectively.

The minimum radius is a constrain for both cases, and it is kept constant to compute the function outcomes.

$$R_{min} = 0.1\ m$$

Case (a):

Bottom part:

$$\begin{aligned} y &= ax^2\ with\ a = 0.12 \\ R &= y + R_{min} \end{aligned} \tag{6}$$

Top part:

$$\begin{aligned} y &= ax^2\ with\ a = 0.05 \\ R &= y + R_{min} \end{aligned} \tag{7}$$

Case (b):

Bottom part:

$$y = ax^2 \; with \; a = 0.05$$
$$R = y + R_{min} \tag{8}$$

Top part:

$$y = ax^2 \; with \; a = 0.15$$
$$R = y + R_{min} \tag{9}$$

Case (a)

The y dimension is computed with the input of the constant section spacing, bringing to the evaluation of the radius for each control cross-section. The Table 4.7 reports the input parameters used to compute the final radii together with the final top and bottom radii.

H	3	m
$n_{section}$	21	-
h_{rel}	0.150	m
R_{min}	0.100	m
R_{top}	0.213	m
R_{bottom}	0.370	m

Table 4.7 Third design-geometrical parameters

The graph (Figure 4.16) shows the profile curve used to obtain the final column. The point coordinates represent the radius of the circle on the horizontal axis, and the relative height of the circle, with respect to the middle one, on the vertical axis.

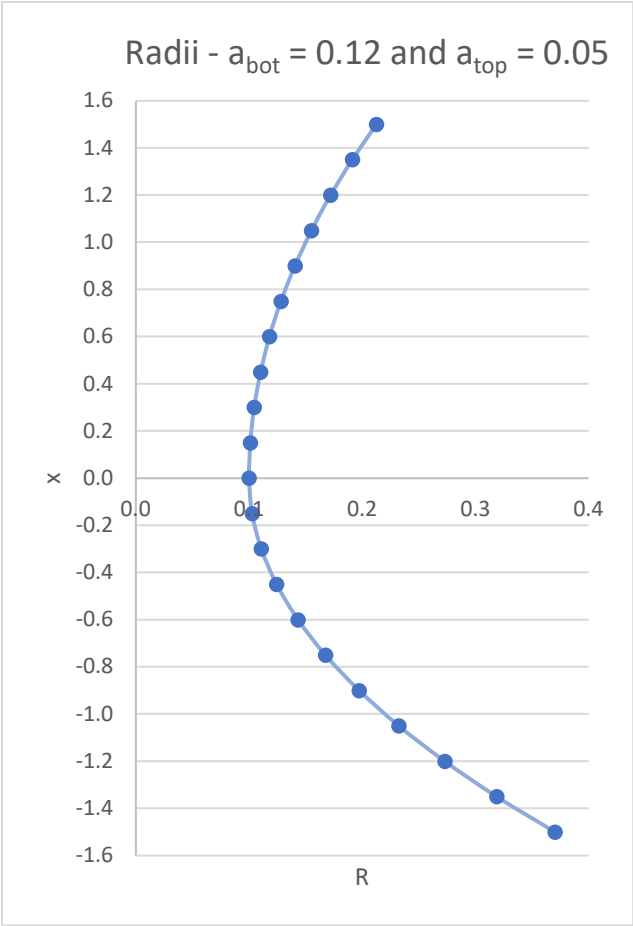

Figure 4.16 Third design (a)-parabolic variation of radii. R_{min}=0.1m. Two different parabolic function, bottom part a=0.12 and top part a=0.05.

Case (b)

The y dimension is computed as for the case (a). The Table 4.8 reports the input parameters used to compute the final radii together with the final top and bottom radii.

H	3	m
$\mathbf{n_{section}}$	21	-
$\mathbf{h_{rel}}$	0.150	m
$\mathbf{R_{min}}$	0.100	m
$\mathbf{R_{top}}$	0.438	m
$\mathbf{R_{bottom}}$	0.213	m

Table 4.8 Third design (b)-input parameters

The graph (Figure 4.17) shows the profile curve used to obtain the final column.

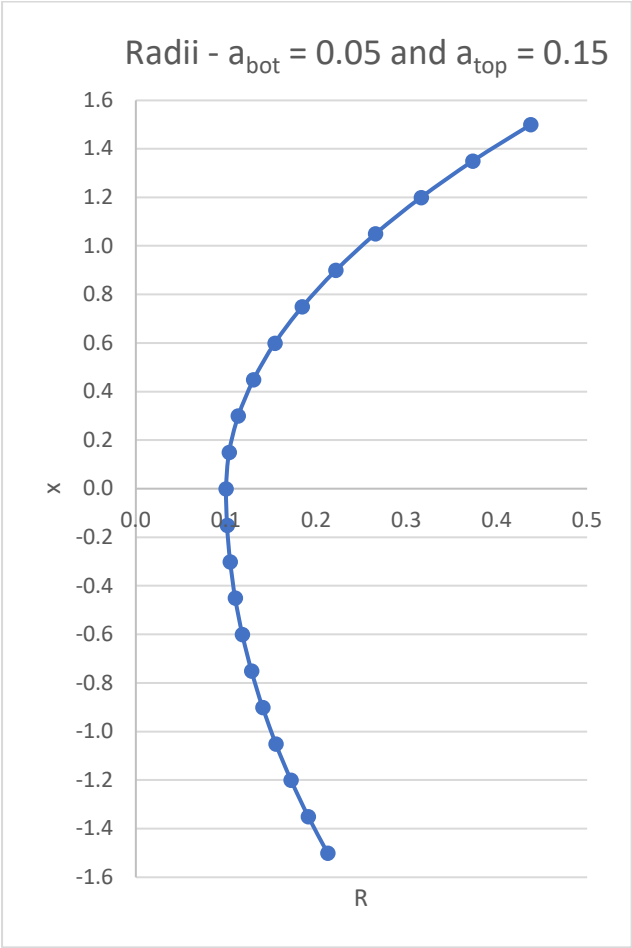

Figure 4.17 Third design (b)-parabolic variation of radii. R_{min}=0.1m. Two different parabolic functions, bottom part a=0.05 and top part a=0.15.

The relative height of control cross-sections is no more assumed constant, its evaluation is performed by taking into account an inverse proportionality between the relative height and radius of each cross-section. The equation (3) is the one used to compute the relative height.

The assumed maximum value for the section spacing is:

$$(h_{rel})_{max} = 0.3m$$

This value is related to the manufactural constraints.

Case (a):

Table 4.9 presents the computed section spacings related to the bottom, middle and top cross-sections.

$$b = 0.00189$$

$$(h_{rel})_{max} = 0.3m$$

	R [m]	**h_{rel}** [m]
Bottom	0.370	0.037
Middle	0.100	0.300
Top	0.213	0.088

Table 4.9 Third design(a)-Evaluation of the new section spacings inversely proportional to the corresponding radius.

The graph (Figure 4.18) shows how the relative height changes with the relative variation of the radii.

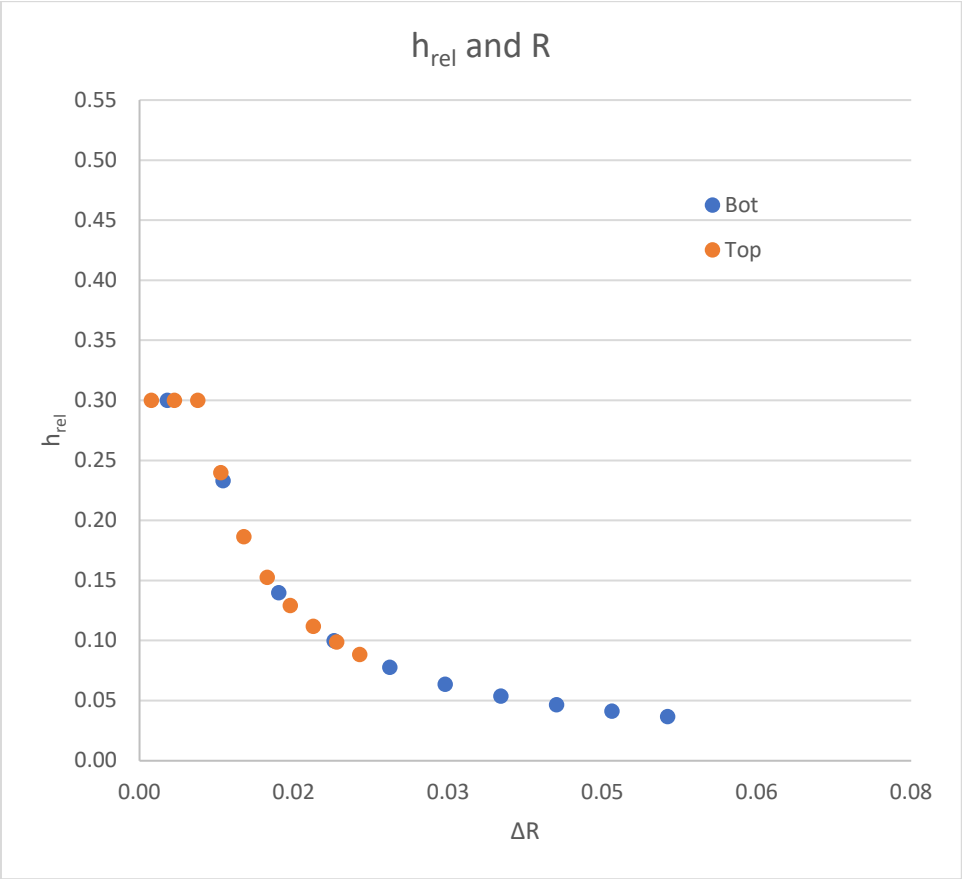

Figure 4.18 Third design(a)-h_{rel} is computed as inversely proportional to R: blue dots represent the bottom cross-sections with respect to the middle one, orange dots represent the top ones.

Each dot represents the relative radius and relative height of a control cross-section with respect to the previous one. The two colors differentiate the dots related to the bottom and the ones related to the top portion of the column with respect to its middle cross-section. Higher variation of the radius brings to smaller section spacings, as shown in the bottom part of the column (blue dots). The opposite situation is in the top portion, where there are smaller variation of the radii, it brings to higher values of the relative height, with three of them equal to 0.3 m, which is the maximum allowable value.

Case (b):

Table 4.10 presents the computed section spacings related to the bottom, middle and top cross-sections.

$$b = 0.00207$$

$$(h_{rel})_{max} = 0.3m$$

	R [m]	**h_{rel}** [m]
Bottom	0.213	0.097
Middle	0.100	0.300
Top	0.438	0.032

Table 4.10 Third design(b)- Evaluation of the new section spacings inversely proportional to the corresponding radius.

The graph (Figure 4.19) shows how the relative height changes with the relative variation of the radii.

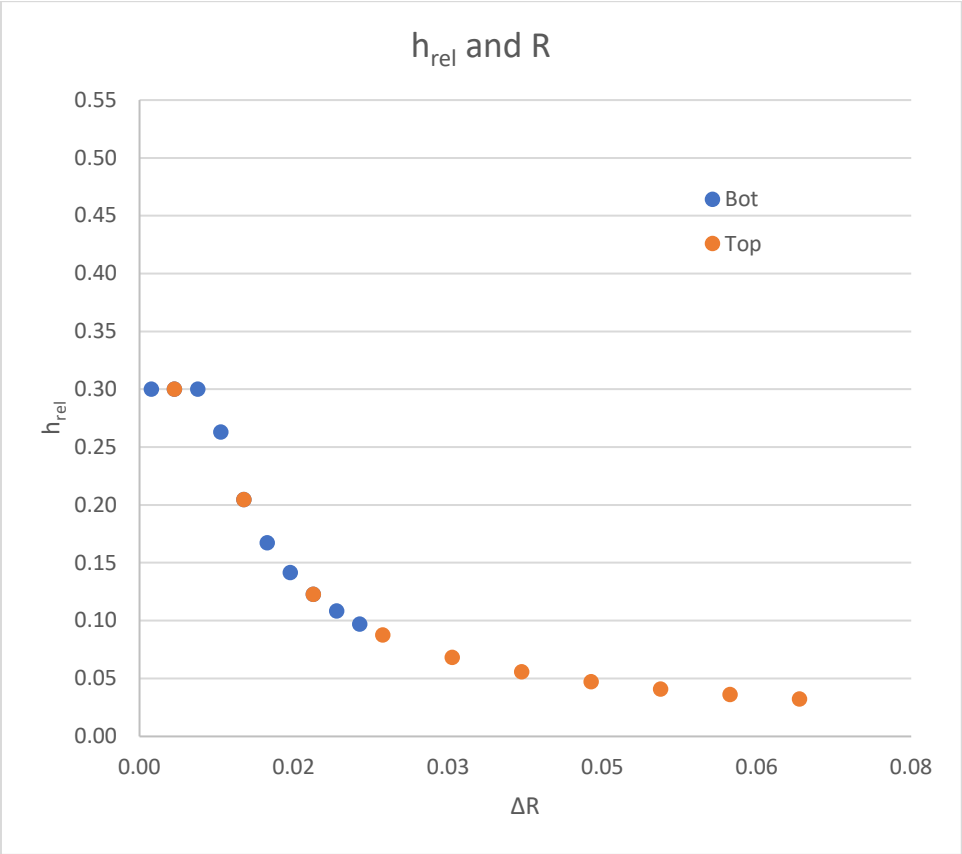

Figure 4.19 Third design(b)-h_{rel} is computed as inversely proportional to R: blue dots represent the bottom cross-sections with respect to the middle one, orange dots represent the top ones.

Each dot represents the relative radius and section spacing with respect to the previous one. The two colors differentiate the dots related to the bottom and the ones related to the top portion of the column with respect to the middle cross-section. Higher variation of the radius brings to smaller section spacings, as shown in the top part of the column (orange dots). The opposite situation is in the bottom portion, where there are smaller variation of the radii, it brings to higher values of the relative height, with three of them equal to 0.3 m, which is the maximum allowable value.

The following representations (Figures 4.20 and 4.21) ensure to have a better visualization of the outcomes.

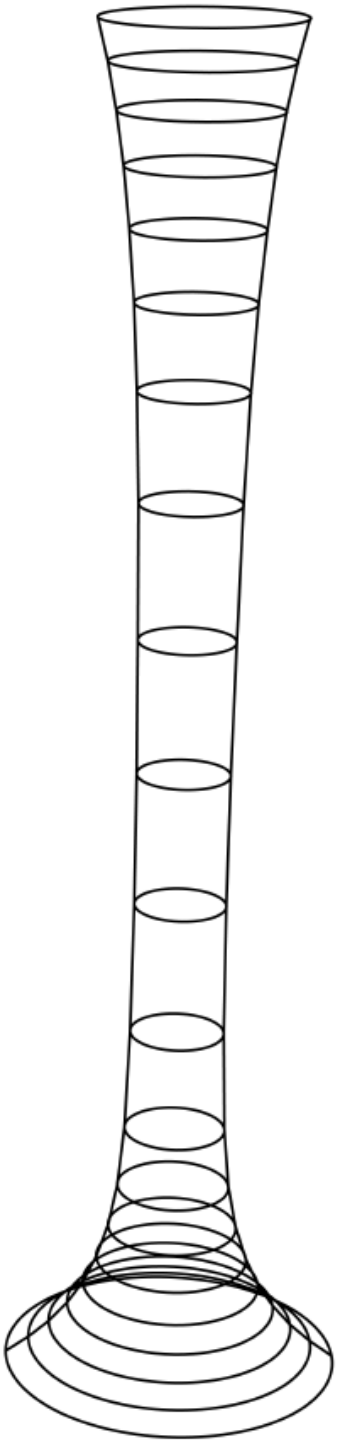

Figure 4.20 Third design (a)-Realization of the circles with profile curve.

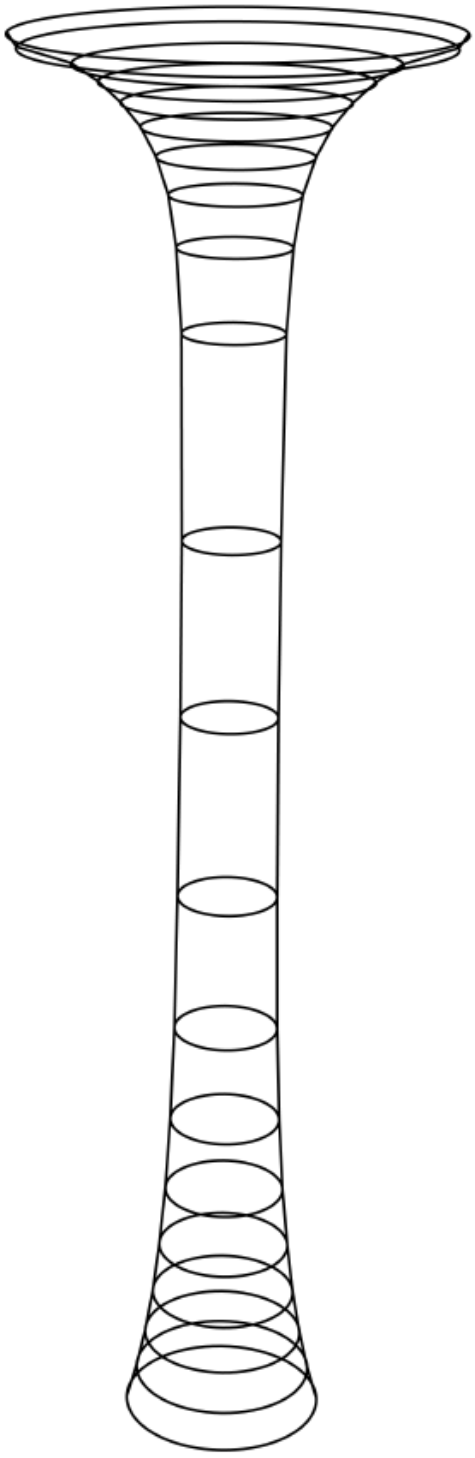

Figure 4.21 Third design (b)-Realization of the circles with profile curve.

The next step is the realization of the external diagrid lattice surface.

Two important parameters to implement the design are the inclination of the elements and their length, hence this information are reported for the bottom portion, in which we are interested in:

Case (a):

- maximum inclination of the single elements with respect to the vertical direction: 69.7°
- maximum length of the elements: 2.87 cm

Case (b):

- maximum inclination of the single elements with respect to the vertical direction: 103.91°
- maximum length of the elements: 2.56 cm

The Figures 4.22 and 4.23 represent the two final cases (a) and (b).

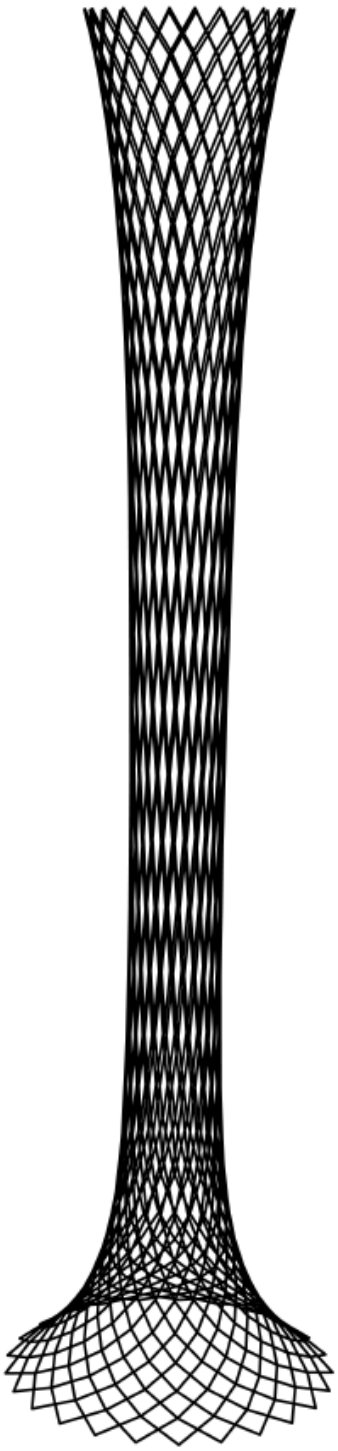

Figure 4.22 Third design (a)-Diagrid column.

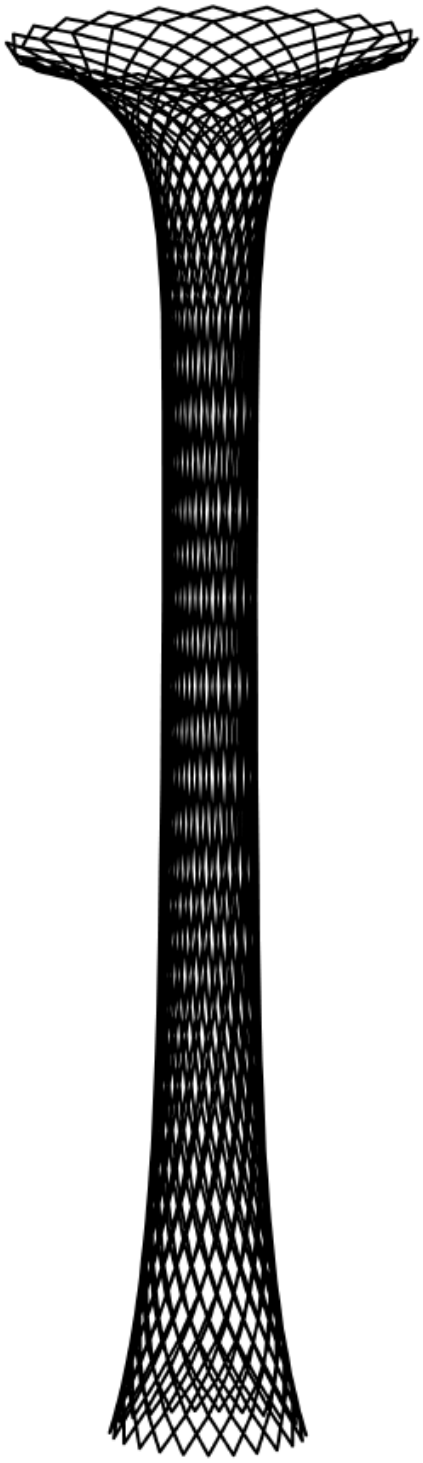

Figure 4.23 Third design (b)-Diagrid column.

4.6. Structural verification and definition of the final design

As presented in the Section 4.4.3, the absence of horizontal hoops at the level of control sections determines the presence of an unbalanced outward "centrifugal" force of the internal actions at the intersection of two bars, causing secondary bending moments, which increase the stresses in the diagonal bars. Therefore, the structural verification is performed in order to find the design ensuring the bending moment reduction in the bars. Firstly, the vertical load applied at the top of the column is computed as the resultant of distributed loads simulating the dead and live loads applied on top of a wooden porch structure. The column would withstand the loads applied on an influence area corresponding to a 5 m column spacing. The column is considered clamped at the base, while the top is free to translate and rotate (cantilever condition).

Among the designed column (Section 4.5), the verification is reported for two of them (case (b) Section 4.5.2 and case (b) Section 4.5.3), presenting the same following geometrical parameters:

- minimum radius of 0.1 m,
- parabolic function coefficient is a = 0.15: in case of Figure 4.15 for both top and bottom portions (case (b) Section 4.5.2), instead of, in case of Figure 4.23 only for the top portion (case (b) Section 4.5.3),
- maximum section spacing: $(h_{rel})_{max} = 0.3\ m$.

For the sake of comparison, a tubular diagrid column (constant diameter along the height) was designed with the height of 3 m, the same as the other designed diagrid columns. The cross-sectional radius and the section spacing are constant along the height, with a radius of 0.2 m and a section spacing of 0.3 m, therefore with a number of 11 control cross-sections.

Additionally, an hyperboloidal diagrid column was designed starting from the column designed in case (b) Section 4.5.2, with the height of 3 m and a number of 15 control cross-sections, maximum bottom and top cross-sectional radius of 0.4 m

and a section spacing varying up to 0.77 m in the central portion of the column (Figure 4.27).

The structural performances of the three diagrid columns were evaluated by means of FE analysis carried out with the commercial software SAP2000 (SAP2000). A linear static analysis was conducted with the purpose of evaluating the structural response due to a constant vertical load of 20 kN. Each bar is modelled with a unique beam element having circular cross-section of 6 mm diameter. The total vertical load is applied through concentrated vertical forces applied at the top nodes. Subsequently, the bending moment diagrams along the height of the three solutions are displayed, in order to perform the subsequent evaluation (Figures 4.24, 4.25, 4.26 and 4.27).

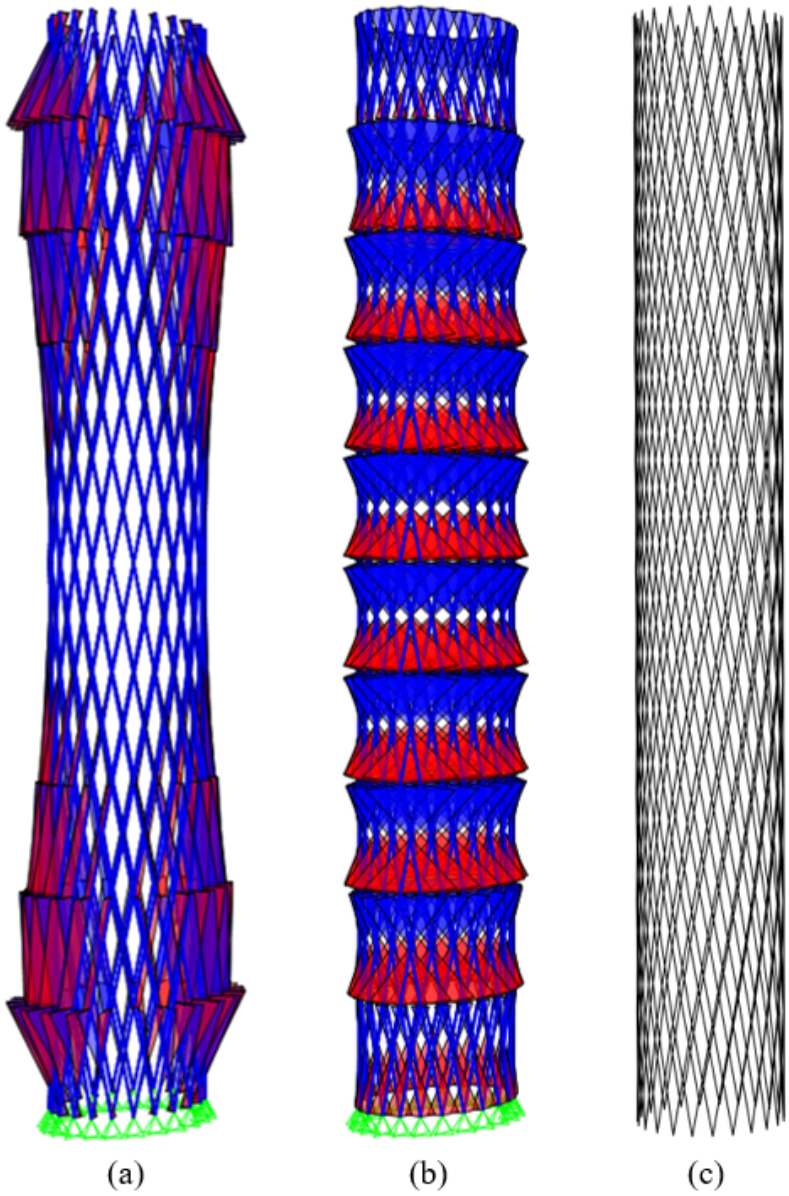

Figure 4.24 Results from structural analysis in terms of bending moment diagrams along the height of the tubular diagrid column: (a) moment 2-2, (b) moment 3-3, (c) diagrid column.

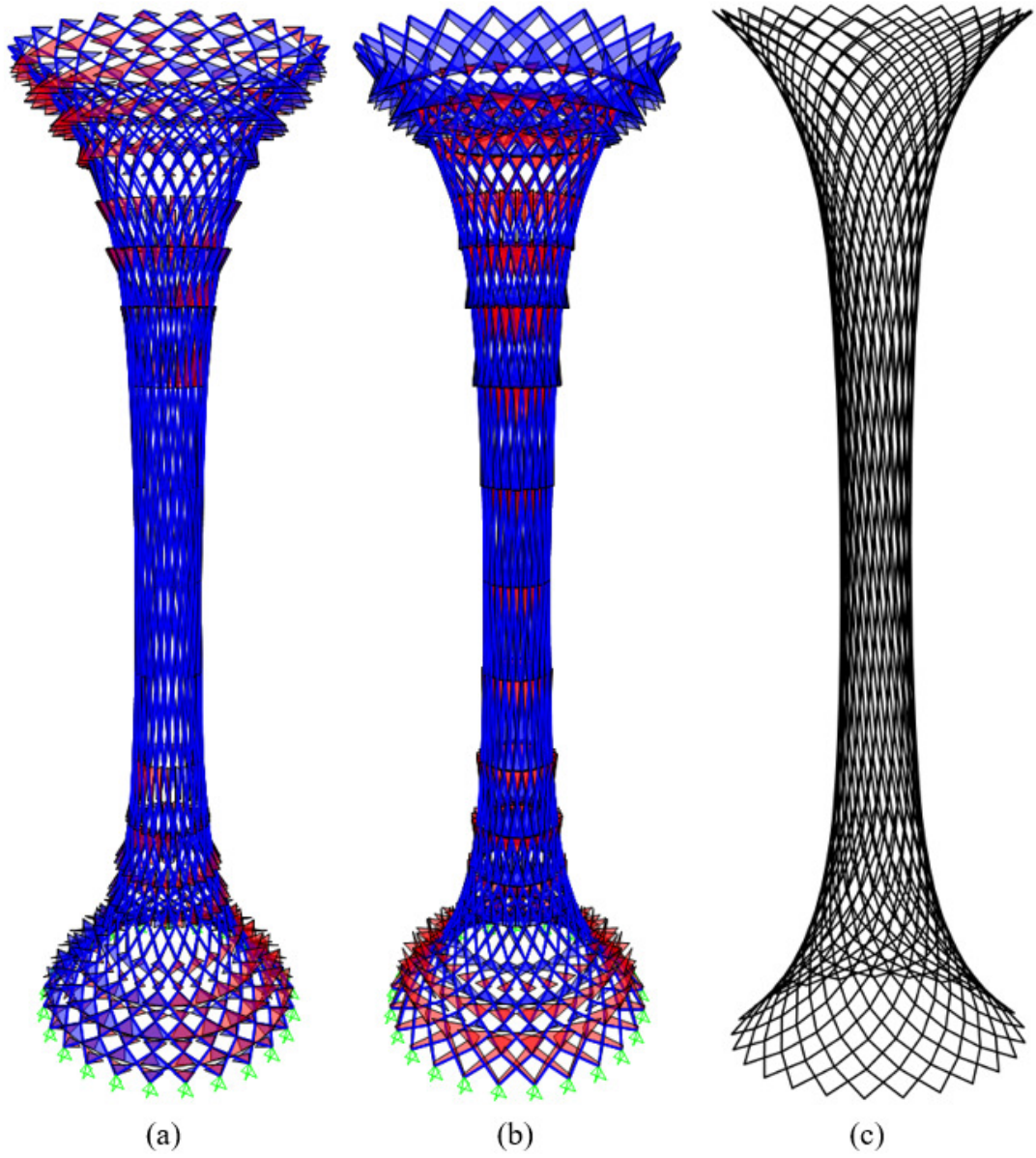

Figure 4.25 Results from structural analysis in terms of bending moment diagrams along the height of the hyperboloidal diagrid column (case (b) Section 4.5.2): (a) moment 2-2, (b) moment 3-3, (c) diagrid column.

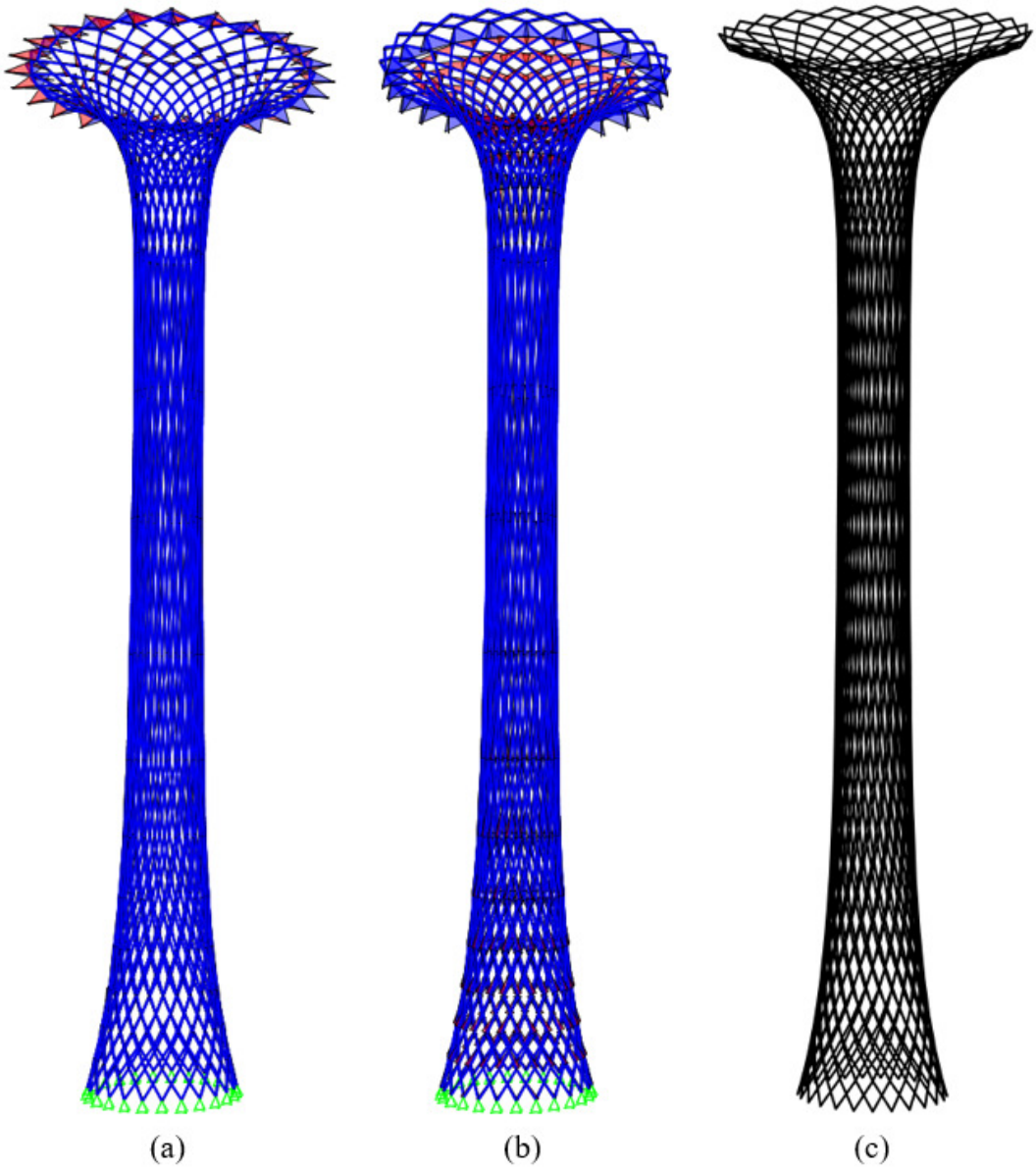

Figure 4.26 Results from structural analysis in terms of bending moment diagrams along the height of the diagrid column (case (b) Section 4.5.3): (a) moment 2-2, (b) moment 3-3, (c) diagrid column.

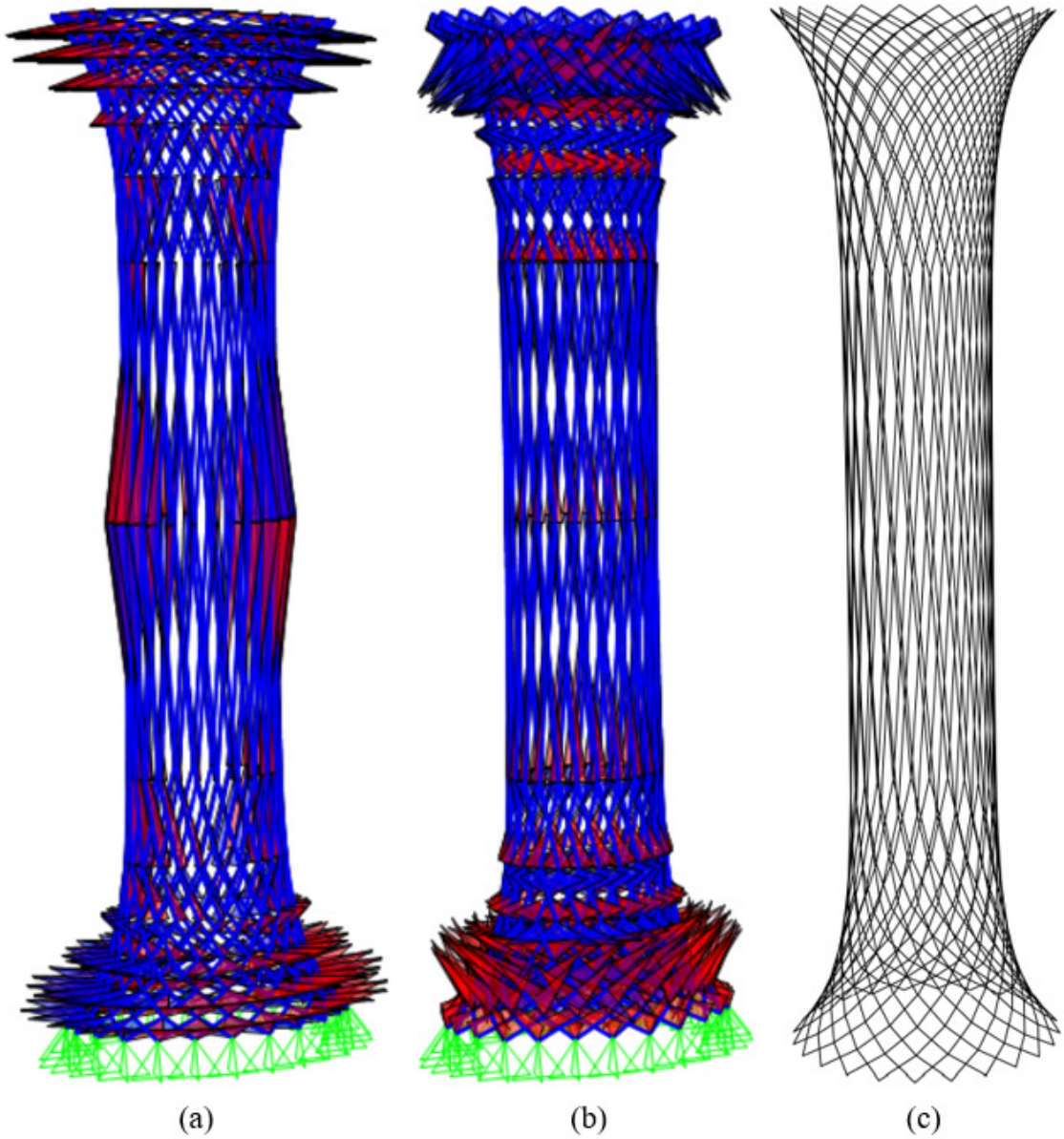

Figure 4.27 Results from structural analysis in terms of bending moment diagrams along the height of the 3 m high hyperboloidal diagrid column with 15 control cross-sections and maximum radius of 0.4 m: (a) moment 2-2, (b) moment 3-3, (c) diagrid column.

In order to evaluate the effectiveness of the different solutions it is used the utilization factor correspondent to the maximum bending moment along all members divided by the resistant moment (due to the cross-sectional area).

Design	N_{res}	N_{max}	N_{max}/N_{res}	M_{res}	M_{max}	M_{max}/M_{res}
	[kN]	**[kN]**	**[-]**	**[kNm]**	**[kNm]**	**[-]**
Tubular	7.07	0.44	0.06	5.30E-03	1.26E-02	2.38
Second case (b) – Hyperboloidal	7.07	0.94	0.13	5.30E-03	4.60E-03	0.87
Third case (b) - Top	7.07	1.66	0.23	5.30E-03	4.01E-02	7.56
Hyperboloidal with 15 cross-sections	7.07	0.88	0.12	5.30E-03	4.50E-03	0.85

Table 4.11 Results from structural analysis in terms of utilization factor

The final results indicate that the hyperboloidal solutions are more efficient than the other two diagrid columns, especially in case of the tubular one (Table 4.11). In particular, the adopted design, hyperboloidal diagrid column, presents a resistant moment higher with respect to the maximum bending moment along the column.

The Figure 4.28 shows the adopted diagrid column structure with the nominal bar diameter of 6 mm.

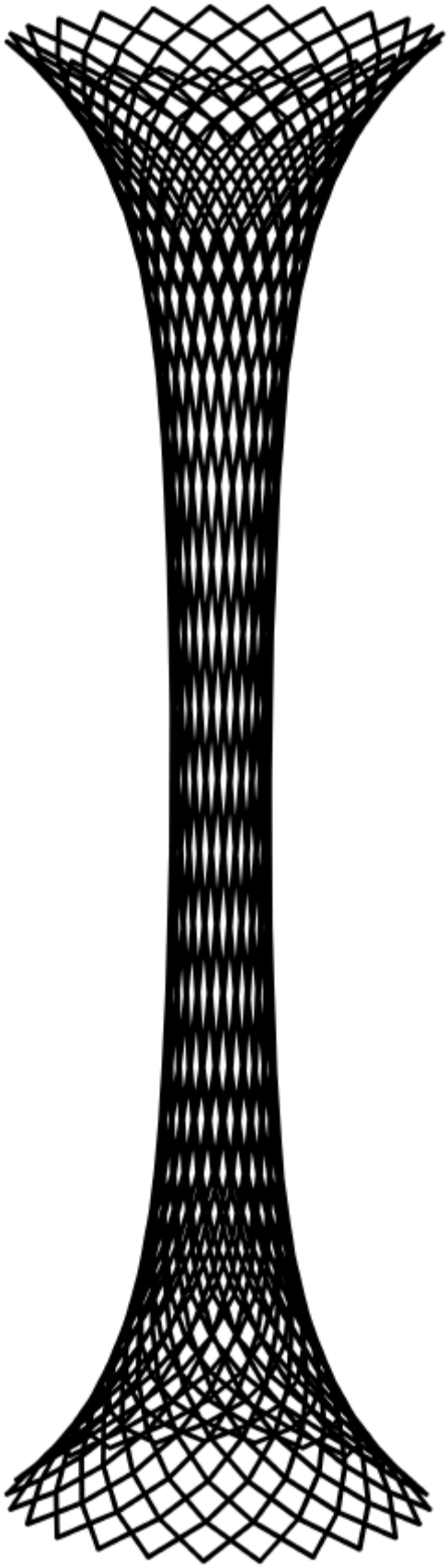

Figure 4.28 Final design of the diagrid column.

5. Fabrication

5.1. Overview

The presented work has the aim to show the procedure adopted to print different specimens, in order to correlate each specimen geometry to its own process parameters and path-planning.

The objective to print a diagrid column (final design is presented in Section 4.6), passes through the knowledge of bars with the longitudinal axis coincident with the vertical build direction, bars with the longitudinal axis inclined by a certain angle with respect to the build direction, and also “crossed-bars”, by focusing the attention on the intersection mechanical behavior.

The elements presented in this work were produced by means of Wire-and-Arc Additive Manufacturing (WAAM) technique, enabling the realization of elements of larger size. The advantage with respect to the other processes is inherent in the set-up flexibility, beyond the geometrical constraints related to the dimension and shape of the printed elements.

5.2. WAAM Setup

Algorithm-aided design tools are adopted to design the output of the WAAM printing technique. This work is performed by means of Grasshopper, a visual programming language and environment that runs within Rhinoceros 3D computer-aided design (CAD) application, from the design phase to the printing one, passing through the programming of the robot's toolpath. Robot, Grasshopper plug-in, allows to transfer programs to the controller and accurate real-time simulations. The commands are related to:

(i) Target plane,
(ii) Robot configuration,
(iii) Type of motion,
(iv) Tool geometry, weight, center of mass and Tool Center Point (TCP) plane,
(v) Speed of robot in mm/s,
(vi) Approximation zone in mm,
(vii) Robot commands.

5.3. Manufacturing Process

The presented works are realized with the “dot-by-dot” printing strategy, by means of steel welding wire ER70S-6, with a diameter of 1.2 mm. The result is the creation of straight rod-like specimens with different orientations with respect to the build direction (perpendicular to the substrate).

The printed specimens were produced with Gas Metal Arc Welding (GMAW). GMAW is used to refer to metal inert gas (MIG) welding or metal active gas (MAG) welding, characterized by a consumable wire electrode. The arc is struck between the workpiece and a metal wire electrode. Electrical energy for the arc is passed to the wire through the contact tube in the welding gun. The gas nozzle that surrounds the contact tube supplies shielding gas to protect the arc and the weld pool (Liu 2022).

Cold Metal Transfer welding is based on short-circuiting transfer process. It provides controlled method of material deposition. The wire feed rate and the cycling arcing phase are controlled to realize sufficient energy to melt both the base material and a globule of filler wire (Selvi 2018). The CMT is an efficient procedure to reduce the heat transferred to the layers under deposition, without dropping the deposition rate (Scotti 2020).

The experimental robotic welding setup was comprised of Universal Robot (UR16e) robotic arm and Fronius TPS 600i PULSE power source. The substrate of the printed samples is a steel plate, which is fixed to a stationary table, with dimensions which vary based on the final outcome size, with 13 mm of thickness. The steel wire adopted in this study is ER70S-6, SupraMig Ultra supplied by Lincoln Electric (Lincoln Electric), with a diameter of 1.2 mm.

Each iteration includes the following steps:

(i) The robotic arm moves toward the axis passing through the target center point of the droplet, consisting of a droplet offset,
(ii) the arm moves downward to the target center point of the droplet, where the deposition is realized,
(iii) a gas pre-flow is started,
(iv) the arc process starts,
(v) while the arc process is on, the arm moves upwards at a certain welding speed in the build direction for a certain seam height,
(vi) the arc process ends,
(vii) a gas post-flow starts, protecting the weld as it solidifies,
(viii) the arm moves towards the next center point of the droplet, while the previous droplet uses this time until the next deposition as cooling time.

During the fabrication, it is assumed the realization of more specimens per time, ensuring the necessary cooling time until the next droplet on top of it, thereby making the overall build-up process faster. The process is repeated for a fixed number of iterations to obtain subsequent layers until the target height is reached.

The cooling time is related to the mass of bars and the distance to the cooling plate because it changes layer by layer, as a result the cooling time increases proceeding upwards, hence the heat transfer speed changes over time, which is taken into consideration to ensure that the time to realize all the next droplets until the new droplet on top of it is enough to guarantee the cooling time of that one (Silvestru 2021).

The thermal changes are not recorded, therefore the cooling time was not optimized, however the time placed between depositions was used for the production time of the next bars on the same layer, hence there was no idle time.

5.4. The robotic tool-path planning

For each printed element, a digital model is created with Rhinoceros, and its plug-in Grasshopper, from which the points coordinates, defining step by step the position of the welded layer, are defined.

The fabrication of specimens is possible setting a path-planning, essentially to send the relevant information to the UR16e and Fronius for welding.

The sequential steps are:

(i) Definition of the global refence system, to collocate the robotic arm and the whole setup for the printing process,
(ii) Definition of TCP (Tool Center Point) and target planes,
(iii) Process parameters setup,
(iv) Slicing of curves to obtain the points with assigned coordinates in the global reference system,
(v) Dot-by-dot printing process.

The robot tool, or Tool Center Point (TCP), is the point used to move the robot to a cartesian position (such as a Cartesian target). It corresponds to the definition of a reference system collocated on the nozzle of the UR16e, in order to print in the right location of the curve points, defined as follow.

The target planes represent the coordinates within the reference system to communicate the position to be assumed by the TCP, referring both on the droplet central point and on a offset target point in the build direction.

The information about the location in which there will be the deposition of each point, and the related offset for transfer operation, is extracted by means of planes slicing the whole specimen; the plane position into the global reference system is based on the layer height (printing process parameter). Furthermore, it is essential to take into consideration possible uncertainties and error, due to intrinsic inaccuracy of the printing process: each point of the digital model has a real counterpart whose position is not exactly the one of the digital model (V. P. Laghi 2020b).

The points in the Figure 5.1 represent the location of the droplets. The definition of their coordinates within the global reference system allows to locate and print them. Starting from the designed geometry, the points are captured by setting a division distance between each welding point correlated to the layer height set on the source power, 1 mm, to convert the input into an executable toolpath. Then, the offset points location is defined starting from the droplet coordinates, assuming an offset value, in order to ensure the transfer operations. The coordinates are transferred to the robotic arm controller by means of commands, corresponding to the TCP locations, with an additional information related to the welding phase.

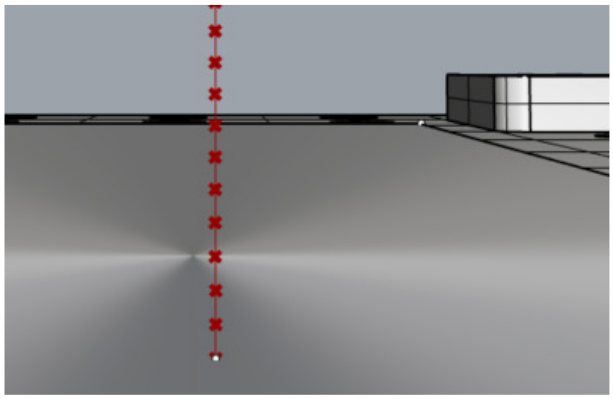

Figure 5.1 Each cross represents the point in which the deposition of the droplet is done. Their coordinates are used for the printing process.

The toolpath for each point in the Figure 5.1 consists of five major steps: approach in normal direction of the plane, a wait while the arc is burning, the welding point itself, a wait after the welding process for cooling and a departure in normal direction. Hence, the robot receives five target planes and five robot commands: the first one sends information about the coordinates within the reference system, the latter sends information about the activation of the welding torch, as follow:

(i) False,
(ii) True
(iii) Wait
(iv) False
(v) False.

False represents no welding, the opposite for true, while wait indicates information about the time required for welding, which can vary related to each application.

Then, the robot moves to the next position. In between the welding points, the robot moves in a linear motion to avoid collisions with the printed structure.

5.5. Printing process parameters

The CMT standard setup allows controlling a large number of process parameters (Fronius International GmbH). The following welding process parameters were taken into account in this work: wire diameter, wire feed speed (Wfs), current (I), voltage (U), arc-length correction, inching value, start, slope, end current, gas pre and post flow. Table 5.1 shows the adapted welding process parameters, it consists of input parameters set on the Fronius TPS 600i, and output parameters set during the printing process. Table 5.2-5.3 shows the constant welding, motion and geometric parameters set on Fronius TPS 600i.

The shielding gas used as gas pre and post flow was pure Argon (Ar) and 15-20% of carbon dioxide (CO_2), also known as M21, applied with a constant flow of 15 l/min.

The Tables 5.1, 5.2 and 5.3 show the printing process adopted for the different outcomes.

Series	**Number of bars printed as a group**	**Input process parameters**			**Output process parameters**	
		Current	**Voltage**	**Wfs**	**Welding time**	**Robot speed**
		I [A]	U [V]	[m/min]	[s]	[mm/s]
Straight bars 11cm	5	108	13.7	3	1.1	1500
Straight bars 16cm	6	108	13.7	3	1.1-1.11	1500
Straight bars – different welding time	3	108	13.7	3	1.1	1500
	3	108	13.7	3	1.2	1500
	3	108	13.7	3	1.3	1500
	3	108	13.7	3	1.4	1500
Crossed bars	-	108	13.7	3	1.15	1500
WAAMGrid mock-up	-	108	13.7	3	1.15-1.18	1500
WAAMGrid demonstrator	-	108	13.7	3	1.2	1500-1800

Table 5.1 Adapted process parameters for each series.

Series	Wire diameter	Layer height	Seam height	Welding speed	Arc-length correction	Inching value
-	[mm]	[mm]	[mm]	[mm/s]	-	[m/min]
Straight bars 11cm	1.2	1.0	1.0	1.0	-2.0	3.0
Straight bars 16cm	1.2	1.0	1.0	1.0	-2.0	3.0
Straight bars – different welding time	1.2	1.0	1.0	1.0	-2.0	3.0
Crossed bars	1.2	1.0	1.0	1.0	-2.0	3.0
WAAMGrid mock-up	1.2	1.0	1.0	1.0	-2.0	3.0
WAAMGrid demonstrator	1.2	1.0	1.0	1.0	-2.0	3.0

Table 5.2 Welding, motion and geometric parameters for all series (1).

Series	Starting current	Start current time	Slope 1 and 2	End current	Gas pre flow	Gas post flow
-	[%]	[s]	[s]	[%]	[s]	[s]
Straight bars 11cm	135.0	0.2	1.0	50.0	0.5	3.0
Straight bars 16cm	135.0	0.2	1.0	50.0	0.5	3.0
Straight bars – different welding time	135.0	0.2	1.0	50.0	0.5	3.0
Crossed bars	135.0	0.2	1.0	50.0	0.5	3.0
WAAMGrid mock-up	135.0	0.2	1.0	50.0	0.5	3.0
WAAMGrid demonstrator	135.0	0.2	1.0	50.0	0.5	2.0

Table 5.3 Welding, motion and geometric parameters for all series (2).

The WAAM-produced specimens are classified based on their topological configuration and process parameters. In the subsequent Section 5.6, each series is analyzed in detail. Focus is on the output process parameters, the ones directly controlled during the printing process by means of Grasshopper and its components. The combination of the controlling parameters affects the printing quality (geometrical precision and surface roughness) as well as the material mechanical properties. The welding time refers to the continuous time in which there is the wire welding, its change produces a different final outcome, in terms of both diameter and mechanical response.

5.6. Description of the test specimens

The WAAM-produced specimens are:

- *straight bars* to test the different printing process parameters and cooling time in order to reach the target diameter and more precision in the bars straightness,
- *crossed bars* to study the response in case of longitudinal axis of the rod inclined with respect to the build direction (the nozzle is perpendicular to the substrate), moreover to test the printing process parameters in relation to the intersection point, obtaining its optimal creation,
- *diagrid column mock-up*, as a test of the bigger final 3D-printed diagrid column, in order to apply what was tested in the two previous WAAM-produced specimens,
- *WAAMGrid Demonstrator*: it is designed as a 12 m high diagrid column with a diameter of 54.64cm.

5.6.1. WAAM-produced straight bars

(i) Straight bars of 11 cm

The WAAM bars are printed as a group of five, in order to take an advantage from the cooling time. The cooling time and the robotic tool-path affect the overall printing time, influenced by the robot speed. Tables 5.4, 5.5 and 5.6 display the adopted process parameters.

Series	**Number of bars printed as a group**	**Input process parameters**			**Output process parameters**	
		Current	**Voltage**	**Wfs**	**Welding time**	**Robot speed**
		I [A]	U [V]	[m/min]	[s]	[mm/s]
Straight bars 11cm	5	108	13.7	3	1.1	1500

Table 5.4 Adapted process parameters for straight bars of 11 cm.

Series	Wire diameter	Layer height	Seam height	Welding speed	Arc-length correction	Inching value
-	[mm]	[mm]	[mm]	[mm/s]	-	[m/min]
Straight bars 11cm	1.2	1.0	1.0	1.0	-2.0	3.0

Table 5.5 Welding, motion and geometric parameters for straight bars of 11 cm (1).

Series	Starting current	Start current time	Slope 1 and 2	End current	Gas pre flow	Gas post flow
-	[%]	[s]	[s]	[%]	[s]	[s]
Straight bars 11cm	135.0	0.2	1.0	50.0	0.5	3.0

Table 5.6 Welding, motion and geometric parameters for straight bars of 11 cm (2).

In the Table 5.5, the layer height is set to 1 mm, it means that the welding process should produce a metal droplet of 1 mm. Each point of the digital model has a real counterpart whose position is not exactly the one of the digital model, due to intrinsic inaccuracy of the printing process. It is balanced by changing the spacing between two subsequent points, therefore, the layer height is 1 mm based on the input process parameters, while the point coordinates are obtained by the hypothesis to have a variable points spacing, in particular starting with the input value of 1 mm, then adopting smaller values up to 0.8 mm with a set reduction of 0.05 mm (Table 5.7).

Layer height	
1 mm	First 5 layers (base)
Step of 0.05 mm	From layer 6 up to reach 0.8 mm
0.8 mm	Remaining part (top)

Table 5.7 Layer height along the straight bars of 11 cm going upward.

Figure 5.2 Straight bars of 11 cm

(ii) Straight bars of 16 cm

The information related to the cooling time and the robotic tool-path applied to the previous WAAM elements are replicated in this case, also referring to both the printing path and the layer height.

The WAAM bars are printed as a group of six. Tables 5.8, 5.9 and 5.10 display the adopted process parameters.

Series	**Number of bars printed as a group**	**Input process parameters**			**Output process parameters**	
		Current	**Voltage**	**Wfs**	**Welding time**	**Robot speed**
		I [A]	U [V]	[m/min]	[s]	[mm/s]
Straight bars 16cm	6	108	13.7	3	1.1-1.15	1500

Table 5.8 Adapted process parameters for straight bars of 16 cm.

Series	Wire diameter	Layer height	Seam height	Welding speed	Arc-length correction	Inching value
-	[mm]	[mm]	[mm]	[mm/s]	-	[m/min]
Straight bars 16cm	1.2	1.0	1.0	1.0	-2.0	3.0

Table 5.9 Welding, motion and geometric parameters for straight bars of 16 cm (1).

Series	Starting current	Start current time	Slope 1 and 2	End current	Gas pre flow	Gas post flow
-	[%]	[s]	[s]	[%]	[s]	[s]
Straight bars 16cm	135.0	0.2	1.0	50.0	0.5	3.0

Table 5.10 Welding, motion and geometric parameters for straight bars of 16 cm (2).

In the Table 5.9, the layer height is set to 1 mm. The Table 5.11 presents the variable points spacing along the bars.

Layer height	
1 mm	First 5 layers (base)
Step of 0.05 mm	From layer 6 up to reach 0.8 mm
Step of 0.02 mm	From 0.8 mm up to 0.7 mm
0.7 mm	From layer 100 up to the top

Table 5.11 Layer height along the straight bars of 16 cm going upward.

These WAAM straight bars were printed with a different welding time, in order to assess the printing process parameters to manufacture the best outcomes. The welding time was changed proceeding upwards (from 1.1 s to 1.15 s) in order to test possible benefits related to the layer height discrepancy.

Figure 5.3 Straight bars of 16 cm.

(iii) Straight bars with different welding time

The information related to the cooling time and the robotic tool-path applied to the previous WAAM elements are replicated in this case, also referring to both the printing path and the layer height.

In this case the aim is to compare four types of WAAM single bars, they are different in terms of welding time, from 1.1 s up to 1.4 s, with a step of 0.1 s.

The WAAM bars are printed as a group of three. Tables 5.12, 5.13 and 5.14 display the adopted process parameters.

Series	Number of bars printed as a group	Input process parameters			Output process parameters	
		Current	Voltage	Wfs	Welding time	Robot speed
		I [A]	U [V]	[m/min]	[s]	[mm/s]
Straight bars – different welding time	3	108	13.7	3	1.1	1500
	3	108	13.7	3	1.2	1500
	3	108	13.7	3	1.3	1500
	3	108	13.7	3	1.4	1500

Table 5.12 Adapted process parameters for straight bars with different welding time.

Series	Wire diameter	Layer height	Seam height	Welding speed	Arc-length correction	Inching value
-	[mm]	[mm]	[mm]	[mm/s]	-	[m/min]
Straight bars – different welding time	1.2	1.0	1.0	1.0	-2.0	3.0

Table 5.13 Welding, motion and geometric parameters for straight bars with different welding time (1).

Series	Starting current	Start current time	Slope 1 and 2	End current	Gas pre flow	Gas post flow
-	[%]	[s]	[s]	[%]	[s]	[s]
Straight bars – different welding time	135.0	0.2	1.0	50.0	0.5	3.0

Table 5.14 Welding, motion and geometric parameters for straight bars with different welding time (2).

In the Table 5.13, the layer height is set to 1 mm. The Tables 5.15, 5.16, 5.17 and 5.18 present the variable points spacing along the bars, highlighting the different settings due to different welding time. A change in welding time produces a different metal droplet, in terms of layer height and final diameter.

Layer height	
1 mm	First 2 layers (base)
Step of 0.05 mm	From layer 3 up to reach 0.85 mm
0.85 mm	Remaining part (top)

Table 5.15 Layer height along the straight bars with welding time of 1.1 s.

Layer height	
1 mm	First 4 layers (base)
0.95 mm	From layer 5 to 8
0.9 mm	From layer 9 to 16
0.85 mm	Remaining part (top)

Table 5.16 Layer height along the straight bars with welding time of 1.2 s.

Layer height	
1.1 mm	First 10 layers (base)
1 mm	From layer 11 to 20
0.95 mm	From layer 21 to 50
0.9 mm	From layer 51 to 80
0.85 mm	Remaining part (top)

Table 5.17 Layer height along the straight bars with welding time of 1.3 s.

Layer height	
1.1 mm	First 10 layers (base)
1 mm	From layer 11 to 20
0.95 mm	From layer 21 to 50
0.9 mm	From layer 51 to 80
0.85 mm	Remaining part (top)

Table 5.18 Layer height along the straight bars with welding time of 1.4 s.

5.6.2. WAAM-produced crossed bars (column grid)

The information related to the cooling time and the robotic tool-path applied to the previous WAAM elements are replicated in this case, also referring to both the printing path and the layer height. The difference is the model for which the printing process parameters were studied ensuring inclined bars with less irregularities and a well-created intersection point. The tool-path is planned to weld the points in a counterclockwise way.

Figure 5.4 Crossed bars: column grid.

Tables 5.19, 5.20 and 5.21 display the adopted process parameters.

Series	**Number of bars printed as a group**	**Input process parameters**			**Output process parameters**	
		Current	**Voltage**	**Wfs**	**Welding time**	**Robot speed**
		I [A]	U [V]	[m/min]	[s]	[mm/s]
Crossed bars	-	108	13.7	3	1.15	1500

Table 5.19 Adapted process parameters for crossed bars (column grid).

Series	Wire diameter	Layer height	Seam height	Welding speed	Arc-length correction	Inching value
-	[mm]	[mm]	[mm]	[mm/s]	-	[m/min]
Crossed bars	1.2	1.0	1.0	1.0	-2.0	3.0

Table 5.20 Welding, motion and geometric parameters for crossed bars (column grid) (1).

Series	Starting current	Start current time	Slope 1 and 2	End current	Gas pre flow	Gas post flow
-	[%]	[s]	[s]	[%]	[s]	[s]
Crossed bars	135.0	0.2	1.0	50.0	0.5	3.0

Table 5.21 Welding, motion and geometric parameters for crossed bars (column grid) (2).

The welding time is 1.15 s, higher with respect to the previous specimens, this is performed in order to create a bigger rod diameter, withstand the bar inclination and ensure the creation of the node.

In the Table 5.20, the layer height is set to 1 mm. The Table 5.22 presents the variable points spacing along the rods.

Layer height	
1.1 mm	First 4 layers (base)
1.05 mm	From layer 5 to 8
1 mm	From layer 9 to 13
0.95 mm	From layer 14 to 18
0.9 mm	From layer 19 to 28
0.85 mm	From layer 29 to 48
0.8 mm	Remaining part (top)

Table 5.22 Layer height along the crossed bars going upward.

5.6.3. 3D-printed Diagrid column - WAAMGrid mock-up

The information related to the cooling time and the robotic tool-path applied to the previous WAAM elements are replicated in this case, also referring to both the printing path and the layer height. The difference is the model for which the printing process parameters were studied ensuring inclined bars with less irregularities and a good intersection point. The tool-path is planned to weld the points in a counterclockwise way.

The WAAMGrid mock-up represents the scaled diagrid column designed in the Section 4.6, the 3 m high hyperboloidal diagrid column with 15 control cross-sections and a maximum cross-sectional radius of 0.4 m, in order to assess the feasibility of this outcome.

The final model is established, however the mock-up dimensions are evaluated following three assumptions:

(i) Total height of 50 cm,
(ii) Minimum radius (middle cross-section) of 3.5 cm,
(iii)Control cross-sections number.

Therefore the obtained mock-up model is as follows:

(i) Bottom and top control cross-sections radius: 6.6 cm,
(ii) Minimum radius: 3.5 cm,
(iii)Total height: 50 cm.

The Figure 5.5 shows the presented final design. The rod-like elements located at the bottom of the column are realized only for a manufacturing purpose, in order to guarantee no damages to the column during the removal phase from the supporting plate. These bars are 1 cm high.

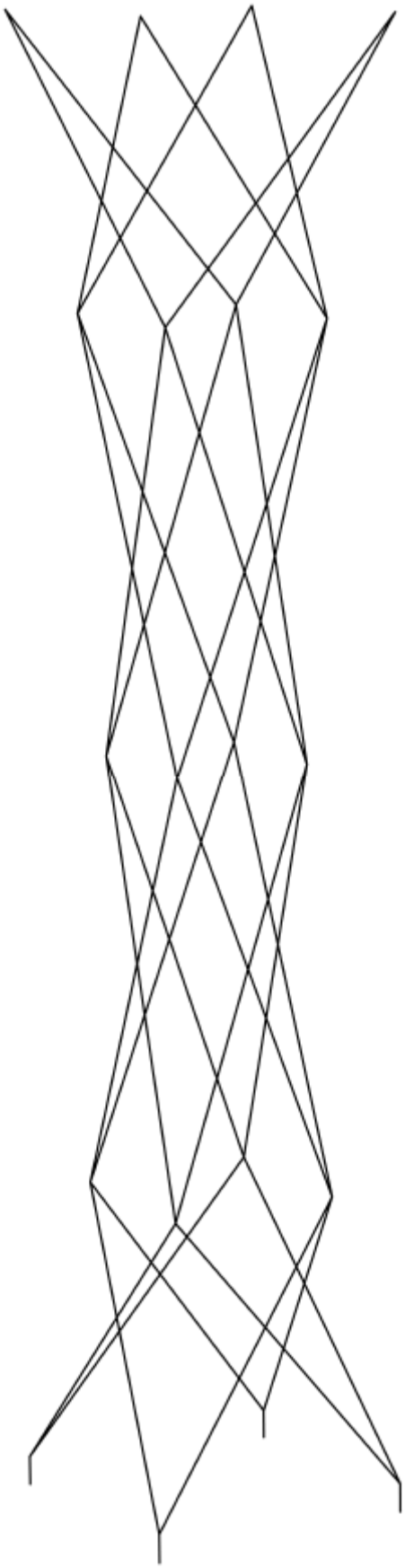

Figure 5.5 WAAMGrid (diagrid column) mock-up configuration.

Tables 5.23, 5.24 and 5.25 display the adopted process parameters.

Series	Number of bars printed as a group	Input process parameters			Output process parameters	
		Current	Voltage	Wfs	Welding time	Robot speed
		I [A]	U [V]	[m/min]	[s]	[mm/s]
WAAMGrid mock-up	-	108	13.7	3	1.15-1.18	1500

Table 5.23 Adapted process parameters for WAAMGrid Diagrid column mock-up.

Series	Wire diameter	Layer height	Seam height	Welding speed	Arc-length correction	Inching value
-	[mm]	[mm]	[mm]	[mm/s]	-	[m/min]
WAAMGrid mock-up	1.2	1.0	1.0	1.0	-2.0	3.0

Table 5.24 Welding, motion and geometric parameters for WAAMGrid Diagrid column mock-up (1).

Series	Starting current	Start current time	Slope 1 and 2	End current	Gas pre flow	Gas post flow
-	[%]	[s]	[s]	[%]	[s]	[s]
WAAMGrid mock-up	135.0	0.2	1.0	50.0	0.5	3.0

Table 5.25 Welding, motion and geometric parameters for WAAMGrid Diagrid column mock-up (2).

The welding time is 1.15 s as established for the crossed bars, increased to 1.18 s in correspondence of the layers close to the intersection point, ensuring the creation of the node. The increased welding time is adopted to realize subsequent welding points starting from 6 layers before the joint keeping the same value for the subsequent 12 layer.

In the Table 5.24, the layer height is set to 1 mm. The Table 5.26 presents the variable points spacing along the rods.

Layer height	
1 mm	First 5 layers (base)
0.95 mm	From layer 6 to 20
0.9 mm	From layer 21 to 45
0.85 mm	Remaining part (top)

Table 5.26 Layer height along the WAAMGrid Diagrid column mock-up.

The final outcome is presented in the Figures 5.6, 5.7 and 5.8.

Figure 5.6 3D-printed Diagrid column - WAAMGrid mock-up (a).

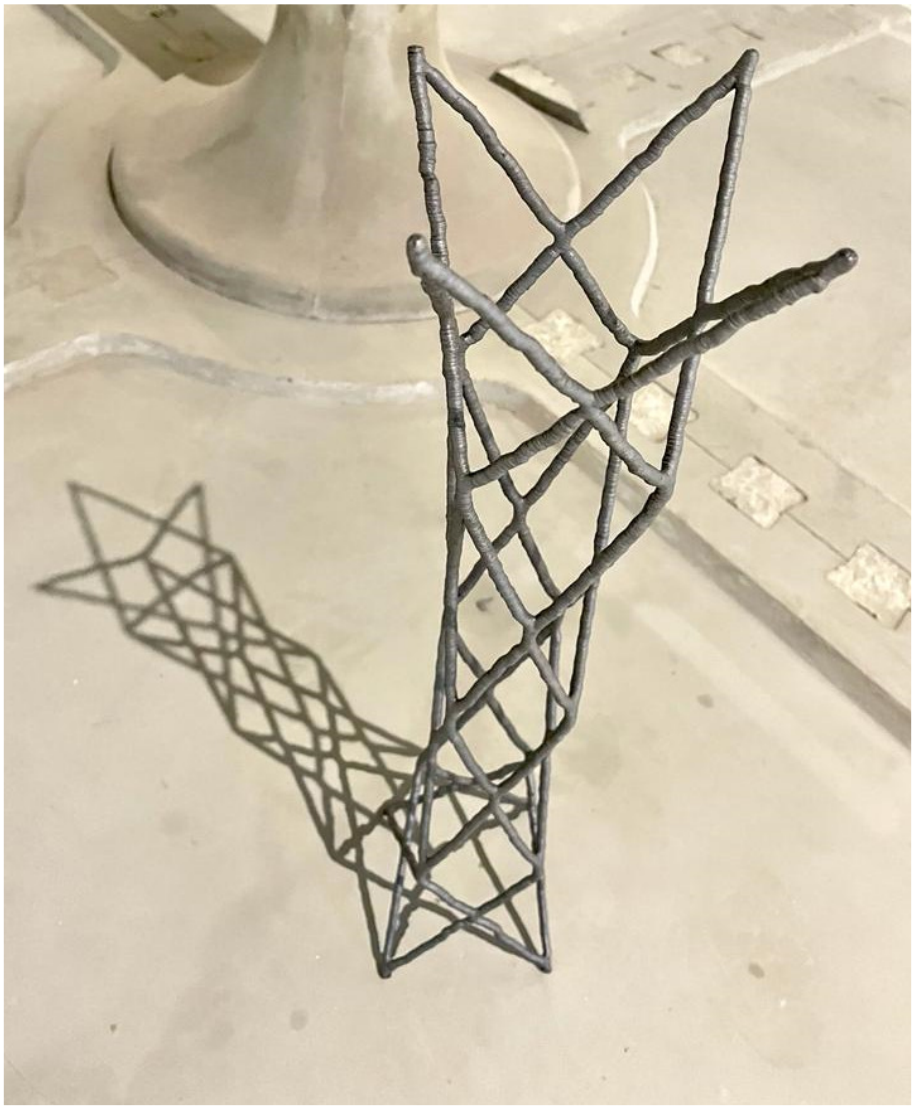

Figure 5.7 3D-printed Diagrid column - WAAMGrid mock-up (b).

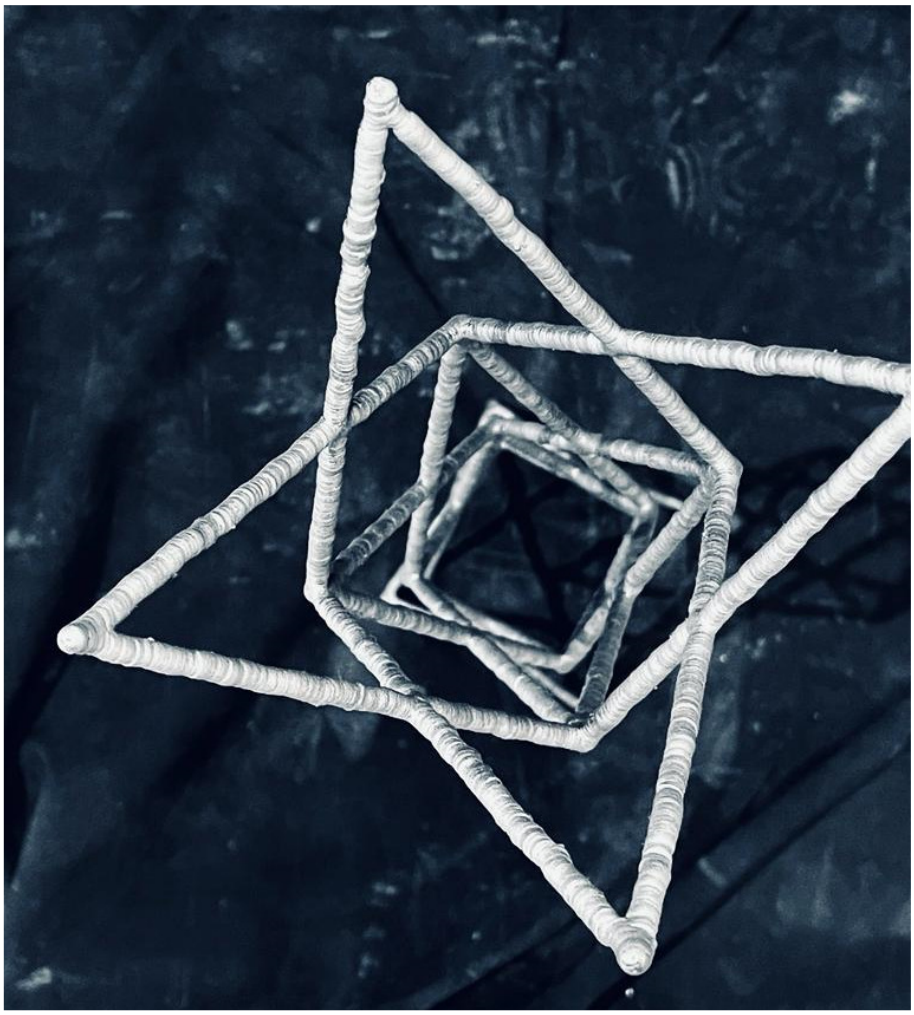

Figure 5.8 3D-printed Diagrid column - WAAMGrid mock-up (c).

5.6.4. 3D-printed Diagrid column - WAAMGrid Demonstrator

An infilled 3D-printed diagrid column is realized with the highest possible dimensions, based on the Universal Robot (UR16e) constraints.

The presented work is referred to as a "Demonstrator", because the outcome is a portion of the whole designed diagrid column. The acquired know-how related to tool-path and printing process parameters is adopted here.

5.6.4.1. WAAMGrid Demonstrator – Design

The starting point is the final design of a diagrid column presented in the Section 0, on which a scale factor is applied in order to achieve the objective of 12 m high column with 13 control cross-sections.

The final model is established following three assumptions:

(iv) Total height of 12 m,
(v) Minimum radius (middle cross-section) of 0.1 m,
(vi) Control cross-sections number: 17.

Therefore, the obtained model is as follows:

(iv) Bottom and top control cross-sections radius: 0.27 m,
(v) Minimum radius: 0.1 m,
(vi) Total height: 12 m.

Then, starting from the control cross-sections geometry, a radial grid was created by assuming the number of grid cells in both radial and polar directions, obtaining the points at grid nodes for each cross-section, as shown in the Figure 5.9.

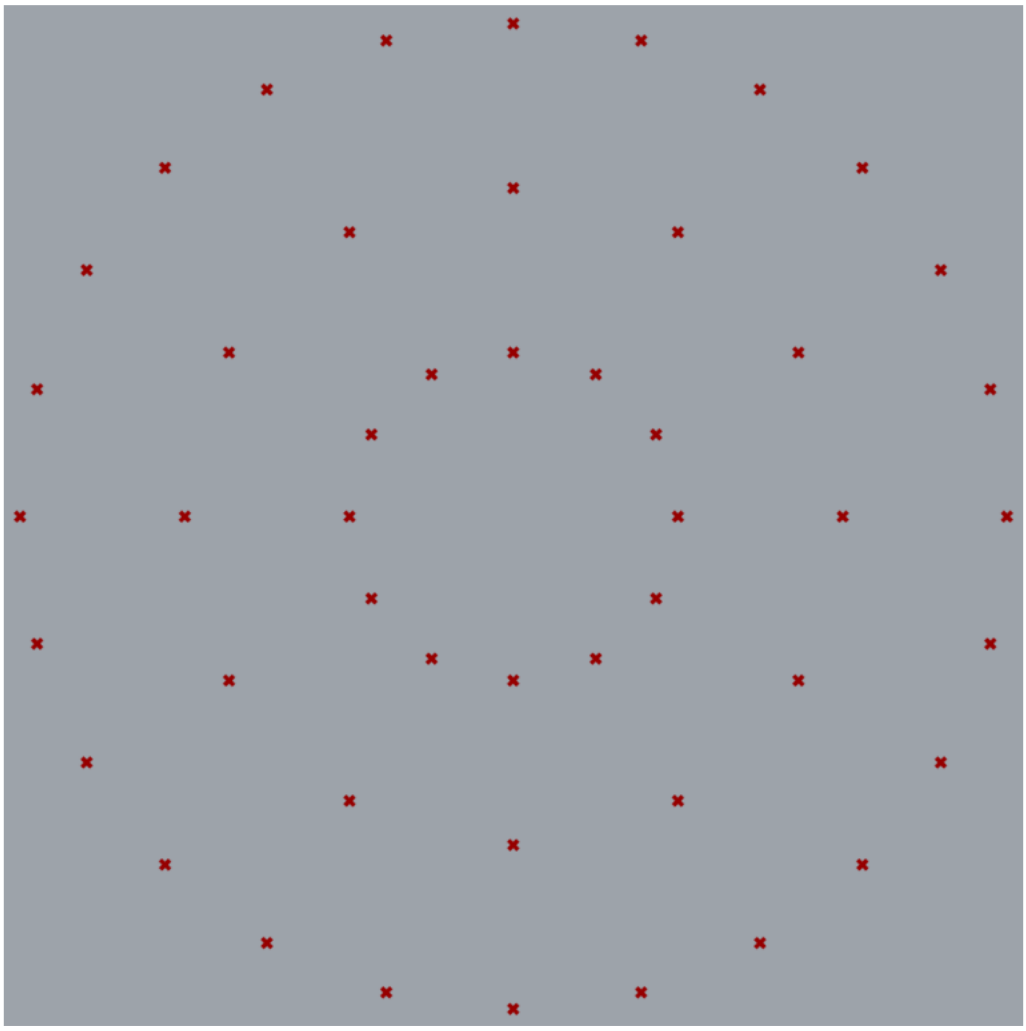

Figure 5.9 3D-printed Diagrid column (WAAMGrid Demonstrator) - Points at grid nodes.

The following step was the creation of the external diagrid lattice surface, as the one designed in the Section 0, the same approach is applied to the internal circumference, resulting in an internal diagrid lattice structure. An intermediate circumference was added between the others enabling the realization of inclined rods following the manufactural constraints (inclination and length). The series of rods connect the point of one circle to the shifted one of the closer circle above: hence, one rod joins two points, the first on the outer circumference and the second on the intermediate one, repeating the same for the intermediate and inner ones. These rods are necessary to connect and support the two diagrid structures.

The final model is presented in the Figure 5.10.

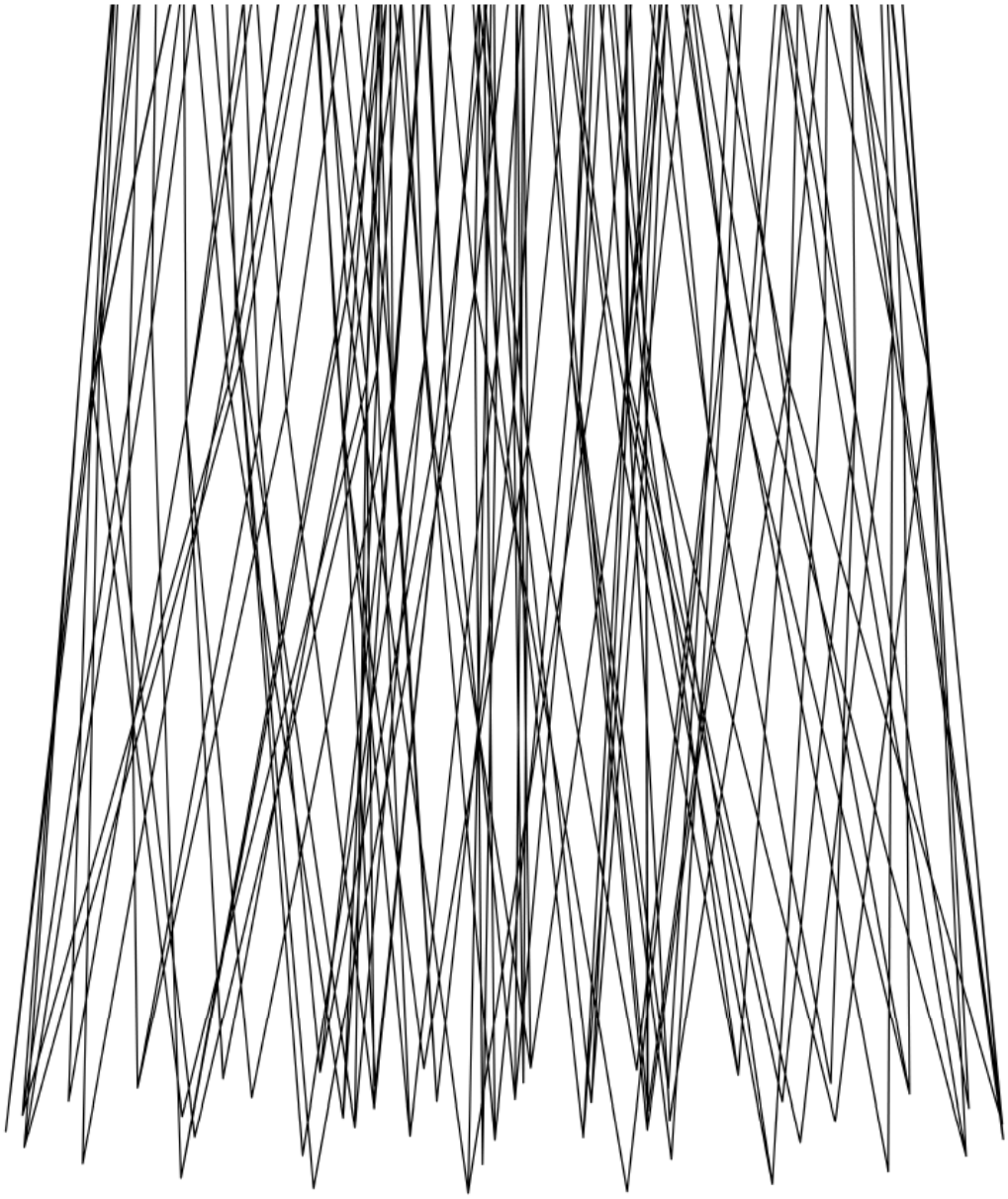

Figure 5.10 3D-printed Diagrid column (WAAMGrid Demonstrator) – configuration.

The outcome is printed by means of 120 welding points per each layer, realizing the designed diagrid elements.

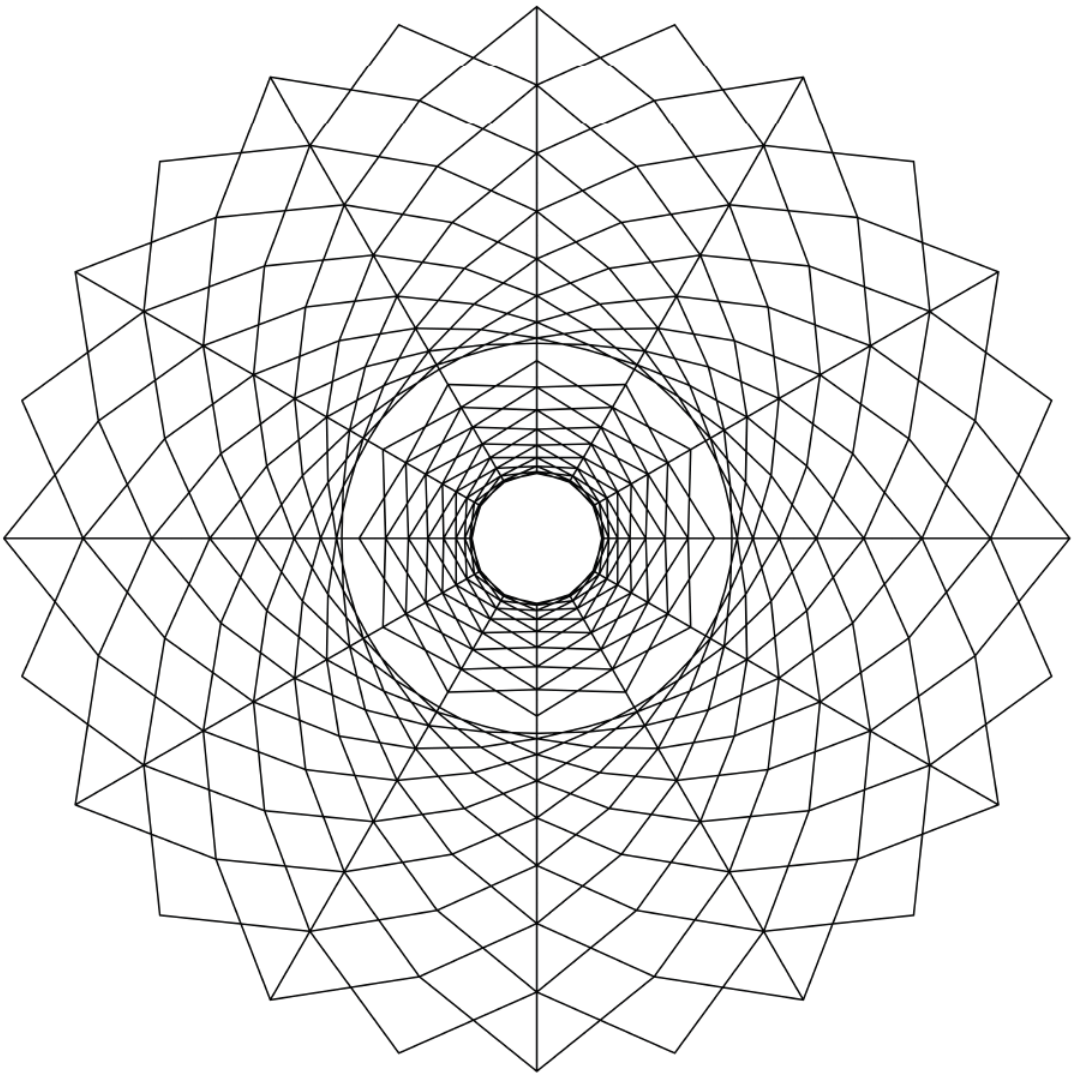

Figure 5.11 3D-printed Diagrid column (WAAMGrid Demonstrator) - Top view.

5.6.4.2. WAAMGrid Demonstrator – Manufacturing

Tables 5.27, 5.28 and 5.29 display the adopted process parameters.

Series	Number of bars printed as a group	Input process parameters			Output process parameters	
		Current	Voltage	Wfs	Welding time	Robot speed
		I [A]	U [V]	[m/min]	[s]	[mm/s]
WAAMGrid demonstrator	-	108	13.7	3	1.2	1500-1800

Table 5.27 Adapted process parameters for WAAMGrid Diagrid column Demonstrator.

Series	Wire diameter	Layer height	Seam height	Welding speed	Arc-length correction	Inching value
-	[mm]	[mm]	[mm]	[mm/s]	-	[m/min]
WAAMGrid demonstrator	1.2	1.0	1.0	1.0	-2.0	3.0

Table 5.28 Welding, motion and geometric parameters for WAAMGrid Diagrid column Demonstrator (1).

Series	Starting current	Start current time	Slope 1 and 2	End current	Gas pre flow	Gas post flow
-	[%]	[s]	[s]	[%]	[s]	[s]
WAAMGrid demonstrator	135.0	0.2	1.0	50.0	0.5	2.0

Table 5.29 Welding, motion and geometric parameters for WAAMGrid Diagrid column Demonstrator (2).

The welding time is 1.2 s in order to guarantee inclined bars with less irregularities and a well-created intersection point.

In the Table 5.28, the layer height is set to 1 mm. The Table 5.30 presents the variable points spacing along the rods. In this case, the wider variability associated to the layer height is due to two different situations:

(i) The layer height is higher at the beginning (equal to the assumed layer height) and when there is the superimposition of more than one point, where more lines are approaching the same point, which is assumed at the beginning when the lines start from the same node, and then when the lines converge in one point (node),

(ii) The layer height is smaller further from the nodes, where it is affected by the error, due to intrinsic inaccuracy of the printing process.

Layer height	
1 mm	First 6 layers (base)
1.1 mm	From layer 7 to 11
1 mm	From layer 12 to 19
1.05 mm	From layer 20 to 21
1.1 mm	From layer 22 to 26
1 mm	From layer 27 to 60
0.95 mm	From layer 61 to 80
0.9 mm	From layer 81 to 100
0.85 mm	From layer 101 to 116
0.8 mm	From layer 117 to 256
1 mm	From layer 257 to 259
1.1 mm	From layer 260 to 272
1 mm	From layer 273 to 276
0.9 mm	From layer 277 to 284
0.8 mm	Remaining part (top)

Table 5.30 Layer height along the WAAMGrid Diagrid column Demonstrator.

Figure 5.12 3D-printed Diagrid column (WAAMGrid Demonstrator) - Column base and welding torch.

The rod-like elements located at the bottom of the column are realized only for a manufacturing purpose, in order to guarantee no damages for the column during the removal phase from the supporting plate. These bars are 1 cm high.

5.6.4.3. WAAMGrid Demonstrator – Dimensions

The final dimensions of the WAAMGrid Demonstrator, the bottom cross-section diameter and the reached height, are related to the constraints of UR16e robotic arm, based on the possible movements of its shoulder, elbow and wrist.

The dimensions are:

D_{bottom}	55.1 cm
D_{upper}	48.6 cm
D_{bar}	4.83 mm
H_{tot}	32.15 cm

Table 5.31 3D-printed Diagrid column (WAAMGrid Demonstrator) - Outcome dimensions.

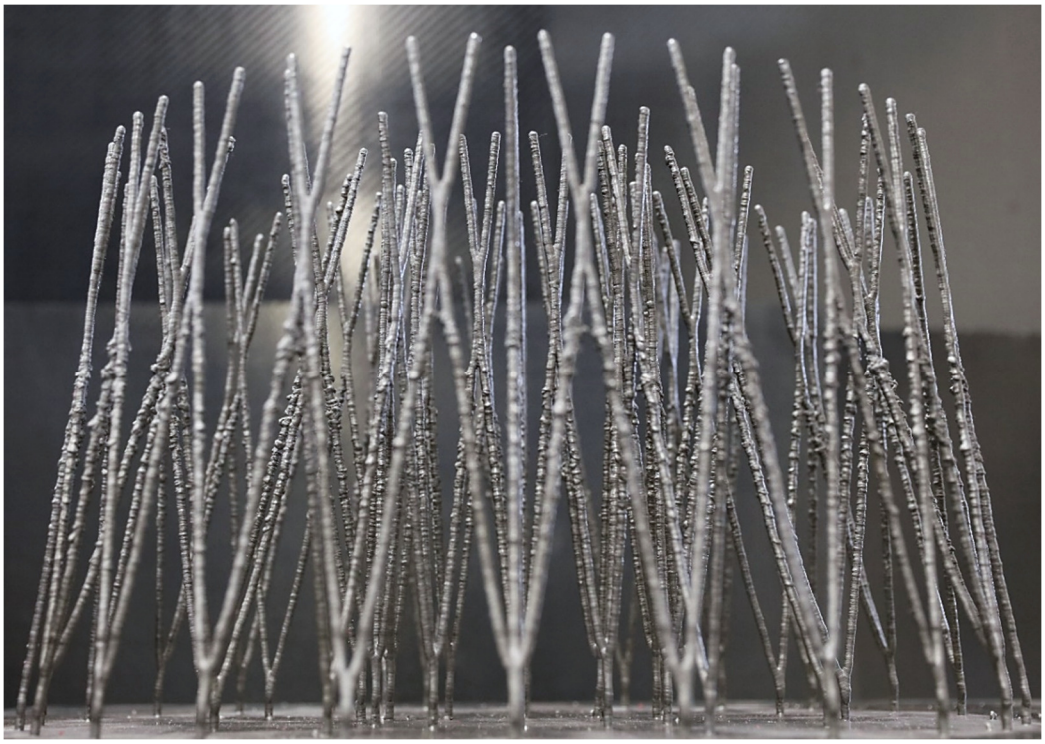

Figure 5.13 3D-printed Diagrid column (WAAMGrid Demonstrator) – Outcome.

The final outcome is presented in the Figure 5.14, and the ellipses allow to highlight the construction path.

(i) The red ellipses are the inner and outer circumferences, in addition, the rods close to these ellipses are approaching them to realize the intersection,

(ii) The green ellipses highlight the rods which are proceeding upward and will create a node at a certain height, higher than 32.15 cm.

The intersection between WAAM-produced rods is presented in the Figure 5.15.

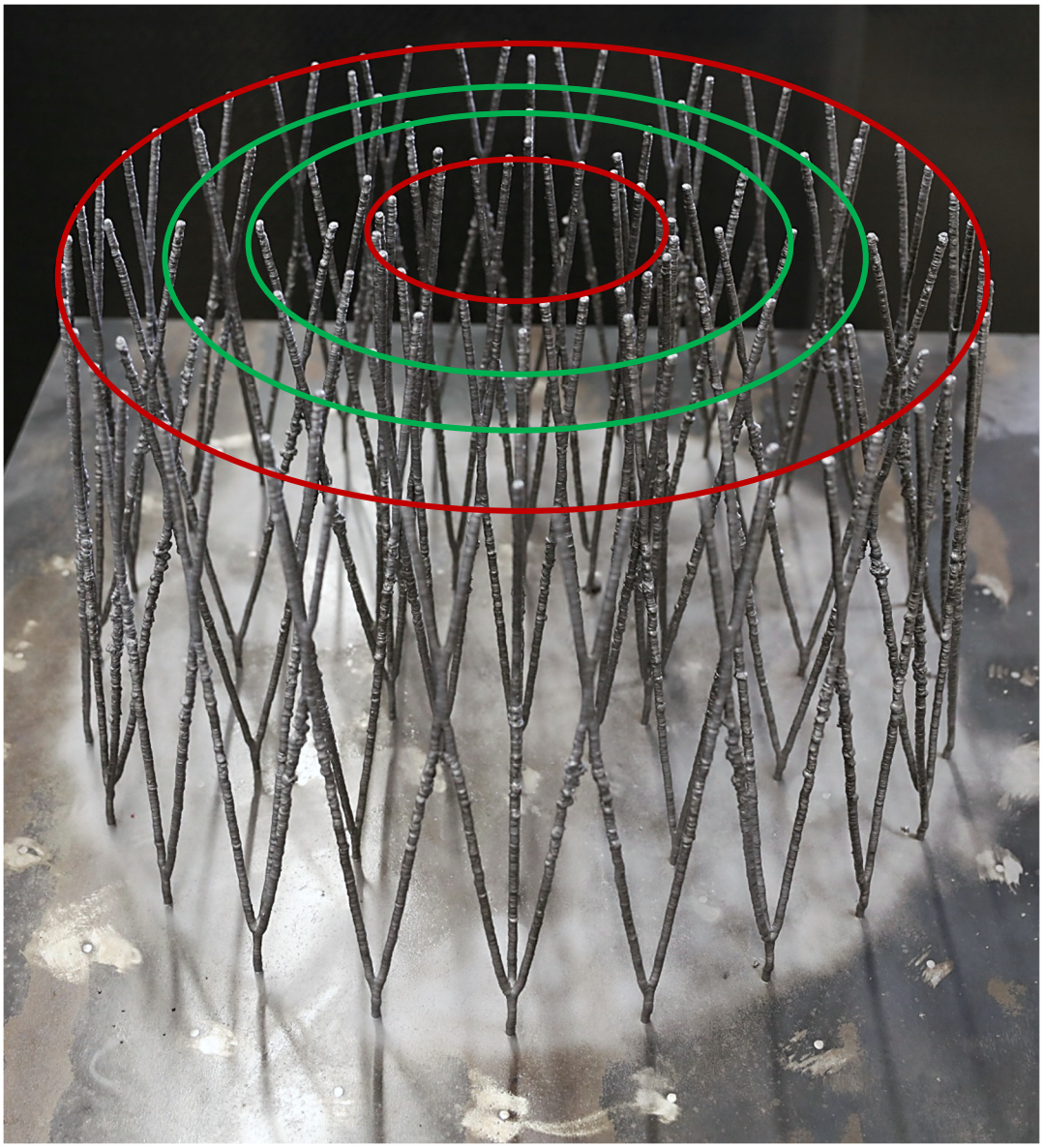

Figure 5.14 3D-printed Diagrid column (WAAMGrid Demonstrator) – The configuration is explained by ellipses.

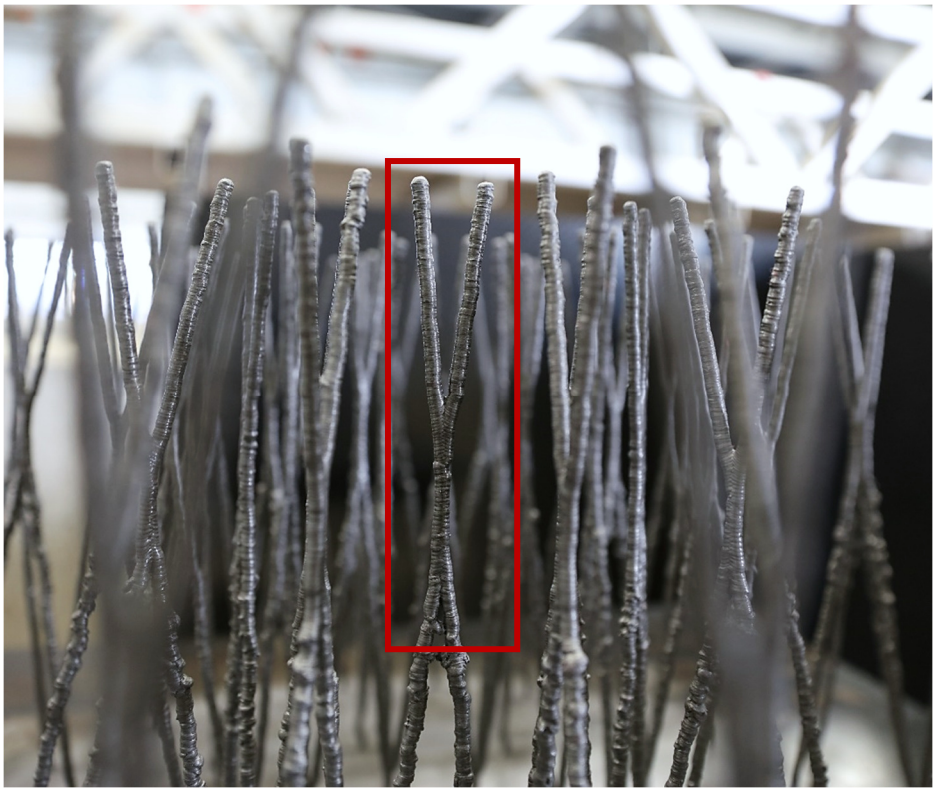

Figure 5.15 3D-printed Diagrid column (WAAMGrid Demonstrator) – Intersection.

5.7. Summary of Fabrication

The “dot-by-dot” printing deposition strategy enables to manufacture straight elements, developing the element in the vertical build direction with certain inclinations. The accuracy of the output is correlated to the adopted printing process parameters, in particular, the fixed layer heigh, set as an initial parameter, was not accomplished, resulting in a non-uniform addition of material, affecting the structure buildup Figure 5.16. During the buildup, the distance between the welding torch and the structure was not consistent with the digital model, this caused:

(i) the shielding gas coverage to be inadequate ruining the quality of the structure;
(ii) the welding parameters change, e.g. wire length;
(iii)collapsed gas bubbles slag and oxide on the weld causing the arc to fail.

The inaccuracies accumulated with each welding step led to a recursive error system and an unpredictable buildup of the structure. As a consequence, the arc is not able to ignite for the necessary amount of time to deposit the desired quantity of metal to the structure. This was managed with a direct approach adjusting the process and the division distance between welding points with a visual approach, based upon the wire length outside the nozzle, due to the adopted non-adaptive approach.

Figure 5.16 Example: inaccuracy of inconsistent buildup.

Moreover, the process efficiency is highly connected to the cooling time, as a key factor to optimize the required worktime. The objective is the arrangement of an optimized tool-path with no idle time, the cooling happens within the process,

the time slot is employed to produce the other welding points of the actual layer. Both the 3D-printed diagrid columns and column grid (Sections 0, 5.6.3, 0) have enough welding points per layer, requiring longer time compared to the cooling one. Focus is on the tool-path in case of more points on the same layer, in order to avoid welding of points too close, due to the minimum time required to restart the scheduled five commands, otherwise it impacts on the gas pre and post flow influencing the welded point in terms of both characterization and additional material. The same is required in case of straight bars (Section 0) for which the objective is to place them at the right distance for the same reason as before, moreover defining the number of bars printed at the same time in order to optimize the cooling time.

The robot speed is an output process parameter, it is established to be fast enough to realize larger structure optimizing the process and, at the same time, it should guarantee the accuracy of the process.

6. Experimental Characterization

6.1. Overview

The first WAAM applications were produced with the “continuous” printing deposition strategy, widely known and studied in the literature (T. L. Feucht 2019), (Gardner 2020), (Kyvelou 2020), (Rodrigues 2019), (Gordon 2018), (W. X. Wu 2019). On the other hand, the “dot-by-dot” strategy is innovative and with new applications (Joosten 2015), (Van Bolderen 2017), (Müller 2019), hence only preliminary studies have been developed, pointing out a non-negligible anisotropic behavior of the WAAM material, influenced by the relative direction of the main axis of the element with respect to the printing layer deposition.

ETH Zürich provided a research assessing the mechanical properties of the bars determined from uniaxial tensile tests on as-printed specimens and milled ones. The object was the use of this printing strategy to produce a novel efficient joining method for custom structural steel components (Silvestru 2021).

The research group, Laghi et al., at University of Bologna is performing an extensive campaign devoted to assess the key effective mechanical parameters of as-built WAAM-produced 304L stainless steel bars for structural design purposes. The mechanical characterization is supported by microstructural investigations and detailed studies on the geometrical features (V. P. Laghi 2021a), (V. P. Laghi 2022).

6.2. Mechanical response of dot-by-dot WAAM steel bars

The research performed on WAAM stainless steel bars is organized in different steps, in order to assess the influence of different build angles on the mechanical response. The work is divided in two phases, testing two types of specimens, the first ones are WAAM steel single bars, the second ones are WAAM steel crossed-bars.

The tested specimens were manufactured by MX3D (MX3D) with Gas Metal Arc Welding (GMAW). The ER308LSi stainless steel welding wire (1 mm diameter), supplied by Oerlikon (Oerlikon), was used as feedstock wire. The employed shield gas was 98% Ar and 2% CO_2. The printing process parameters are reported in Table 6.1.

Wire diameter	**Welding speed**	**Wfs**	**Gas flow rate**	**Current**	**Voltage**	**Deposition rate**
[mm]	[mm/s]	[m/min]	[L/min]	[A]	[V]	[kg/h]
1	15-30	4-8	10-20	100-140	18-21	0.5-2

Table 6.1 Printing process parameters provided by MX3D for "X rods".

The object is to account for the possible influence of the printing direction, with respect to the vertical axis, on the overall mechanical response of the printed bars. In this regard, three different build angles are considered (angle between the axis of the WAAM bar and the vertical axis, perpendicular to the base platform), and the nozzle angle (angle between the axis of the WAAM bar and the nozzle axis) was set equal to 0° for all batches. The specimens were printed with build angles equal to 0° (dot-0), 10° (dot-10) and 45° (dot-45). The two limit cases of build angles correspond to the common limit condition for practical applications.

The mechanical characterization of WAAM steel single bars was performed on different specimens through tensile, three-point bending and compression tests, buckling behavior. The results are aimed at evaluating the influence of both build

angle and geometrical irregularities (proper of the WAAM printing process) on the mechanical properties. The variation of the real diameter along the height of the bar (order of 0.5 mm) is due to the successive deposition of metal droplets. In addition, this also induces some lack of straightness due to inaccurate positioning of the torch.

Therefore, the result is a non-uniform circular cross-section and non-straight longitudinal axis. For this reason, a detailed geometrical characterization is carried out on two levels:

(i) A specimen-to-specimen characterization to assess the variability of the geometry within the same batch,

(ii) An inherent characterization on the single bar to assess the variability of the geometry along the element.

Instead of the use of advanced modelling, a simplified approach is adopted. The idea is to decouple the two main sources of variabilities: (i) geometrical data and (ii) mechanical material properties. General information on cross-sectional area are used for the interpretation of the mechanical tests (V. P. Laghi 2020b).

The mechanical tests are interpreted assuming an effective cross-sectional area constant along the element length, so that the axial stresses can be computed according to Euler-Bernoulli beam theory:

$$\sigma_{eff} = \frac{F}{A_{eff}} \tag{10}$$

$$\varepsilon_{eff} = \frac{\Delta L}{L_0} \tag{11}$$

Where:

- A_{eff} is an effective volume-equivalent cross-sectional area of the structural member,
- F is the tensile axial force,
- σ_{eff} is the effective stress, which differs from the true material stress, σ,
- L_0 indicates the undeformed initial length,
- ΔL indicates the elongation.

A_{eff} is derived using an average value as obtained from volumetric measurements on as-built specimens (Kyvelou 2020), (V. P. Laghi 2021b), (V. P. Laghi 2020b).

This criterion has the advantage of providing an integral value based on equal weight criterion. Therefore, the effective diameter is computed as:

$$d_{eff} = \sqrt{\frac{4A_{eff}}{\pi}} \tag{12}$$

The simplified approach allows to treat the cross-sectional area as a deterministic value, while all the uncertainties are collected in the effective axial stress, hence in the mechanical parameters only. In this way, the conventional approach adopted for the analysis and design of traditionally manufactured steel members has no variations, considering the geometrical parameters as deterministic values and the material strength parameters as random variables.

The following measuring systems are used to assess the main geometrical parameters of Wire-and-Arc Additive Manufactured elements:

- Digital caliper (with a nominal precision of 0.02 mm) for manual measures. Measurements of diameters are performed per each rod element at various locations, due to the surface roughness and lack of straightness, the final value is an average of them,
- Analogic hydraulic scale to take volume measurements from which the effective area, and corresponding diameter, are derived,
- 3D scanning acquisition system for the evaluation of cross-section irregularities, surface roughness and lack of straightness of the element.

Within the specimen-to-specimen characterization, the volume-equivalent cross-section was assumed as the resistant effective cross-sectional area for the calculation of the effective stresses from tensile tests (Kyvelou 2020), (V. P. Laghi 2020b). Then, the average effective diameters d_{eff} are shown in Table 6.2.

Specimen-to-specimen variability	
Specimen	**d_{eff} [mm]**
dot-0	5.92 ± 0.29
dot-10	5.71 ± 0.28
dot-45	6.40 ± 0.29

- *Table 6.2 Mean values and standard deviations of diameters for the tested bars: specimen-to-specimen variability (V. P. Laghi 2022).*

For all the batches, the coefficient of variation of the effective diameter was of around 5%. These results are in line with the WAAM bars studied by Silvestru et al. (Silvestru 2021).

The inherent geometrical characterization of the dot-0 and dot-45 3D-scanned bars is reported in Table 6.3 in terms of: ratios between the real and effective cross-sectional area (A_{real}/A_{eff}), diameter (d_{real}/d_{eff}), discrepancy between real and nominal diameter (d_{real}/d_n), out-of-roundness parameters (L_x/d_{real} and L_y/d_{real}), lack-of-straightness parameter (e/H).

Inherent geometrical irregularities						
Specimen	**A_{real}/A_{eff}** [-]	**d_{real}/d_{eff}** [-]	**L_x/d_{real}** [-]	**L_y/d_{real}** [-]	**d_{real}/d_n** [-]	**e/H** [%]
dot-0	0.98 ± 0.06	0.99 ± 0.03	1.02 ± 0.02	0.99 ± 0.02	0.98 ± 0.03	0.22 ± 0.12
dot-45	0.99 ± 0.06	0.99 ± 0.03	1.01 ± 0.03	1.00 ± 0.02	1.01 ± 0.03	0.28 ± 0.10

Table 6.3 Variability of the inherent geometrical irregularities (mean and standard deviation) (V. P. Laghi 2022).

The overall variability resulting from specimen-to-specimen and inherent variability is an important source of variability of the key effective mechanical parameters.

The 3D models of the threes bars (one dot-0, one dot-10 and one dot-45) were analyzed to quantify the variability of the local geometrical parameters. The variability registered for the dot-0 specimen resulted similar to the one of dot-10 specimen, hence they are reported as a single result. For each specimen, the distribution of the cross-sectional area was studied from the 3D scan and compared with the nominal cross-sectional area (A_n = 28.3 mm). Overall, the dot-45 and dot-0 present respectively, an higher mean value and a lower one with respect to the nominal one. The identification of the real longitudinal axis of the WAAM bars was performed by connecting the centroids of all sections. The dot-45 specimen has a higher irregularity with respect to the dot-0. These results are also similar to the one reported in the work of Silvestru et al. (Silvestru 2021).

6.2.1. Tensile tests

The tensile tests were performed on a total of 29 specimens (10 dot-0, 10 dot-10, and 9 dot-45).

The tensile tests were performed on a universal testing machine of 500 kN load capacity at the Structural Engineering labs of University of Bologna. The specimens were tested in displacement-control with a velocity corresponding to a load rate of 2 MPa/s according to (ISO6892-1 2009). The longitudinal elongation of each specimen was measured using a Linear Variable Differential Transformer (LVDT). A monitoring system weas adopted to evaluate the strains, a linear deformometer of gauge length of 50 mm to detect the linear deformation of the specimens up to yielding.

Figure 6.1 presents the effective stress-strain curve of WAAM single bars with different build angles, with a comparison of the results within the same batch.

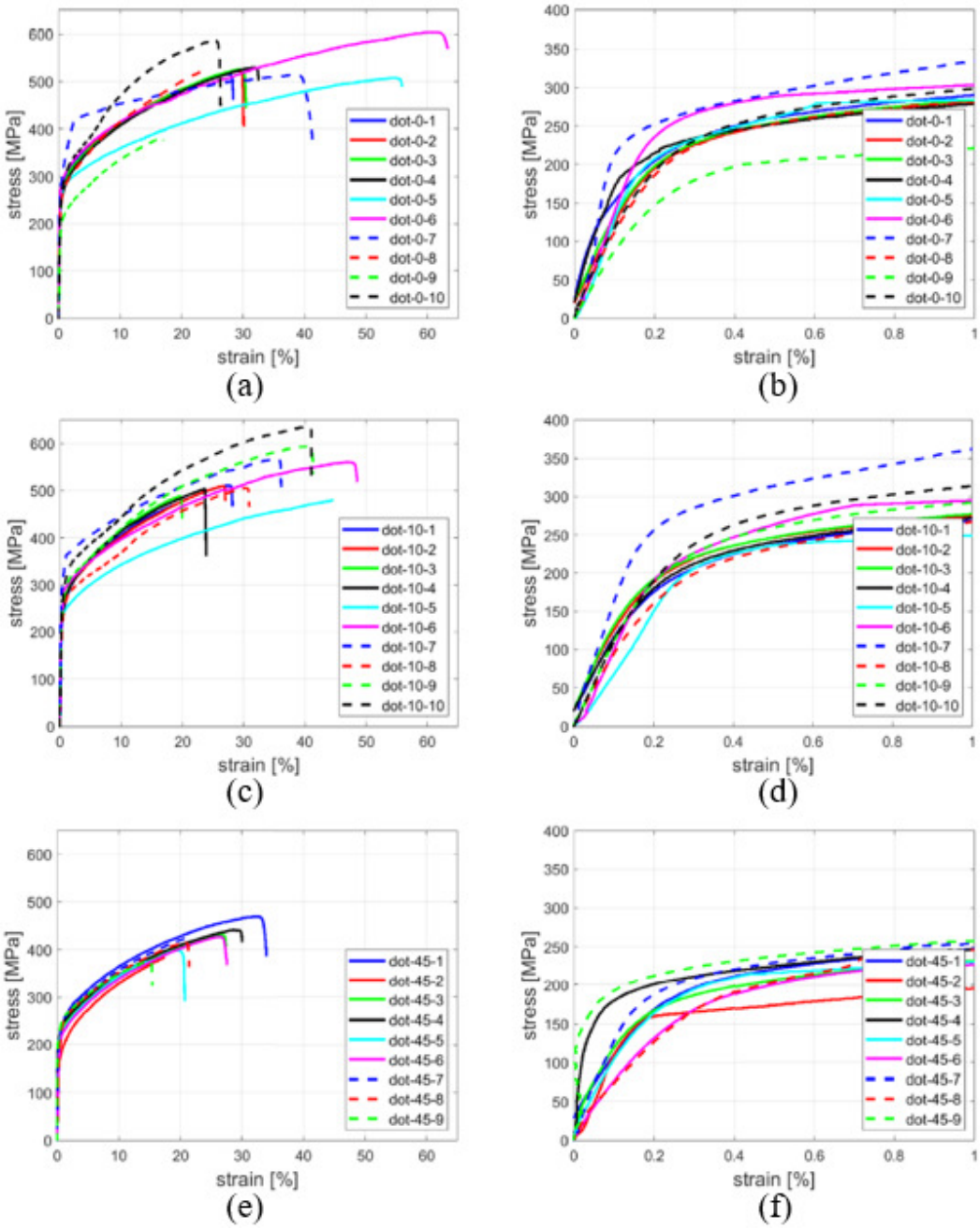

Figure 6.1 Effective stress–strain curves for tensile tests on WAAM bars: full curve and a zoom of them (up to 1% strain) for specimens with (a,b) dot-0, (c,d) dot-10 and (e,f) dot-45 (V. P. Laghi 2022).

Observing the stress-strain curves, there is a significant variability in the tensile response within each orientation. Dot-0 and dot-10 specimens presented ultimate tensile strength up to 600 MPa and elongation to failure up to 40%, both mechanical parameters were lower for dot-45. All three orientations registered very large post-yielding hardening behavior until rupture.

Young's modulus (E), 0.2% proof stress ($R_{p,02}$), ultimate tensile strength (UTS), elongation to failure ($A_{\%}$), yield-to-tensile strength ratio ($R_{p,02}$/UTS) and element's ductility were evaluated from the effective stress-strain curves. These main mechanical parameters are reported in Table 6.4.

Specimen	**E** [GPa]	**$R_{p,02}$** [MPa]	**UTS** [MPa]	**$A_{\%}$** [%]	**$R_{p,02}$/UTS** [-]	**μ_e** [-]
dot-0	133 ± 27	243 ± 20	524 ± 56	35 ± 14	0.47 ± 0.03	93 ± 42
dot-10	108 ± 19	245 ± 21	536 ± 49	34 ± 9	0.46 ± 0.03	79 ± 21
dot-45	98 ± 28	208 ± 20	419 ± 29	24 ± 6	0.50 ± 0.05	55 ± 14

Table 6.4 Key effective mechanical parameters from tensile tests on WAAM single bars (V. P. Laghi 2021a), (V. P. Laghi 2022).

The average value of all the key effective mechanical parameters decrease with increasing build angle.

The experimental results show discrepancies with respect to the traditionally manufactured steel, especially the Young's modulus, for which the specimens present low values with a large scatter. Instead of, 0.2% proof stress and ultimate tensile strength values are comparable to the standard values for conventional 304L steel. However, the reduction is in line with the results obtained on specimens extracted from WAAM steel plates printed with "continuous" strategy (V. P. Laghi 2021b), (V. P. Laghi 2020c), (Kyvelou 2020). The low values of the strength ratio evidences a significant hardening behavior of the WAAM single bars, possibly related to the microstructure resulting from the "dot-by-dot" strategy.

The Table 6.5 reports the values of the coefficient of variation (COV) registered for the key effective mechanical parameters considering the three different build angles. High values for Young's modulus are in line with those exhibited by the as-built specimens cut from plates printed with the same wire (V. P. Laghi 2021b). 0.2% proof stress and ultimate tensile strength variabilities are very close to the overall cross-sectional area variability, as expected. Elongation at rupture and element's ductility exhibit very large COV values, which are influenced by all the geometrical variabilities.

Effective mechanical parameter variability					
Specimen	**E**	**$R_{p,02}$**	**UTS**	**$A_{\%}$**	**μ_e**
dot-0	22%	11%	12%	39%	45%
dot-10	18%	9%	9%	33%	27%
dot-45	28%	8%	7%	26%	26%

Table 6.5 Variability of the key effective mechanical parameters (COV) (V. P. Laghi 2022).

The specimens printed with different build angles are compared: the specimens printed at low build angles (dot-0 and dot-10) revealed good strength properties in terms of 0.2% proof stress and ultimate tensile strength, in line with conventional 304L stainless steel. Values of Young's modulus, elongation at rupture and element's ductility revealed the highest influence of the build angle.

6.2.2. Compression tests

The compression tests were performed on 14 dot-0 specimens, with different lengths, corresponding to slenderness ratios λ from 0.30 to 1.70

The compression tests were carried out on the same universal testing machine as for the tensile tests. The specimens were tested in displacement-control with an initial velocity of 0.2 mm/min, with an unloading after 6 mm displacement at 0.4 mm/min, and re-loading at 0.2 mm/min until 12 mm displacement. The bars were constrained in order to obtain a hinge-clamped configuration. The purpose of the tests is to evaluate the buckling strength at different slenderness values.

The values of the plastic capacity N_{pl} and the critical Eulerian buckling load N_{cr} were evaluated as:

$$N_{pl} = A_{eff} f_y \tag{12}$$

$$N_{cr} = \frac{\pi^2 EJ}{L_{eff}^2} \tag{13}$$

The plastic capacity N_{pl} were evaluated considering the effective cross-sectional area A_{eff} taken from volume-based measurements, as for the tensile tests. The average 0.2% proof stress value from the tensile tests was considered as f_y. The Table 6.6 exhibits the main results from the compression tests for the four main groups of specimens.

Slenderness	λ_m [mm]	$N_{u,m}$ [kN]	$N_{cr,m}$ [kN]	$N_{pl,m}$ [kN]	N_u/N_{cr} [kN]	N_u/N_{pl} [kN]
Very stub	0.28	8.83	83.99	6.83	0.11	1.29
Stub	0.87	4.57	8.66	6.49	0.53	0.70
Slender	1.38	2.79	3.07	5.82	0.91	0.48
Very slender	1.67	1.50	2.53	7.01	0.59	0.21

Table 6.6 Results from compression tests on WAAM-produced stainless steel rods (V. P. Laghi 2021a).

The specimens with lowest slenderness ratio (stub rods) registered the highest ultimate force values, even higher than their corresponding mean plastic force. This result can be related to the significant post-yielding hardening before failure, as resulted from the tensile tests.

6.2.3. Three-point bending test

The three-point bending tests were performed on 10 dot-0 specimens of 200 mm length then tested under compression.

The aim of the tests is to measure the elastic flexural stiffness of the bars within the elastic limit of the material, hence before reaching yielding (corresponding to around 200 MPa of stress). The results confirmed an effective flexural elastic modulus of around 110 GPa for bars printed with 0° build angle, thus having 85% reduction from the elastic modulus value registered from tensile tests (V. P. Laghi 2022 (under review)).

6.2.4. Buckling behavior

The research is going forward to extend the presented results in terms of additional experimental tests conducted on rods with different end constraints, and development of numerical studies in order to explore the influence of the main parameters on the buckling behavior and calibrate ad-hoc buckling curves for WAAM-produced rods. Both parametric and numerical investigations will be performed and compared with the experimental results to draw first design guidelines for WAAM-produced stainless steel structures subjected to compression (V. P. Laghi 2021a).

6.3. Tensile test on crossed-bars

The research presented in the previous Section 6.2 is going on performing tensile tests on WAAM steel crossed-bars. They are characterized through tensile tests, both uni-axial loading (along the longitudinal axis of one of the two bars) and multi-axial loading (on both the two bars at the same time). The object is to study how the intersection influences the overall behavior of the specimen, then exploring how this is influenced by a different inclination of the bar.

The mechanical characterization is performed on WAAM stainless steel specimens made by two rod-like straight elements which has an intersection point. This portion of the work is focused on the investigation of these as-built elements, whose mechanical response is affected by both bars and intersection behaviors, moreover, the two bars of the specimens were produced with two different orientations. Accordingly, the work is organized to perform the mechanical characterization taking into account also the influence of the relative direction of the bar with respect to the printing layers deposited.

The crossed-bars consist of two bars: one presents the longitudinal axis aligned along the vertical direction, coincident with the printing direction, and the other one with the longitudinal axis inclined by a certain angle, respectively 10°, 20° and 30° (referred to by name X10, X20, X30) with respect to the vertical direction (Figure 6.2). They were produced by MX3D (MX3D), as for the previous WAAM-produced steel bars, with the same printing process parameters (Table 6.1).

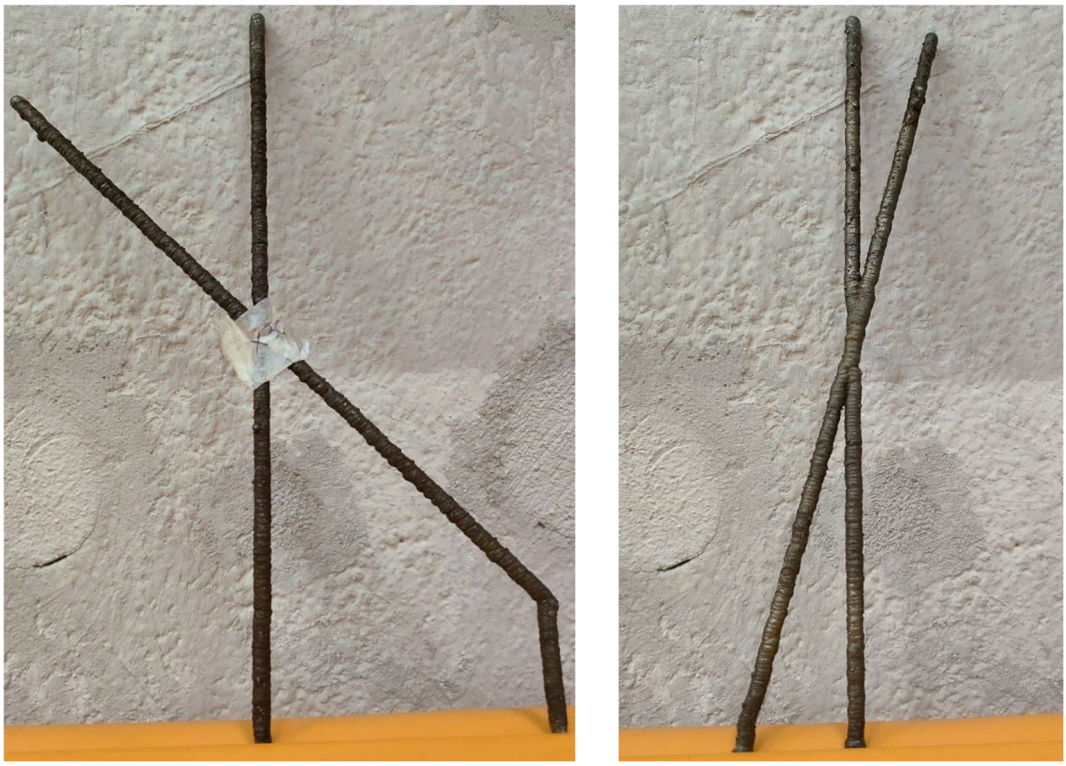

Figure 6.2 Examples of "X bars": on the left, X30 and on the right, X10.

The geometrical characterization was performed on all the 43 crossed-bars specimens produced by MX3D and reported in the following pages, instead of the tensile tests have been performed on a group of them, because this mechanical characterization is part of a wide experimental campaign, as presented in the section 6.2. Tensile tests were carried out over a total of 26 specimens. Between them, 8 were of X10, 7 of X20 and 11 of X30 series of specimens.

6.3.1. Geometrical characterization

A benchmark of crossed-bars related to the same type of inclination is characterized by means of a measuring system in order to understand the variability of the geometrical characterization due to the inherent property of the WAAM process. Notice that the specimens belonging to the same category, based on the inclination of the inclined bar, were printed with the same printing process parameters, therefore they have the same model.

As exposed in the Section 6.2, the possible measuring systems to be adopted performing the geometrical characterization are three. Among these, the ones used in this section to assess the geometrical parameters of WAAM crossed-bars are two: digital caliper and volume-based measurements.

6.3.1.1. X10

The effective cross-sectional area, A_{eff}, is derived using an average value as obtained from volumetric measurements on as-built specimens. On this regard, the Table 6.7 presents the volume-based measures of the effective diameter. Additionally, the average, standard deviation and covariance values are reported for each inclination, in order to assess the variability of the entire batch.

The effective diameter is assumed to be constant along the whole crossed bar (e.g. it is 5.67 mm for X10_1 specimen), enabling to interpret the mechanical tensile tests.

Specimen	Dry Weight	Hydrostatic specific Weight	Volume	A_{av}	d_{av}
-	[g]	[g]	[m^3]	[mm^3]	[mm]
X10_1	105.32	91.93	0.013	25.22	5.67
X10_2	106.37	92.83	0.014	25.29	5.67
X10_3	104.29	91.00	0.013	25.13	5.66
X10_4	103.40	90.18	0.013	25.04	5.65
X10_5	105.54	92.08	0.013	25.23	5.67
X10_6	105.65	92.19	0.013	25.14	5.66
X10_7	104.49	91.17	0.013	25.09	5.65
X10_8	105.35	91.92	0.013	25.01	5.64
X10_9	105.02	91.65	0.013	25.11	5.65
X10_10	106.43	92.84	0.014	25.45	5.69
X10_11	105.71	92.24	0.013	25.18	5.66
X10_12	106.36	92.81	0.014	25.26	5.67
X10_13	104.16	90.88	0.013	24.94	5.64
X10_14	104.67	91.31	0.013	25.08	5.65
X10_15	105.86	92.32	0.014	25.40	5.69
Average	105.24	91.82	0.013	25.17	5.66
Stand. Dev.	0.86	0.76	0.0001	0.14	0.02
COV [%]	0.82	0.83	0.79	0.54	0.27

Table 6.7 Volume-based measures of the diameter of X10.

A further comparison of the diameter measurements obtained from different monitoring systems is performed, in particular between measures taken with caliper and the ones by means of volume measurements (Table 6.8).

The relative error of the effective diameter (value computed from the volume measurements) with respect to the caliper measurements is computed as follow:

$$\frac{\left(d_{av,v} - \mu_{dav,c}\right)}{d_{av,v}} \tag{14}$$

	Volume	Caliper	Volume
Specimen	$\mathbf{d_{av,v}}$	$\mathbf{d_{av,c}}$	**Error**
-	[mm]	[mm]	[%]
X10_1	5.67	5.63	0.96
X10_2	5.67	5.75	0.82
X10_3	5.66	5.68	1.14
X10_4	5.65	5.64	1.32
X10_5	5.67	5.70	0.93
X10_6	5.66	5.67	1.12
X10_7	5.65	5.67	1.22
X10_8	5.64	5.72	1.37
X10_9	5.65	5.60	1.17
X10_10	5.69	5.82	0.49
X10_11	5.66	5.71	1.03
X10_12	5.67	5.93	0.88
X10_13	5.64	5.74	1.52
X10_14	5.65	5.82	1.24
X10_15	5.69	5.72	0.59
Average	5.66	5.72	
Stand. Dev.	0.02	0.08	
COV [%]	0.27	1.46	

Table 6.8 Caliper and volume-based measures of the diameter of X10.

To have a clear overview, a relative frequency histogram is reported (Figure 6.3).

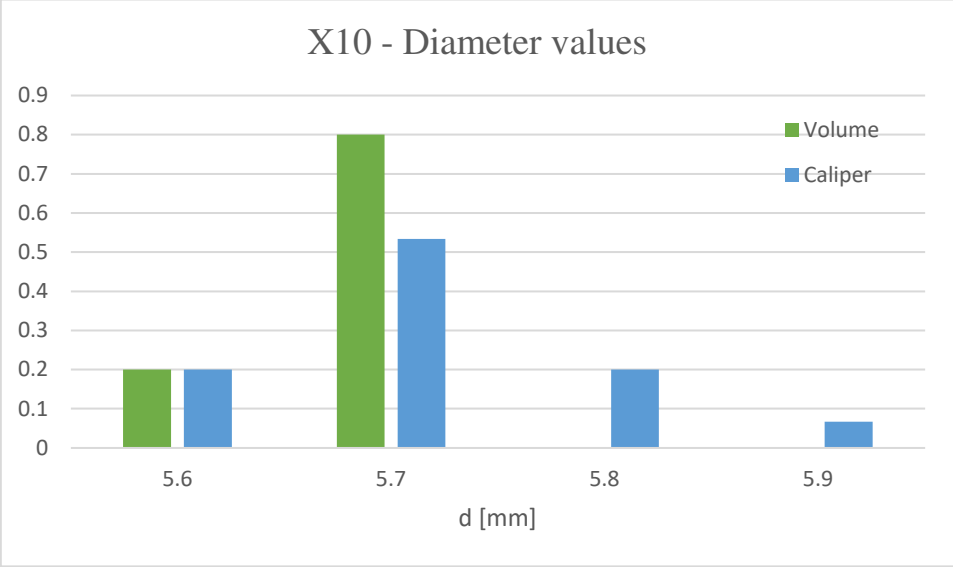

Figure 6.3 Relative frequency histogram of X10 with both volume-based and caliper measures (approximated to the first decimal digit).

6.3.1.2. X20

As presented in the Section 6.3.1.1, the Table 6.9 presents the volume-based measures of the effective diameter. Additionally, the average, standard deviation and covariance values are reported.

Specimen	**Dry Weight**	**Hydrostatic specific Weight**	**Volume**	**A_{av}**	**d_{av}**
-	**[g]**	**[g]**	**[m^3]**	**[mm^3]**	**[mm]**
X20_1	107.54	93.81	0.014	25.24	5.67
X20_2	106.94	93.28	0.014	25.25	5.67
X20_3	108.92	95.04	0.014	25.33	5.68
X20_4	104.45	91.12	0.013	25.01	5.64
X20_5	108.68	94.82	0.014	25.18	5.66
X20_6	109.61	95.64	0.014	25.54	5.70
X20_7	108.99	95.07	0.014	25.13	5.66
X20_8	107.05	93.37	0.014	25.20	5.66
X20_9	105.99	92.44	0.014	25.19	5.66
X20_10	106.09	92.55	0.014	25.03	5.65
X20_11	109.51	95.54	0.014	25.78	5.73
X20_12	109.55	95.56	0.014	25.56	5.70
X20_13	105.52	92.05	0.013	25.18	5.66
X20_14	108.65	94.84	0.013	24.39	5.57
X20_15	109.8	95.69	0.014	25.94	5.75
Average	107.82	94.05	0.014	25.26	5.67
Stand. Dev.	1.66	1.45	0.0002	0.35	0.04
COV [%]	1.54	1.54	1.70	1.37	0.69

Table 6.9 Volume-based measures of the diameter of X20.

A further comparison of the diameter measurements obtained from different monitoring systems is performed, in particular between measures taken with caliper and the ones by means of volume measurements (Table 6.10).

The relative error of the effective diameter with respect to the caliper measurements is computed following the equation (14).

	Volume	**Caliper**	**Volume**
Specimen	$\mathbf{d_{av,v}}$	$\mathbf{d_{av,c}}$	**Error**
-	**[mm]**	**[mm]**	[%]
X20_1	5.67	5.70	1.83
X20_2	5.67	5.74	1.81
X20_3	5.68	5.76	1.65
X20_4	5.64	5.70	2.30
X20_5	5.66	5.81	1.96
X20_6	5.70	5.83	1.23
X20_7	5.66	5.70	2.06
X20_8	5.66	5.65	1.93
X20_9	5.66	5.69	1.94
X20_10	5.65	5.77	2.26
X20_11	5.73	5.93	0.77
X20_12	5.70	5.91	1.21
X20_13	5.66	5.80	1.96
X20_14	5.57	5.84	3.59
X20_15	5.75	5.77	0.46
Average	5.67	5.77	
Stand. Dev.	0.04	0.08	
COV [%]	0.69	1.37	

Table 6.10 Caliper and volume-based measures of the diameter of X20.

Based on the derived information, a relative frequency histogram is reported (Figure 6.4).

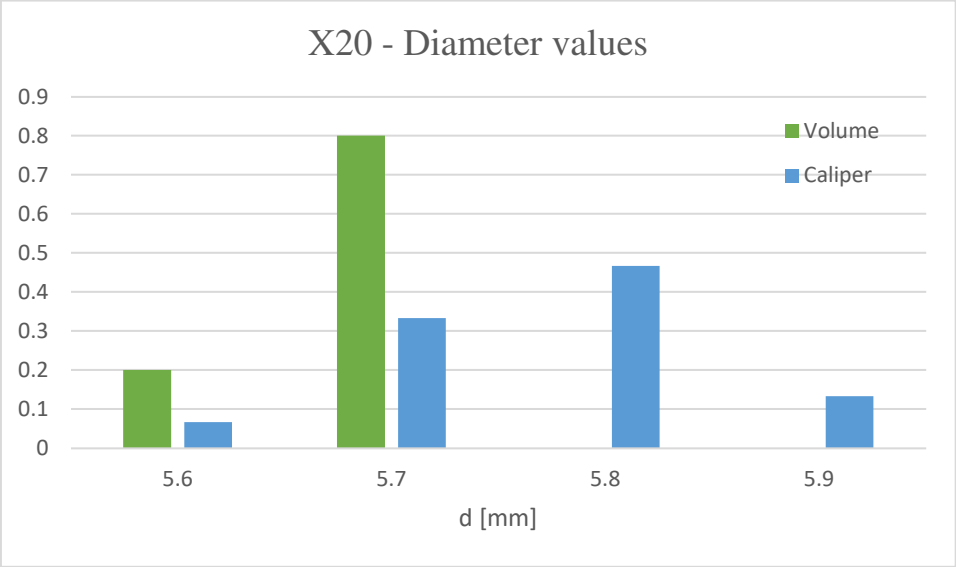

Figure 6.4 Relative frequency histogram of X20 with both volume-based and caliper measures (approximated to the first decimal digit).

6.3.1.3. X30

As presented in the Section 6.3.1.1, the Table 6.11 presents the volume-based measures of the effective diameter. Additionally, the average, standard deviation and covariance values are reported.

Specimen	**Dry Weight**	**Hydrostatic specific Weight**	**Volume**	**A_{av}**	**d_{av}**
-	**[g]**	**[g]**	**[m^3]**	**[mm^3]**	**[mm]**
X30_1	114.18	99.61	0.015	25.72	5.72
X30_2	115.97	101.18	0.015	25.84	5.74
X30_3	112.37	98.04	0.014	25.57	5.71
X30_4	113.52	99.04	0.015	25.61	5.71
X30_5	114.96	100.27	0.015	26.12	5.77
X30_6	114.35	99.77	0.015	25.74	5.73
X30_7	109.21	95.27	0.014	24.99	5.64
X30_8	113.95	99.42	0.015	25.47	5.70
X30_9	115.85	101.11	0.015	25.96	5.75
X30_10	114.37	99.8	0.015	25.70	5.72
X30_11	115.49	100.78	0.015	25.86	5.74
X30_12	115.47	100.74	0.015	25.85	5.74
X30_13	112.71	98.29	0.014	25.84	5.65
Average	114.03	99.49	0.015	25.71	5.72
Stand. Dev.	1.76	1.55	0.0002	0.27	0.03
COV [%]	1.55	1.55	1.50	1.03	0.61

Table 6.11 Volume-based measures of the diameter of X30.

A further comparison of the diameter measurements obtained from different monitoring systems is performed, in particular between measures taken with caliper and the ones by means of volume measurements (Table 6.12).

The relative error of the effective diameter with respect to the caliper measurements is computed following the equation (14).

	Volume	**Caliper**	**Volume**
Specimen	**$d_{av,v}$**	**$d_{av,c}$**	**Error**
-	**[mm]**	**[mm]**	[%]
X30_1	5.72	5.90	0.19
X30_2	5.74	5.78	0.04
X30_3	5.71	5.60	0.49
X30_4	5.71	5.74	0.41
X30_5	5.77	5.86	0.58
X30_6	5.73	5.73	0.15
X30_7	5.64	5.60	1.65
X30_8	5.70	5.73	0.68
X30_9	5.75	6.99	0.26
X30_10	5.72	5.65	0.23
X30_11	5.74	5.82	0.07
X30_12	5.74	5.81	0.05
X30_13	5.65	5.65	1.48
Average	5.72	5.83	
Stand. Dev.	0.03	0.34	
COV	0.006	0.059	

Table 6.12 Caliper and volume-based measures of the diameter of X30.

Based on the derived information, a relative frequency histogram is reported (Figure 6.5).

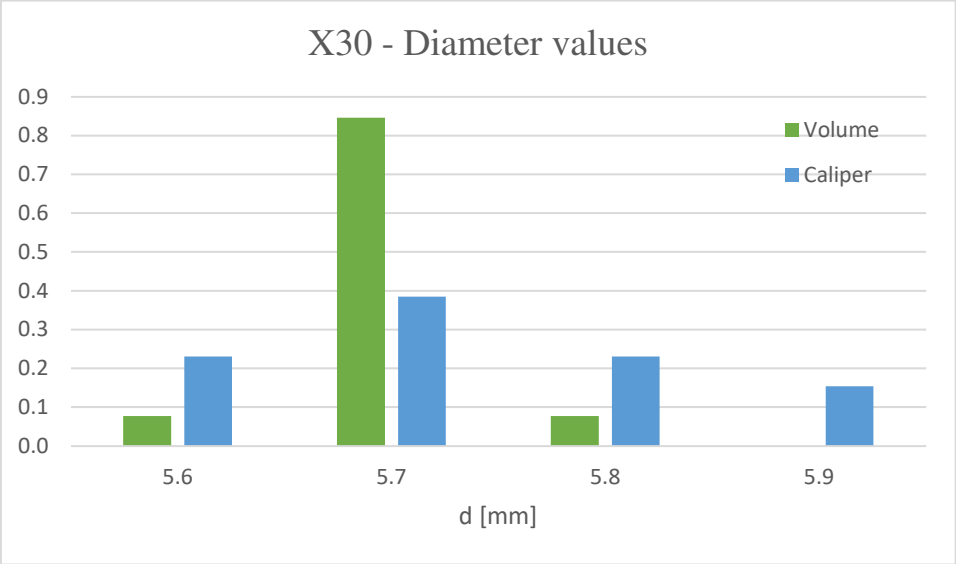

Figure 6.5 Relative frequency histogram of X30 with both volume-based and caliper measures (approximated to the first decimal digit).

Within the specimen-to-specimen characterization, the volume-equivalent cross-section was assumed as the resistant effective cross-sectional area to compute the effective stresses from tensile tests (Kyvelou 2020), (V. P. Laghi 2020b). Then, the average effective diameters d_{eff} are shown in Table 6.13.

Specimen-to-specimen variability	
Specimen	**d_{eff} [mm]**
X-10	5.66 ± 0.02
X-20	5.67 ± 0.04
X-30	5.72 ± 0.03

- *Table 6.13 Mean values and standard deviations of diameters for the tested crossed-bars: specimen-to-specimen variability.*

Between all the batches, the maximum coefficient of variation of the effective diameter related to the volume-based effective diameter is 0.69%, related to the WAAM crossed-bars X20, instead of, it is 0.61% for X30 and 0.27% for X10.

6.3.2. Results

The tensile tests were performed on a universal testing machine of 500 kN load capacity, as for the straight bars with different build angles, presented in the Section 6.2.1. The specimens were tested under displacement-control with a velocity corresponding to a load rate of 2 MPa/s according to (ISO6892-1 2009).

The longitudinal elongation of each specimen was measured using a Linear Variable Differential Transformer (LLVDT). Two monitoring systems were adopted to evaluate the strains, detecting the effective strain of the specimens up to yielding: a linear deformometer of gauge length of 50 mm on the intersection, and another one of gauge length of 25 mm on the bar.

Young's modulus (E), 0.2% proof stress ($R_{p,02}$), ultimate tensile strength (UTS), elongation to failure ($A_{\%}$) were evaluated from the effective stress-strain curves.

Figure 6.6 shows the adopted testing setup.

Figure 6.6 Experimental tensile test setup in case of WAAM crossed-bars specimens.

The crossed-bars were tested on both the bars to detect a different behavior related to the relative inclination of the build direction with respect to the longitudinal axis of the bar. In this regard, for each type of series (e.g. X10, X20 and X30) the test is performed on some specimens along the straight bar A, which has the build direction coincident with the longitudinal axis, and on the others along the inclined bar B, which has a certain inclination of the longitudinal axis of the bar with respect to the build direction (Figure 6.7). The adopted notation indicates the tested specimen plus the letter referred to the bar on which the tensile test was performed (e.g. X10_10A is the specimen number 10 belonging to the specimen type with the bar inclined of 10°, which was tested along the bar A).

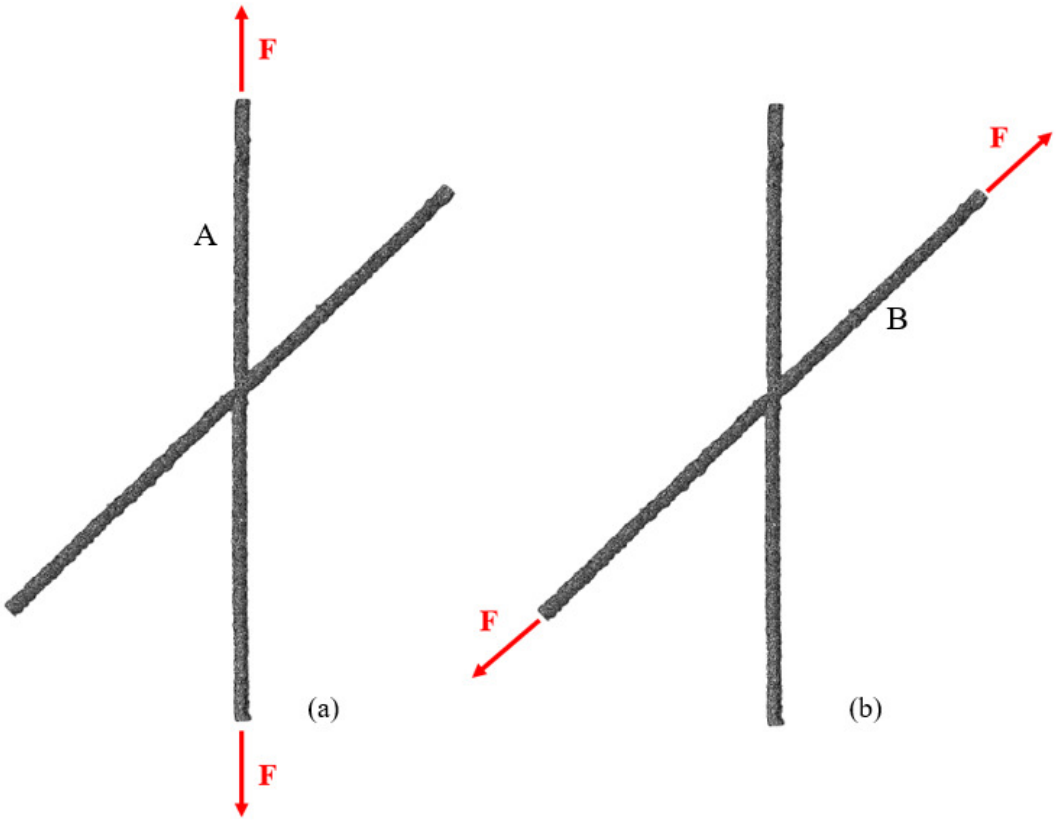

Figure 6.7 Testing methods: (a) tensile test along the bar A, (b) tensile test along the bar B.

The expected possible tensile failures for WAAM crossed-bars specimens are three, based on the portion of the specimen with less strength, hence the failure can occur on the bar, either on the intersection or close to it. This response exhibits how the intersection point may interfere in the overall behavior of the specimen, whether

it represents the weaker point, or the failure occurs on the bar, hence when the intersection point is far from the ultimate tensile strength.

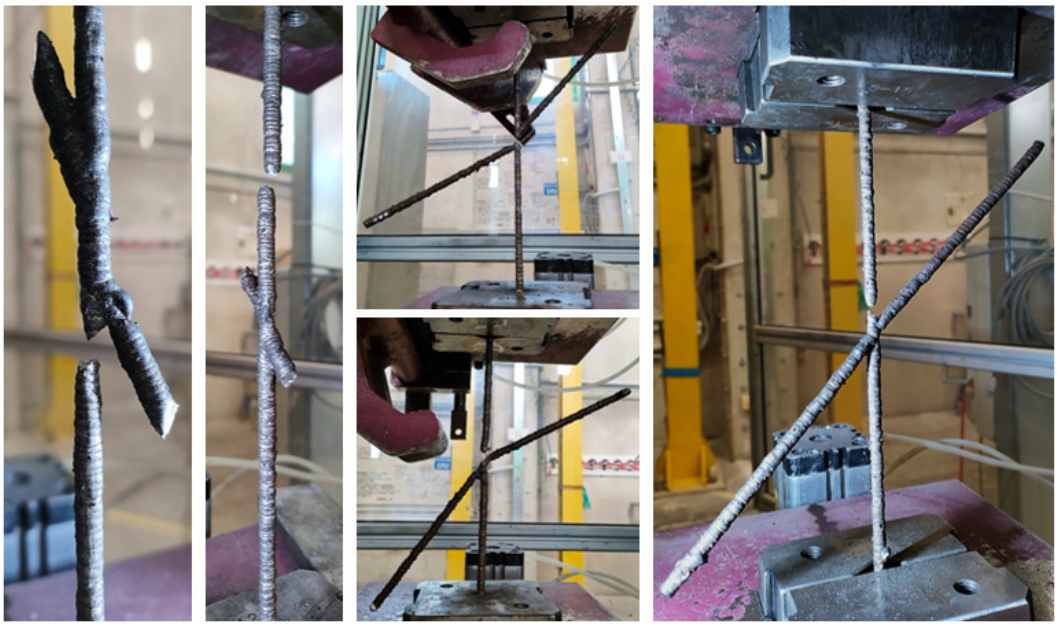

Figure 6.8 Different tensile failure for a WAAM crossed-bars.

Some specimens were tested with the addition of strain gauges to the others monitoring systems, in order to obtain local information about the linear deformation of the specimen up to yielding, ensuring the possibility to compare the information provided by deformometers and strain gauges to assess the anisotropic material behavior (Figure 6.9, 6.10 and 6.11).

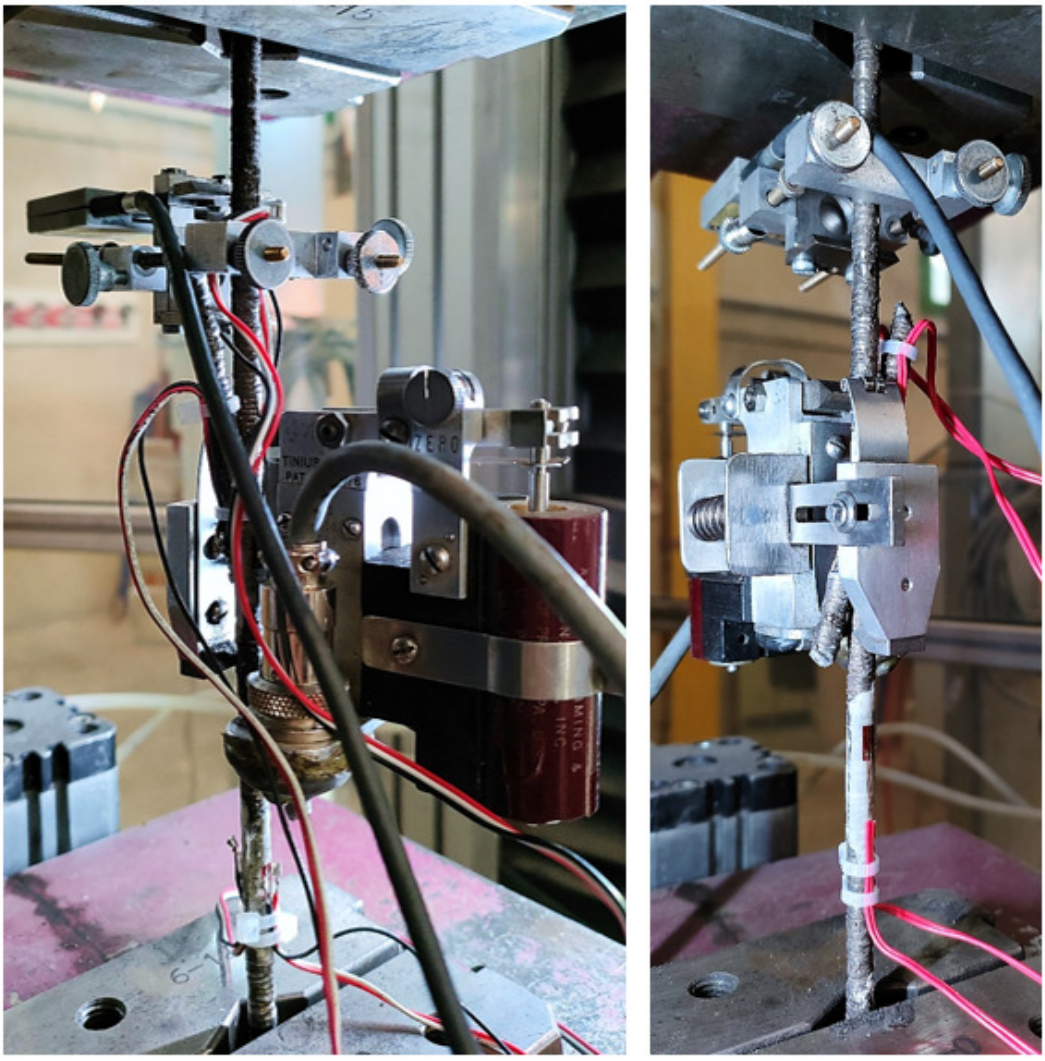

Figure 6.9 Experimental tensile test setup with deformometers and strain gauges: (a) X10_10A, (b) X10_15A.

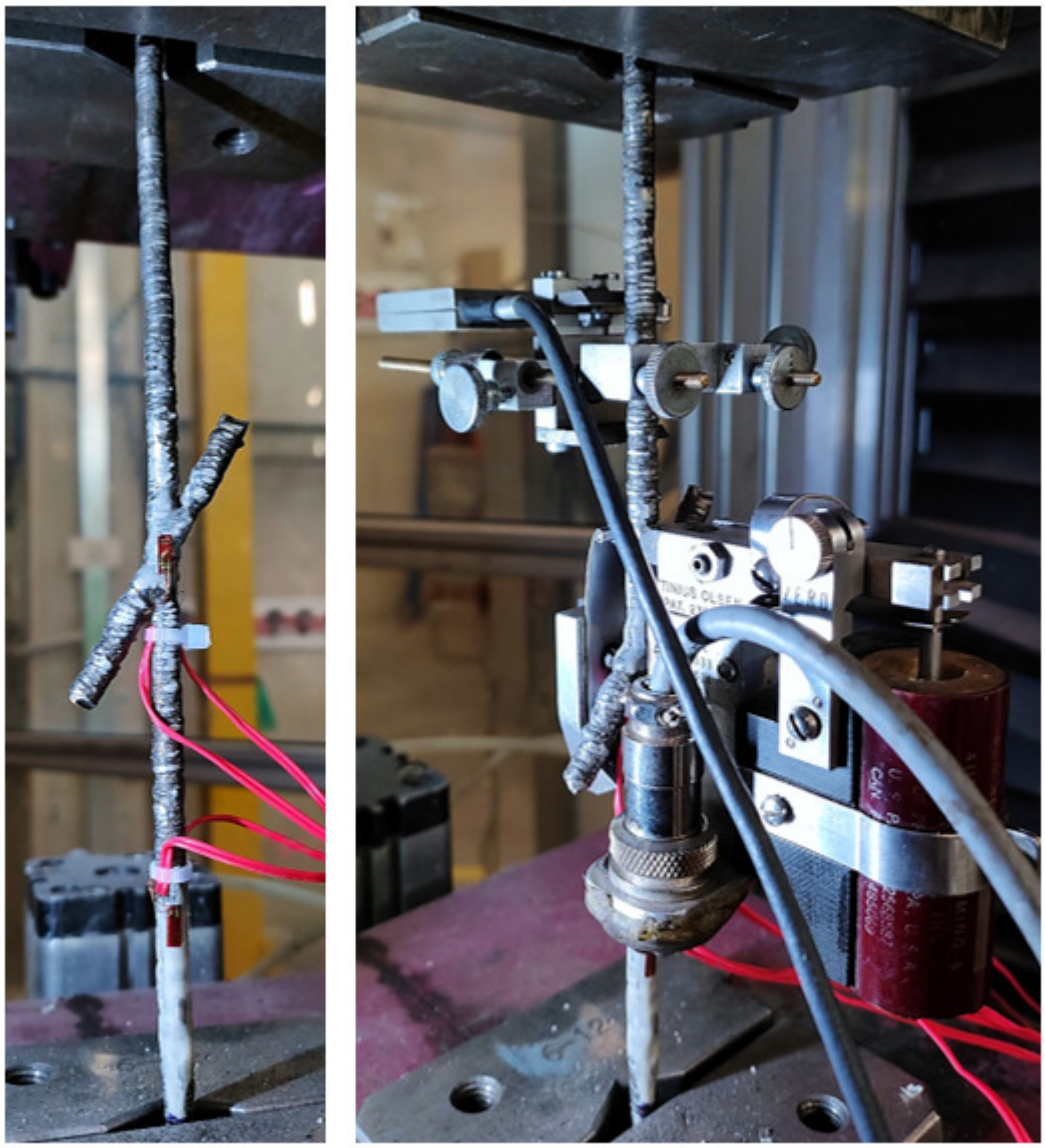

Figure 6.10 Experimental tensile test setup with deformometers and strain gauges: (a) X20_15A with only strain gauges, (b) X20_15A with the complete setup.

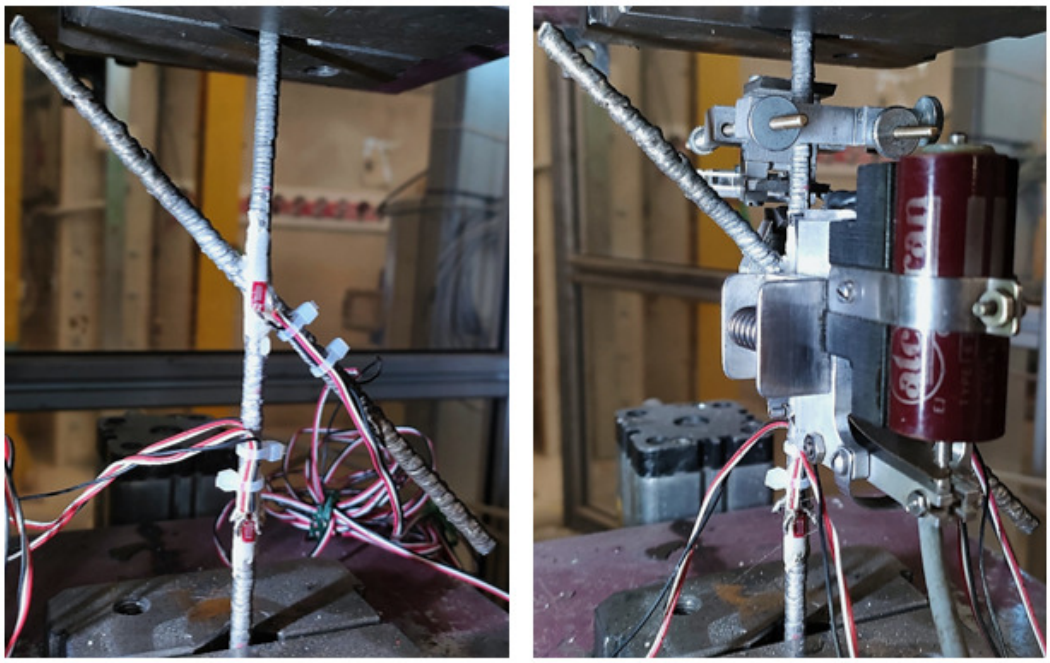

Figure 6.11 Experimental tensile test setup with deformometers and strain gauges: (a) X30_13A with only strain gauges, (b) X30_13A with the complete setup.

The surface roughness is an inherent geometrical irregularity of WAAM-produced elements, due to this, the application of the strain gauges was different from the usual one in order to create a smooth surface on which the strain gauge was able to give us information about the deformation. The process is organized as follow:

- Conditioner to clean the surface (acid) by means of an abrasive paper,
- Acid neutralizer (alkaline),
- Superglue to create a smooth surface,
- Strain gauges are applied with glue.

The "X bars" specimens were not tested all with the same type of strain gauges, in particular, X30_3B, X30_12A and X30_13A specimens were tested with the strain gauge type "Flab-3-11" with a gauge factor of 2.09 ± 1%, instead of, X10_10A, X10_15A and X20_15A specimens were tested with the strain gauge type "KFGS-3-120-C1-11" with a gauge factor of 2.11 ± 1%.

6.3.2.1. X10

The tensile tests were performed obtaining information to be interpreted by means of the effective cross-sectional area. The effective stress values (σ_{eff}) were computed as the ratio between the tensile force acting on the tested bar and its effective cross-sectional area, according to the Equation (10). Effective strain values were computed as the ratio between the elongation and its undeformed initial length, according to the Equation (11), and considering a gauge length of 50 mm and one of 25 mm for the information coming respectively from the intersection and the bar. The information are then organized in an effective stress-strain curve of WAAM crossed-bars, and a zoom of it, for strain values lower than 1%, pointing the attention on the first part of the tensile test, exhibiting the Young's modulus and the 0.2% proof stress values.

The results are reported for both the testing method, referring to the tensile test performed on the bar A (named as "straight bar", the build direction is coincident with the longitudinal axis of the bar) and the one performed on the bar B (named as "inclined bar", the longitudinal axis of the bar is inclined of 10° with respect to the build direction).

In particular, all the stress-strain curves related to the same testing method are reported on the same graph, in order to compare crossed-bars belonging to the same batch, also comparing information provided by the linear deformometer both on the bar and on the node, derived from the same bar with node.

In the Figure 6.12, the reported results refer to the tensile test performed on the straight bar A with the node (the build direction is coincident with the longitudinal axis of the bar), referring to the results collected by means of a linear deformometer of gauge length of 25 mm positioned on the bar and another one of gauge length of 50 mm on the node.

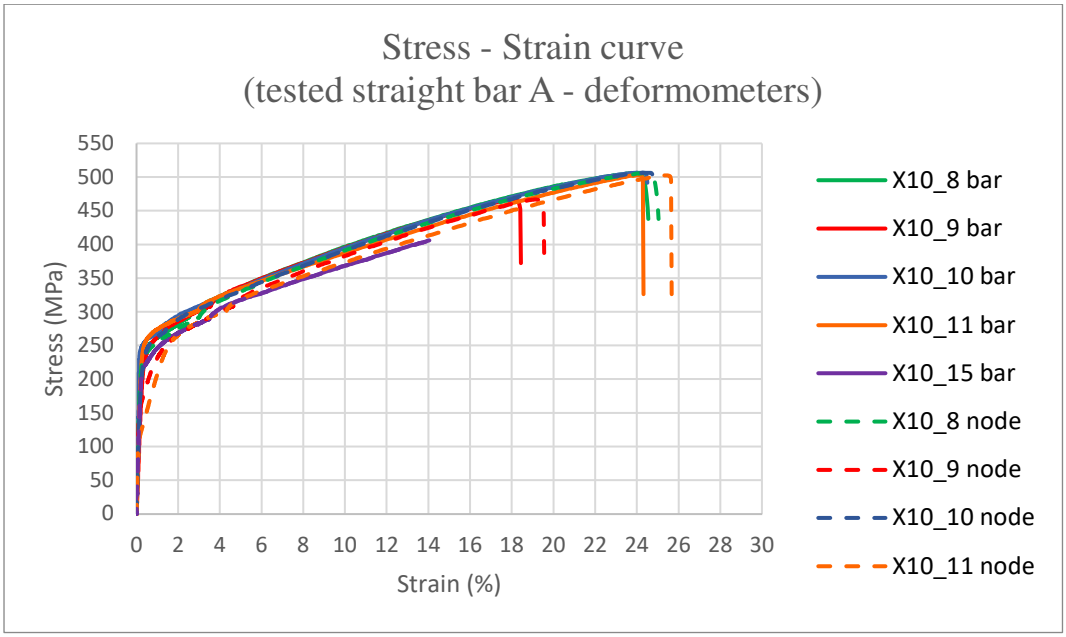

Figure 6.12 Effective stress-strain curves for tensile tests on WAAM crossed-bars (X10) tested along the straight bar A.

To explore the first part of the tensile test, exhibiting the Young's modulus and the 0.2% proof stress values, a zoom of the effective stress-strain curve of WAAM crossed-bars (for strain lower than 1%) is reported in Figure 6.13.

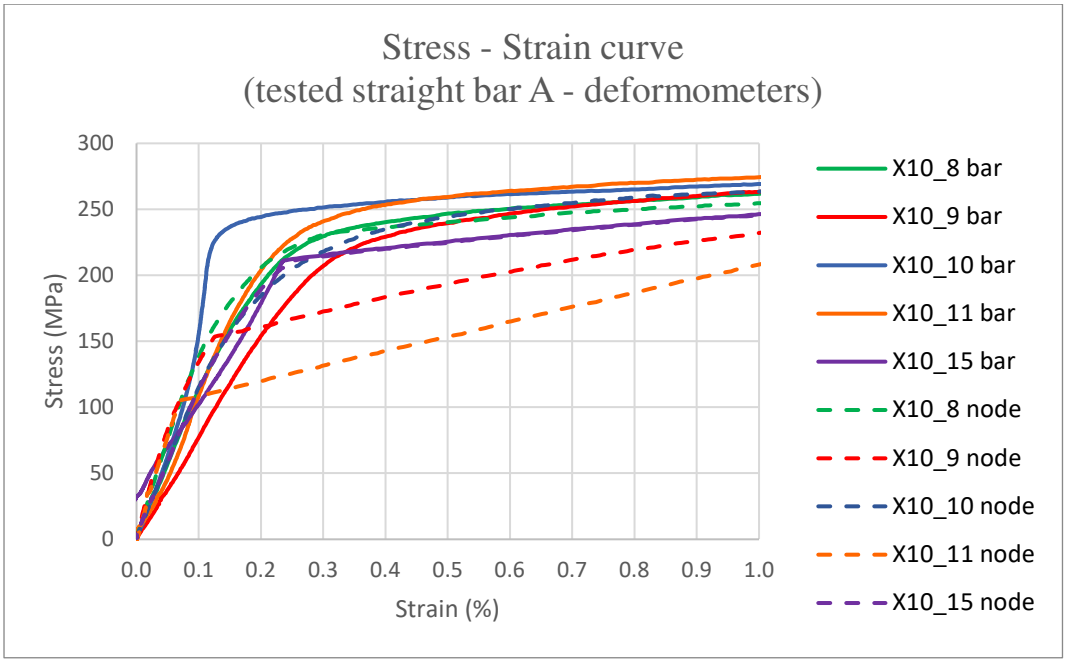

Figure 6.13 A zoom of the effective stress-strain curves (up to 1% strain) for tensile tests on WAAM crossed-bars (X10) tested along the straight bar A.

Young's modulus (E), 0.2% proof stress ($R_{p,02}$), ultimate tensile strength (UTS), elongation to failure ($A_{\%}$) and yield-to-tensile strength ratio ($R_{p,02}$/UTS) were evaluated from the effective stress-strain curves. These main mechanical parameters are reported in Table 6.14. The notation "bar" refers to the effective mechanical parameters provided by the linear deformometer located on the bar, instead of, the notation "node" refers to the effective mechanical parameters provided by the linear deformometer located on the node of the straight bar A.

Straight bar A with node		**E**	**Rp,02**	**UTS**	**A%**	**Rp,02/UTS**
		[GPa]	**[MPa]**	**[MPa]**	**[%]**	**[-]**
X10_8	bar	115.01	242.13	505.96	25.03	0.48
	node	143.68	245.48			0.49
X10_9	bar	85.55	236.67	467.09	19.55	0.51
	node	136.80	174.98			0.37
X10_10	bar	149.10	259.08	506.71	25.83	0.51
	node	115.41	233.60			0.46
X10_11	bar	145.45	257.94	502.81	25.66	0.51
	node	141.33	128.97			0.26
X10_15	bar	87.37	224.00	467.13	21.23	0.48
	node	116.45	213.30			0.46

Table 6.14 Key effective mechanical parameters from tensile tests on WAAM crossed-bars (X10) tested along the straight bar A provided by the two deformometers on both bar and node.

Straight bar A with node (X10)		
E_{av}(bar)	**[GPa]**	116.50
E_{av}(node)	**[GPa]**	130.73
E_{av}(bar)/E_{av}(node)	**[-]**	0.89
UTS_{av}	**[MPa]**	489.94

Table 6.15 Mean values of Young's modulus and ultimate tensile strength from tensile tests on WAAM crossed-bars (X10) tested along the straight bar A.

In the Table 6.15, the ratio between the mean values of the Young's modulus related to the bar and the node provides a value smaller than one, therefore the node exhibits an higher contribution with respect to the straight bar with the node. The coefficient of variation of the Young's modulus is higher in case of the bar with a value of 23.38%, compared to 9.40% of the node. The variation in terms of ultimate tensile strength of the straight bar A with the node is smaller, 3.81%.

In the Figure 6.14, the reported results refer to the tensile test performed on the inclined bar B with the node (the longitudinal axis of the bar is inclined of 10° with respect to the build direction), referring to the results collected by means of a linear deformometer of gauge length of 25 mm positioned on the bar and another one of gauge length of 50mm on the node.

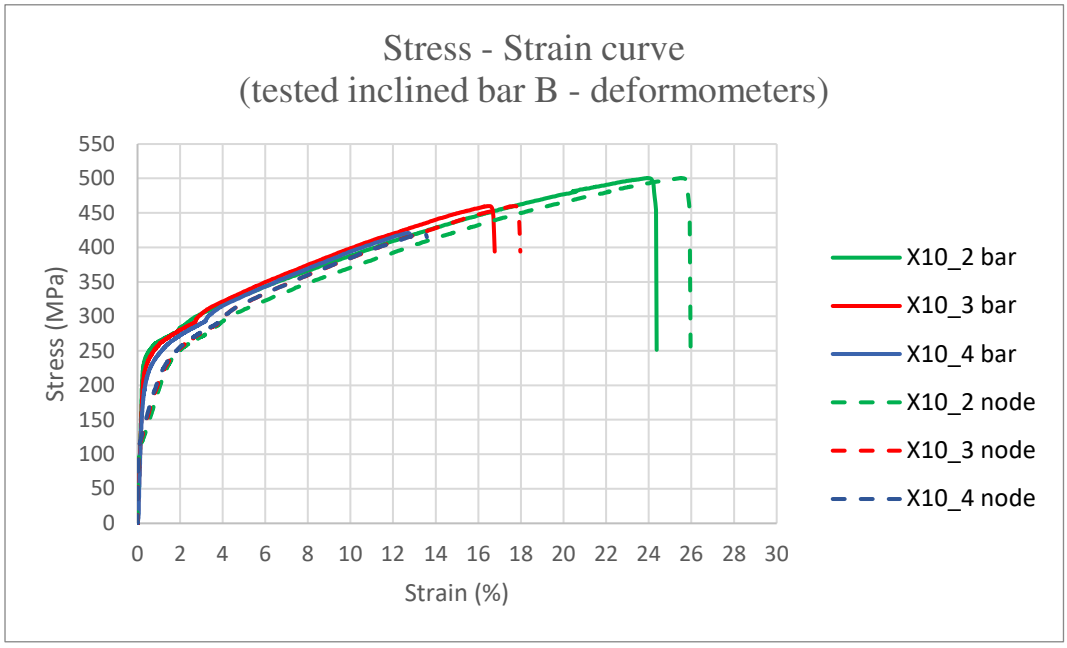

Figure 6.14 Effective stress-strain curves for tensile tests on WAAM crossed-bars (X10) tested along the inclined bar B.

A zoom of the effective stress-strain curve of WAAM crossed-bars (for strain lower than 1%) is reported in Figure 6.15 to explore the first part of the tensile test.

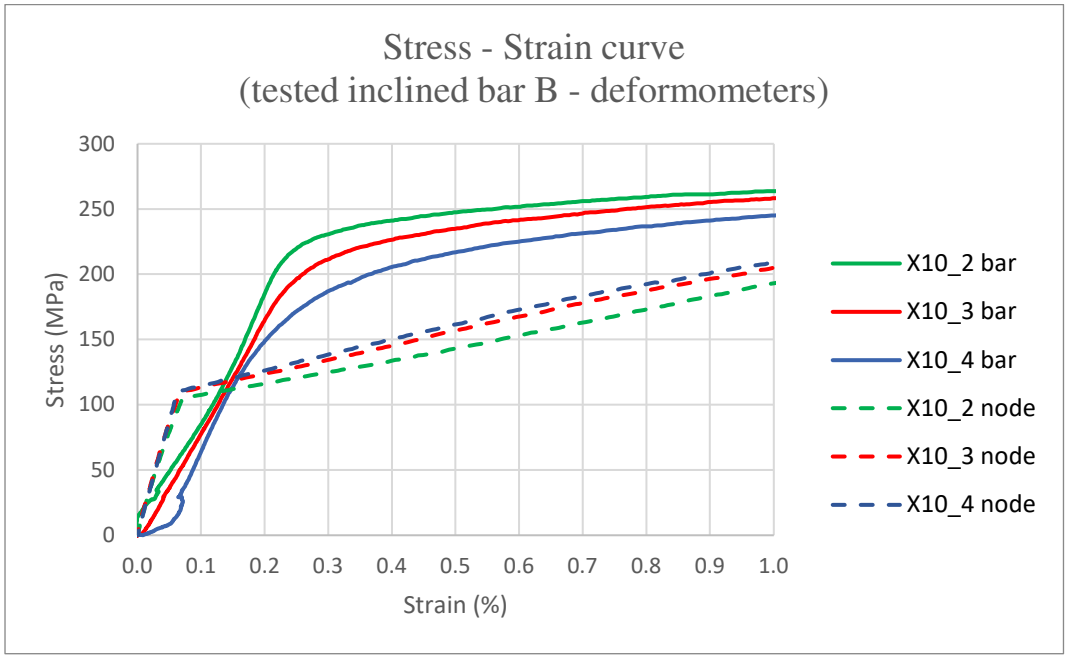

Figure 6.15 A zoom of the effective stress-strain curves (up to 1% strain) for tensile tests on WAAM crossed-bars (X10) tested along the inclined bar B.

Young's modulus (E), 0.2% proof stress ($R_{p,02}$), ultimate tensile strength (UTS), elongation to failure ($A_{\%}$) and yield-to-tensile strength ratio ($R_{p,02}$/UTS) were evaluated from the effective stress-strain curves. These main mechanical parameters are reported in Table 6.16. The notation "bar" refers to the effective mechanical parameters provided by the linear deformometer located on the bar, instead of, the notation "node" refers to the effective mechanical parameters provided by the linear deformometer located on the node of the inclined bar B.

Inclined bar B with node		E	Rp,02	UTS	A%	Rp,02/UTS
		[GPa]	[MPa]	[MPa]	[%]	[-]
X10_2	bar	75.23	249.28	500.59	25.96	0.50
	node	143.73	126.36			0.25
X10_3	bar	82.09	235.77	459.99	17.97	0.51
	node	179.78	137.76			0.30
X10_4	bar	102.85	198.55	421.00	13.87	0.47
	node	174.73	137.76			0.33

Table 6.16 Key effective mechanical parameters from tensile tests on WAAM crossed-bars (X10) tested along the inclined bar B.

Inclined bar B with node (X10)		
E_{av}(bar)	**[GPa]**	86.72
E_{av}(node)	**[GPa]**	166.08
E_{av}(bar)/E_{av}(node)	**[-]**	0.52
UTS_{av} [MPa]	**[MPa]**	460.53

Table 6.17 Mean values of Young's modulus and ultimate tensile strength from tensile tests on WAAM crossed-bars (X10) tested along the inclined bar B.

In the Table 6.17, the ratio between the mean values of the Young's modulus related to the bar and the node provides a value smaller than one, the node exhibits a contribution nearly the double with respect to the inclined bar with the node. The coefficient of variation of the Young's modulus is higher in case of the bar with a value of 13.54%, compared to 9.60% of the node. The variation in terms of ultimate tensile strength of the inclined bar B with the node is 7.06%.

6.3.2.2. X20

The effective stress values (σ_{eff}) were computed according to the Equation (10), while the effective strain values were computed according to the Equation (11), considering a gauge length of 50 mm and one of 25 mm for the information coming respectively from the intersection and the bar. The information are then organized in an effective stress-strain curve of WAAM crossed-bars. In particular, all the stress-strain curves related to the same testing method are reported on the same graph, in order to compare crossed-bars belonging to the same batch, also comparing information provided by the linear deformometer both on the bar and on the node, derived from the same bar with node.

The results are reported for both the testing method, referring to the tensile test performed on the bar A (named as “straight bar”, the build direction is coincident with the longitudinal axis of the bar) and the one performed on the bar B (named as “inclined bar”, the longitudinal axis of the bar is inclined of 20° with respect to the build direction).

In the Figure 6.16, the reported results refer to the tensile test performed on the straight bar A with the node (the build direction is coincident with the longitudinal axis of the bar), referring to the results collected by means of a linear deformometer of gauge length of 25 mm positioned on the bar and another one of gauge length of 50 mm on the node.

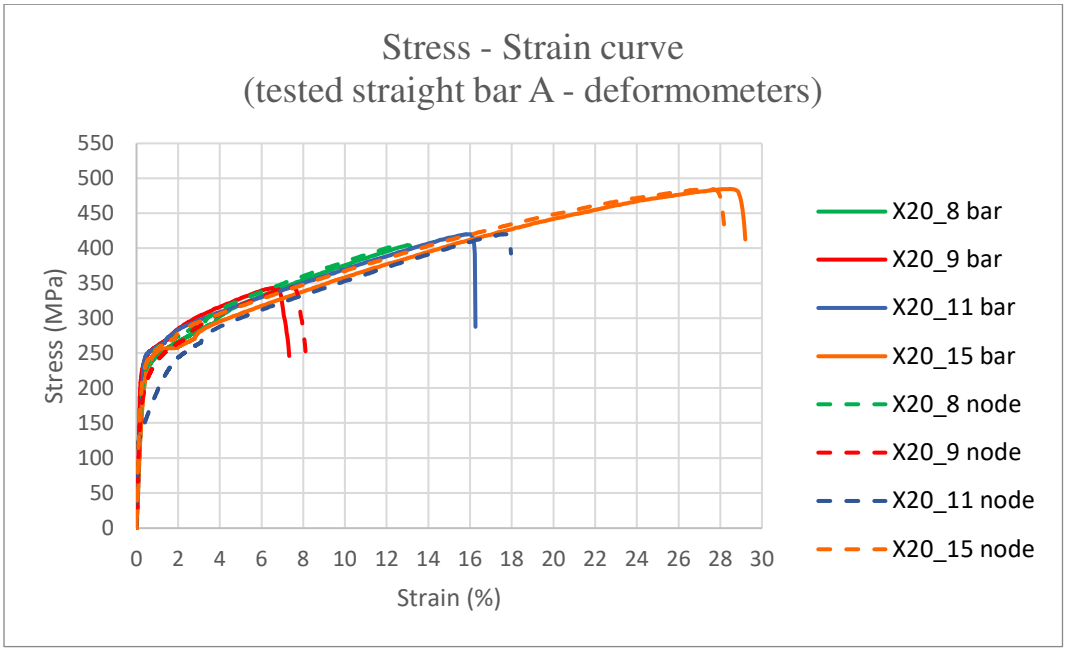

Figure 6.16 Effective stress-strain curves for tensile tests on WAAM crossed-bars (X20) tested along the straight bar A.

To explore the first part of the tensile test, exhibiting the Young's modulus and the 0.2% proof stress values, a zoom of the effective stress-strain curve of WAAM crossed-bars (for strain lower than 1%) is reported in Figure 6.17.

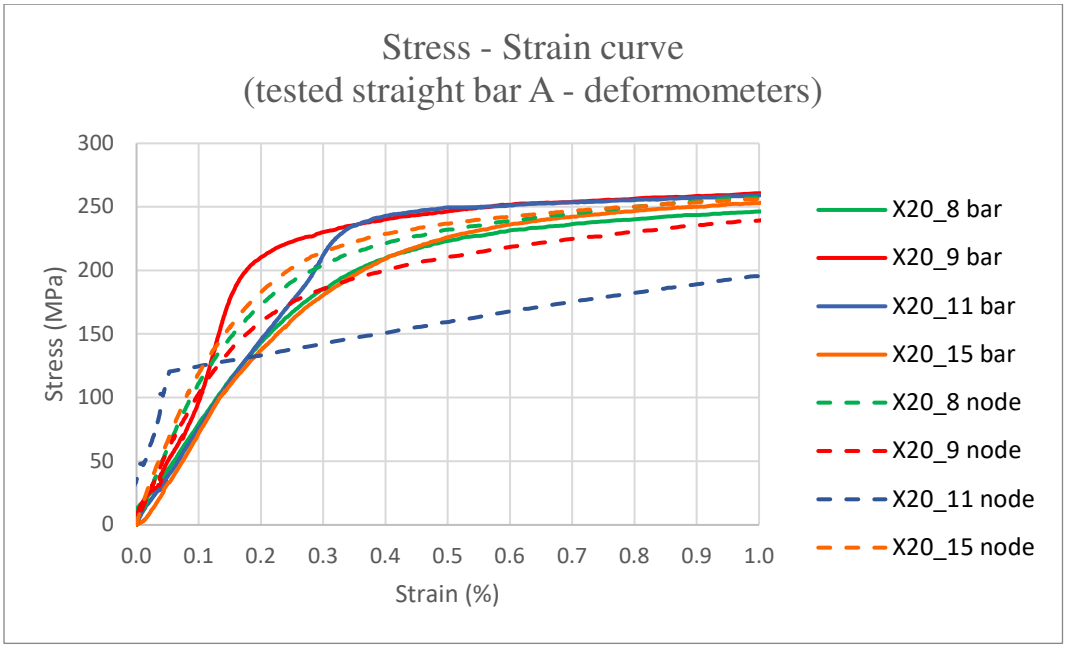

Figure 6.17 A zoom of the effective stress-strain curves (up to 1% strain) for tensile tests on WAAM crossed-bars (X20) tested along the straight bar A.

Young's modulus (E), 0.2% proof stress ($R_{p,02}$), ultimate tensile strength (UTS), elongation to failure ($A_{\%}$) and yield-to-tensile strength ratio ($R_{p,02}$/UTS) were evaluated from the effective stress-strain curves. These main mechanical parameters are reported in Table 6.18. The notation "bar" refers to the effective mechanical parameters provided by the linear deformometer located on the bar, instead of, the notation "node" refers to the effective mechanical parameters provided by the linear deformometer located on the node of the straight bar A.

Straight bar A with node		**E**	**Rp,02**	**UTS**	**A%**	**Rp,02/UTS**
		[GPa]	**[MPa]**	**[MPa]**	**[%]**	**[-]**
X20_8	bar	71.44	224.13	404.76	13.14	0.55
	node	105.92	224.70			0.56
X20_9	bar	82.15	248.40	343.97	8.47	0.72
	node	106.42	198.36			0.58
X20_11	bar	71.13	250.82	420.29	17.98	0.60
	node	158.38	145.20			0.35
X20_15	bar	83.74	219.18	485.15	28.23	0.45
	node	119.12	225.53			0.46

Table 6.18 Key effective mechanical parameters from tensile tests on WAAM crossed-bars (X20) tested along the straight bar A provided by the two deformometers on both bar and node.

Straight bar A with node (X20)		
E_{av}(bar)	**[GPa]**	77.11
E_{av}(node)	**[GPa]**	122.46
E_{av}(bar)/E_{av}(node)	**[-]**	0.63
UTS_{av}	**[MPa]**	413.54

Table 6.19 Mean values of Young's modulus and ultimate tensile strength from tensile tests on WAAM crossed-bars (X20) tested along the straight bar A.

In the Table 6.19, the ratio between the mean values of the Young's modulus related to the bar and the node provides a value smaller than one, therefore the node exhibits an higher contribution with respect to the straight bar with the node. The coefficient of variation of the Young's modulus is smaller in case of the bar with a value of 7.60%, compared to 17.48% of the node. The variation in terms of ultimate tensile strength of the straight bar A with the node is high, 12.15%.

In the Figure 6.18, the reported results refer to the tensile test performed on the inclined bar B with the node (the longitudinal axis of the bar is inclined of 20° with respect to the build direction), referring to the results collected by means of a linear deformometer of gauge length of 25 mm positioned on the bar and another one of gauge length of 50 mm on the node.

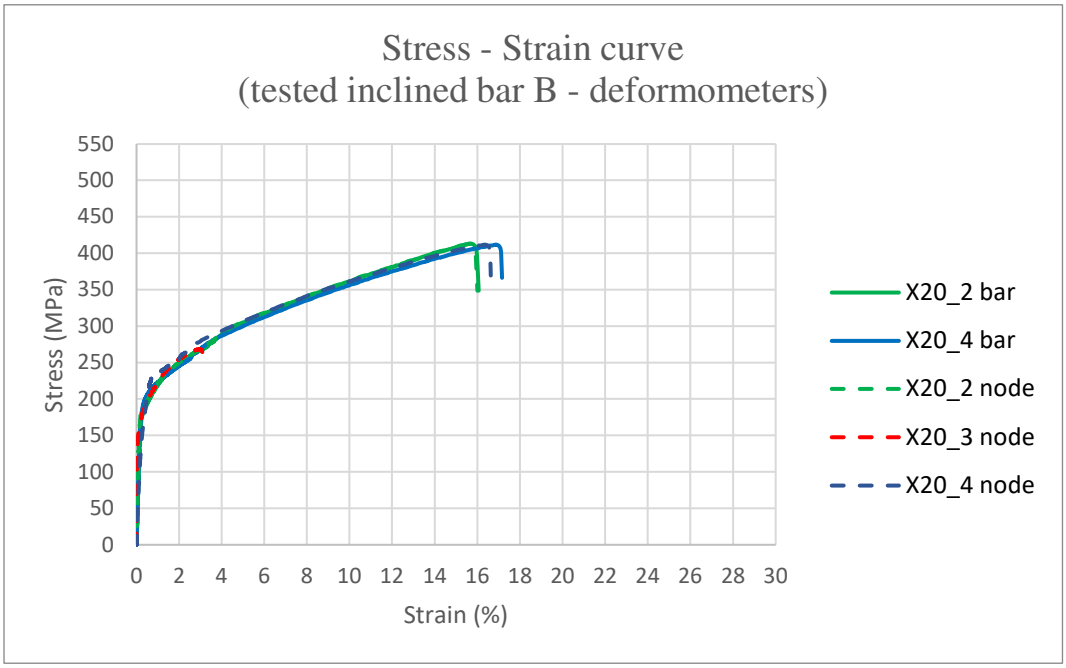

Figure 6.18 Effective stress-strain curves for tensile tests on WAAM crossed-bars (X20) tested along the inclined bar B.

A zoom of the effective stress-strain curve of WAAM crossed-bars (for strain lower than 1%) is reported in Figure 6.19 to explore the first part of the tensile test.

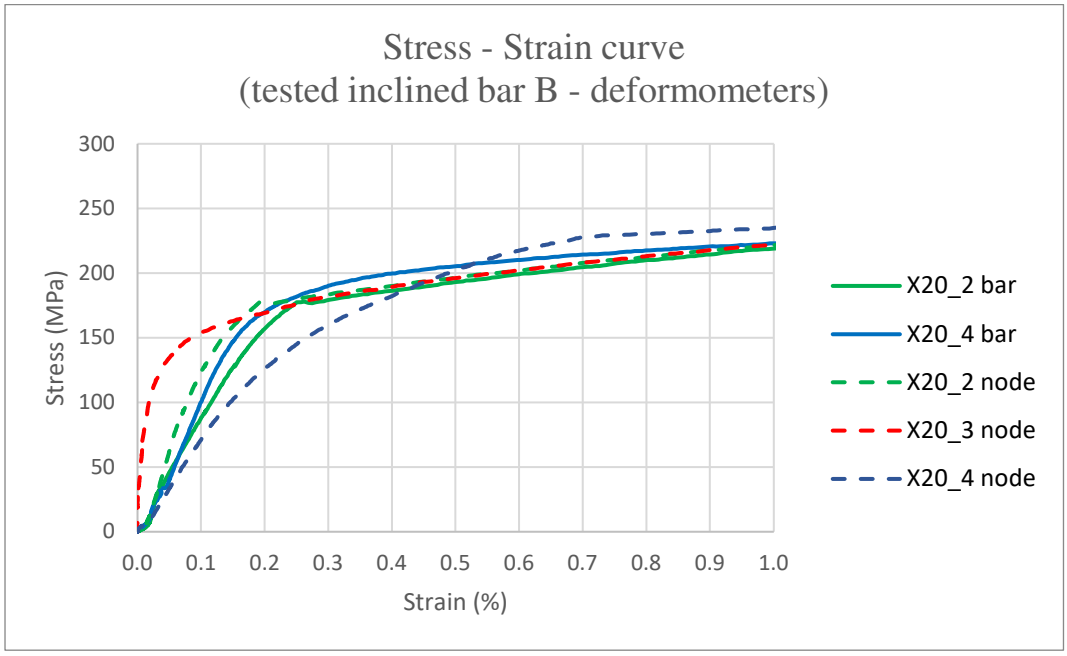

Figure 6.19 A zoom of the effective stress-strain curves (up to 1% strain) for tensile tests on WAAM crossed-bars (X20) tested along the inclined bar B.

Young's modulus (E), 0.2% proof stress ($R_{p,02}$), ultimate tensile strength (UTS), elongation to failure ($A_{\%}$) and yield-to-tensile strength ratio ($R_{p,02}$/UTS) were evaluated from the effective stress-strain curves. These main mechanical parameters are reported in Table 6.20. The notation "bar" refers to the effective mechanical parameters provided by the linear deformometer located on the bar, instead of, the notation "node" refers to the effective mechanical parameters provided by the linear deformometer located on the node of the inclined bar B.

Inclined bar B with node		E	Rp,02	UTS	A%	Rp,02/UTS
		[GPa]	[MPa]	[MPa]	[%]	[-]
X20_2	bar	88.97	177.76	413.08	16.05	0.43
	node	178.42	175.10			0.42
X20_3	node	308.78	185.40	268.39	3.12	0.69
X20_4	bar	114.18	194.82	411.85	17.15	0.47
	node	69.86	199.78			0.49

Table 6.20 Key effective mechanical parameters from tensile tests on WAAM crossed-bars (X20) tested along the inclined bar B.

Inclined bar B with node (X10)		
E_{av}(bar)	**[GPa]**	101.58
E_{av}(node)	**[GPa]**	185.69
E_{av}(bar)/E_{av}(node)	**[-]**	0.55
UTS_{av} [MPa]	**[MPa]**	364.44

Table 6.21 Mean values of Young's modulus and ultimate tensile strength from tensile tests on WAAM crossed-bars (X20) tested along the inclined bar B.

In the Table 6.21, the ratio between the mean values of the Young's modulus related to the bar and the node exhibits a node contribution nearly doubled with respect to the inclined bar with the node. The coefficient of variation of the Young's modulus is very high in the node with a value of 52.60%, compared to 12.41% of the bar. The variation in terms of ultimate tensile strength of the inclined bar B with the node is 18.64%.

6.3.2.3. X30

The effective stress values (σ_{eff}) were computed according to the Equation (10), while the effective strain values were computed according to the Equation (11), considering a gauge length of 50 mm and one of 25 mm for the information coming respectively from the intersection and the bar. The information are then organized in an effective stress-strain curve of WAAM crossed-bars. In particular, all the stress-strain curves related to the same testing method are reported on the same graph, in order to compare crossed-bars belonging to the same batch, also comparing information provided by the linear deformometer both on the bar and on the node, derived from the same bar with node.

The results are reported for both the testing method, referring to the tensile test performed on the bar A (named as “straight bar”, the build direction is coincident with the longitudinal axis of the bar) and the one performed on the bar B (named as “inclined bar”, the longitudinal axis of the bar is inclined of 30° with respect to the build direction).

In the Figure 6.20, the reported results refer to the tensile test performed on the straight bar A with the node (the build direction is coincident with the longitudinal axis of the bar), referring to the results collected by means of a linear deformometer of gauge length of 25 mm positioned on the bar and another one of gauge length of 50 mm on the node.

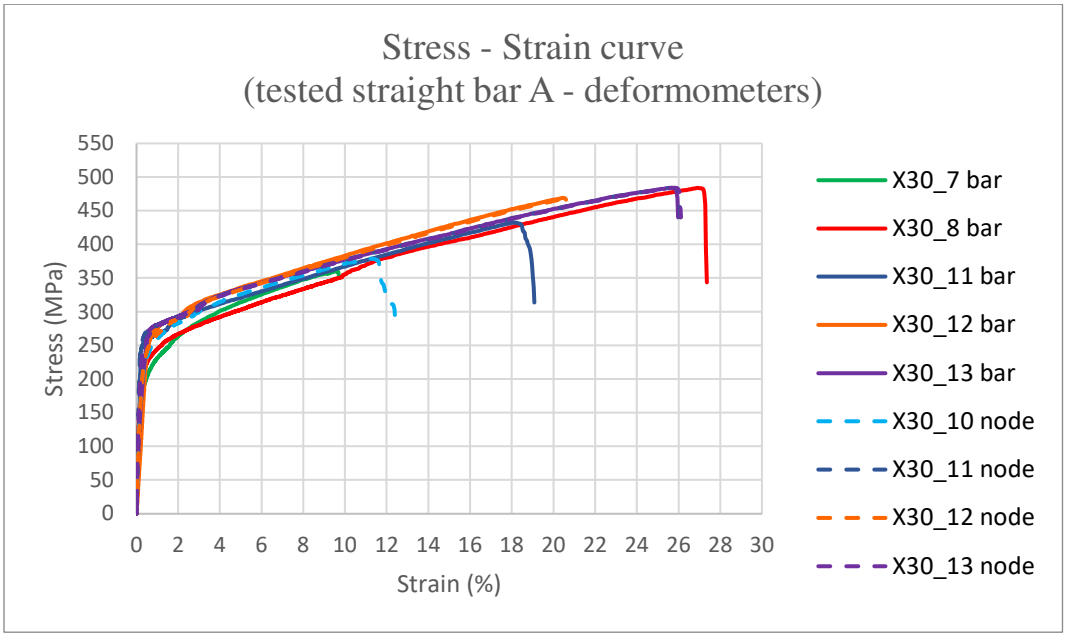

Figure 6.20 Effective stress-strain curves for tensile tests on WAAM crossed-bars (X30) tested along the straight bar A.

To explore the first part of the tensile test, exhibiting the Young's modulus and the 0.2% proof stress values, a zoom of the effective stress-strain curve of WAAM crossed-bars (for strain lower than 1%) is reported in Figure 6.21.

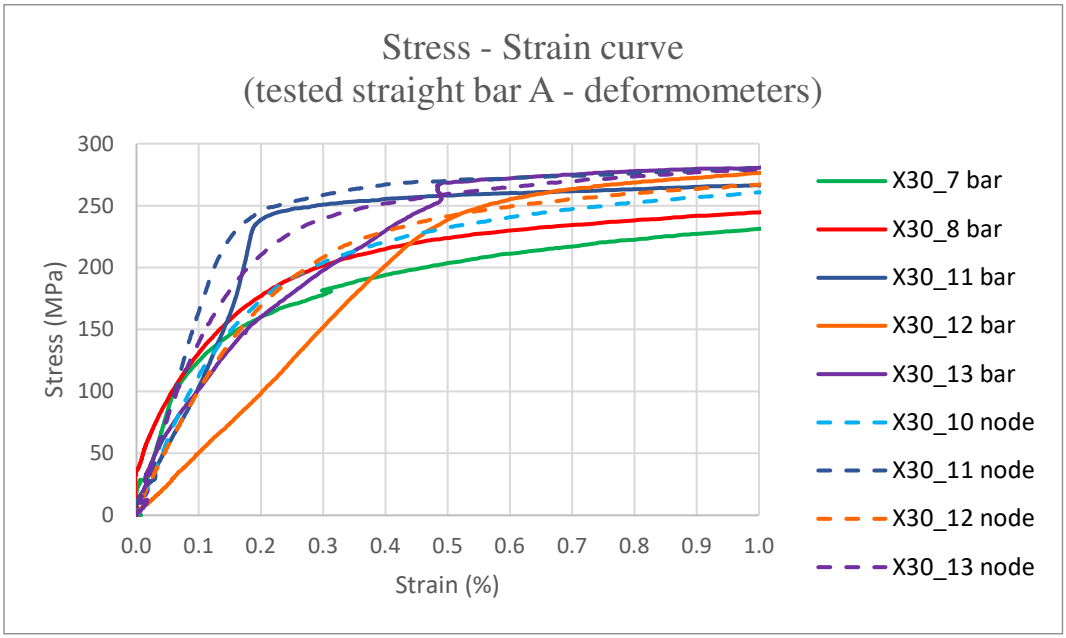

Figure 6.21 A zoom of the effective stress-strain curves (up to 1% strain) for tensile tests on WAAM crossed-bars (X30) tested along the straight bar A.

Young's modulus (E), 0.2% proof stress ($R_{p,02}$), ultimate tensile strength (UTS), elongation to failure ($A_{\%}$) and yield-to-tensile strength ratio ($R_{p,02}$/UTS) were evaluated from the effective stress-strain curves. These main mechanical parameters are reported in Table 6.22. The notation "bar" refers to the effective mechanical parameters provided by the linear deformometer located on the bar, instead of, the notation "node" refers to the effective mechanical parameters provided by the linear deformometer located on the node of the straight bar A.

Straight bar A with node		**E**	**Rp,02**	**UTS**	**A%**	**Rp,02/UTS**
		[GPa]	**[MPa]**	**[MPa]**	**[%]**	**[-]**
X30_7	bar	139.33	183.35	360.19	14.44	0.51
X30_8	bar	137.87	206.10	483.97	28.61	0.43
X30_10	node	125.44	221.40	378.94	14.43	0.58
X30_11	bar	89.57	258.68	432.96	19.69	0.60
	node	178.04	227.90			0.53
X30_12	bar	50.93	236.16	469.09	21.26	0.50
	node	100.94	222.66			0.47
X30_13	bar	69.24	211.35	484.22	26.10	0.44
	node	138.07	253.62			0.52

Table 6.22 Key effective mechanical parameters from tensile tests on WAAM crossed-bars (X30) tested along the straight bar A provided by the two deformometers on both bar and node.

Straight bar A with node (X10)		
E_{av}(bar)	**[GPa]**	97.39
E_{av}(node)	**[GPa]**	135.62
E_{av}(bar)/E_{av}(node)	**[-]**	0.72
UTS_{av}	**[MPa]**	434.89

Table 6.23 Mean values of Young's modulus and ultimate tensile strength from tensile tests on WAAM crossed-bars (X30) tested along the straight bar A.

In the Table 6.23, the ratio between the mean values of the Young's modulus related to the bar and the node provides a value smaller than one, therefore the node exhibits an higher contribution with respect to the straight bar with the node. The coefficient of variation of the Young's modulus is higher in case of the bar with a value of 36.77%, compared to 20.57% of the node. The variation in terms of ultimate tensile strength of the straight bar A with the node is high, 11.39%.

In the Figure 6.22, the reported results refer to the tensile test performed on the inclined bar B with the node (the longitudinal axis of the bar is inclined of 30° with respect to the build direction), referring to the results collected by means of a linear deformometer of gauge length of 25 mm positioned on the bar and another one of gauge length of 50mm on the node.

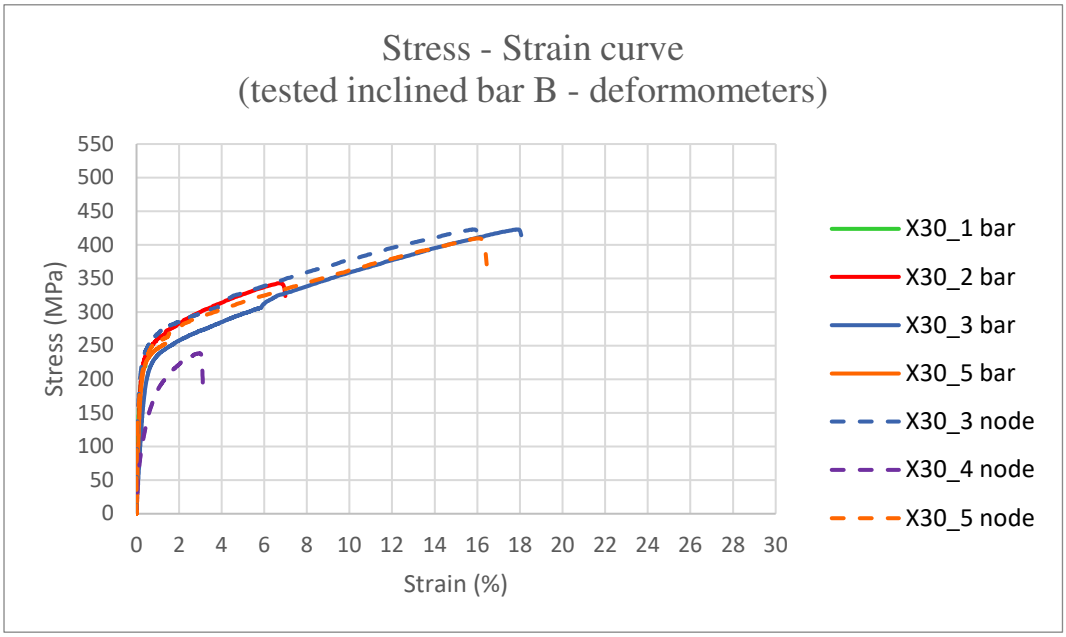

Figure 6.22 Effective stress-strain curves for tensile tests on WAAM crossed-bars (X30) tested along the inclined bar B.

A zoom of the effective stress-strain curve of WAAM crossed-bars (for strain lower than 1%) is reported in Figure 6.23 to explore the first part of the tensile test.

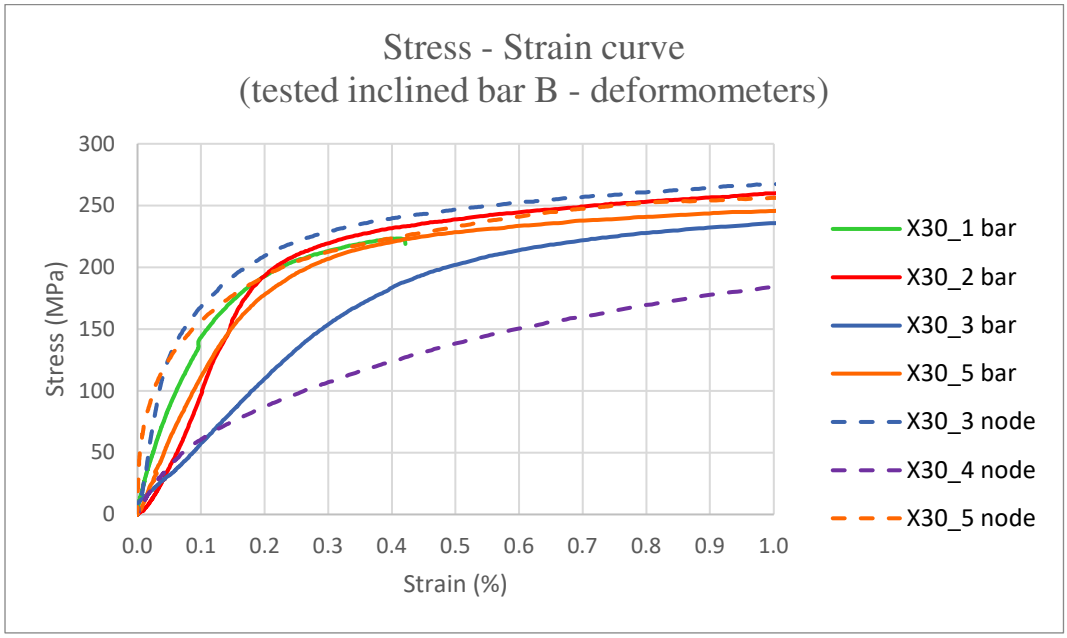

Figure 6.23 A zoom of the effective stress-strain curves (up to 1% strain) for tensile tests on WAAM crossed-bars (X30) tested along the inclined bar B.

Young's modulus (E), 0.2% proof stress ($R_{p,02}$), ultimate tensile strength (UTS), elongation to failure ($A_{\%}$) and yield-to-tensile strength ratio ($R_{p,02}$/UTS) were evaluated from the effective stress-strain curves. These main mechanical parameters are reported in Table 6.24. The notation "bar" refers to the effective mechanical parameters provided by the linear deformometer located on the bar, instead of, the notation "node" refers to the effective mechanical parameters provided by the linear deformometer located on the node of the inclined bar B.

Inclined bar B with node		E	Rp,02	UTS	A%	Rp,02/UTS
		[GPa]	[MPa]	[MPa]	[%]	[-]
X30_1	bar	154.75	216.86	223.38	0.42	0.97
X30_2	bar	121.83	222.66	342.90	8.22	0.65
X30_3	bar	54.19	209.69	422.64	18.06	0.50
	node	304.82	247.52			0.59
X30_4	node	60.71	127.47	238.58	3.14	0.53
X30_5	bar	89.55	211.47	409.54	16.47	0.52
	node	249.93	223.78			0.55

Table 6.24 Key effective mechanical parameters from tensile tests on WAAM crossed-bars (X30) tested along the inclined bar B.

Inclined bar B with node (X10)		
E_{av}(bar)	**[GPa]**	105.08
E_{av}(node)	**[GPa]**	205.16
E_{av}(bar)/E_{av}(node)	**[-]**	0.51
UTS_{av} [MPa]	**[MPa]**	327.41

Table 6.25 Mean values of Young's modulus and ultimate tensile strength from tensile tests on WAAM crossed-bars (X30) tested along the inclined bar B.

In the Table 6.25, the ratio between the mean values of the Young's modulus related to the bar and the node exhibits a node contribution nearly doubled with respect to the inclined bar with the node. The coefficient of variation of the Young's modulus is very high in the node with a value of 50.97%, compared to 35.54% of the bar. The variation in terms of ultimate tensile strength of the inclined bar B with the node is 25.47%.

6.3.2.4. Strain gauges

As presented in the Section 6.3.2 some WAAM crossed-bars specimens were tested with the addition of strain gauges to the others monitoring systems (Figure 6.24), in order to obtain local information about the linear deformation of the specimen up to yielding.

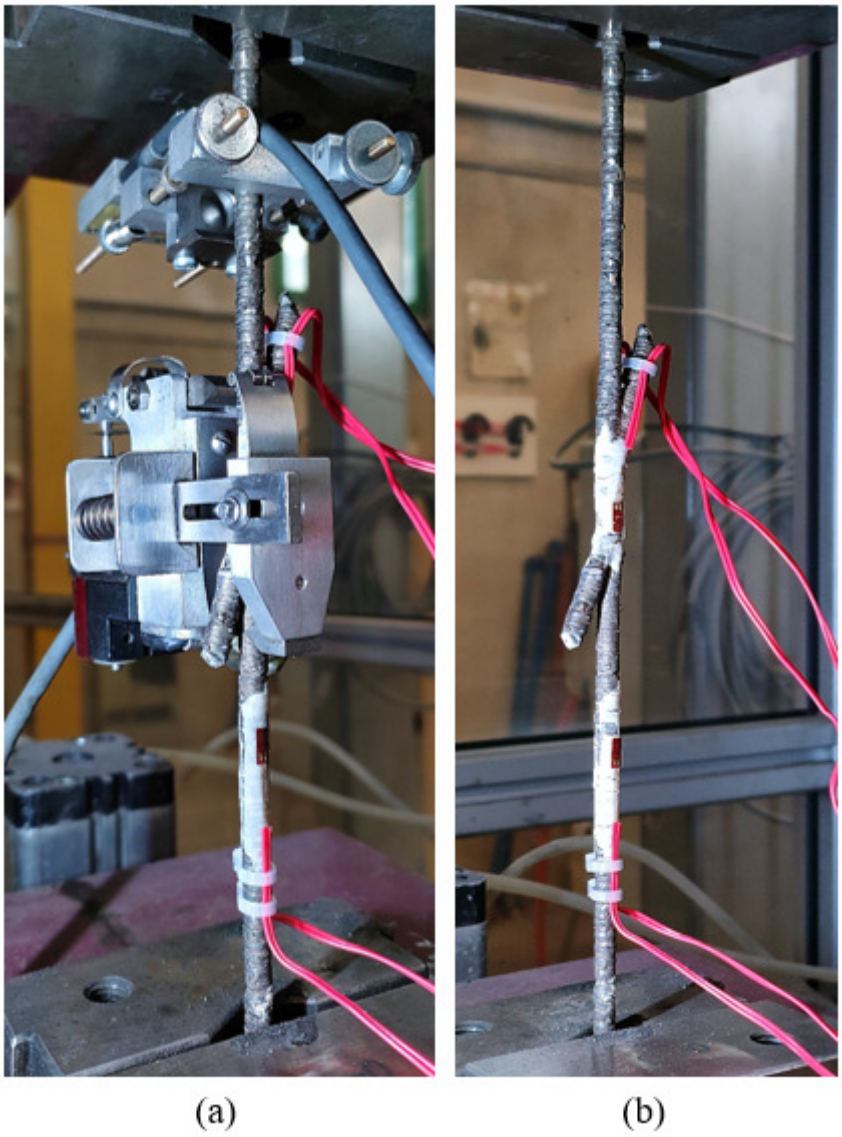

Figure 6.24 Experimental tensile test setup in case of WAAM crossed-bars specimens: (a) with two deformometers and four strain gauges, (b) with only four strain gauges.

A zoom of the effective stress-strain curve of WAAM crossed-bars (for strain lower than 1%) is reported in Figure 6.25 to explore the different response related to the monitoring system and its location on the specimen, in order to capture discrepancies from global to local information.

The WAAM crossed-bars "X10_10" was tested along the straight bar A with the node, which has the build direction coincident with the longitudinal axis. The same was performed on the specimens "X10_15", "X20_15", "X30_12" and "X30_13". The effective stress-strain curves of WAAM crossed-bars referred to linear deformometers and strain gauges are reported on the same graph (Figures 6.25, 6.26, 6.27, 6.28 and 6.29): one of both measuring systems was positioned on the bar and the others on the node (in particular, the linear deformometer of gauge length of 25 mm on the bar and the other one of gauge length of 50 mm on the node).

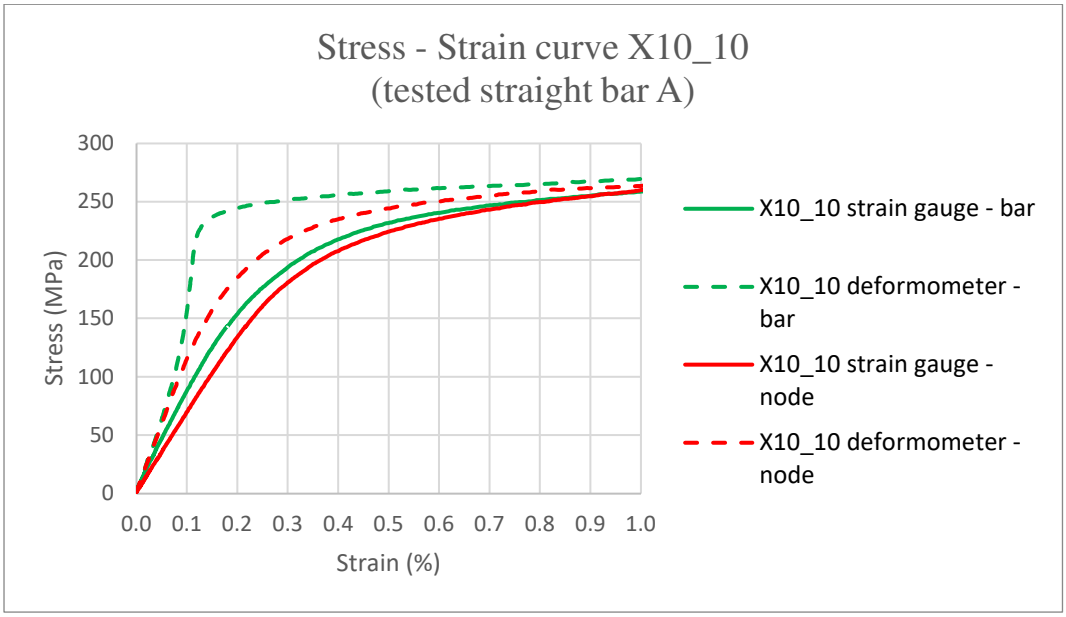

Figure 6.25 A zoom of the effective stress-strain curves (up to 1% strain) for tensile tests on WAAM crossed-bars (X10_10) tested along the straight bar A with information about both bar and intersection from linear deformometers and strain gauges.

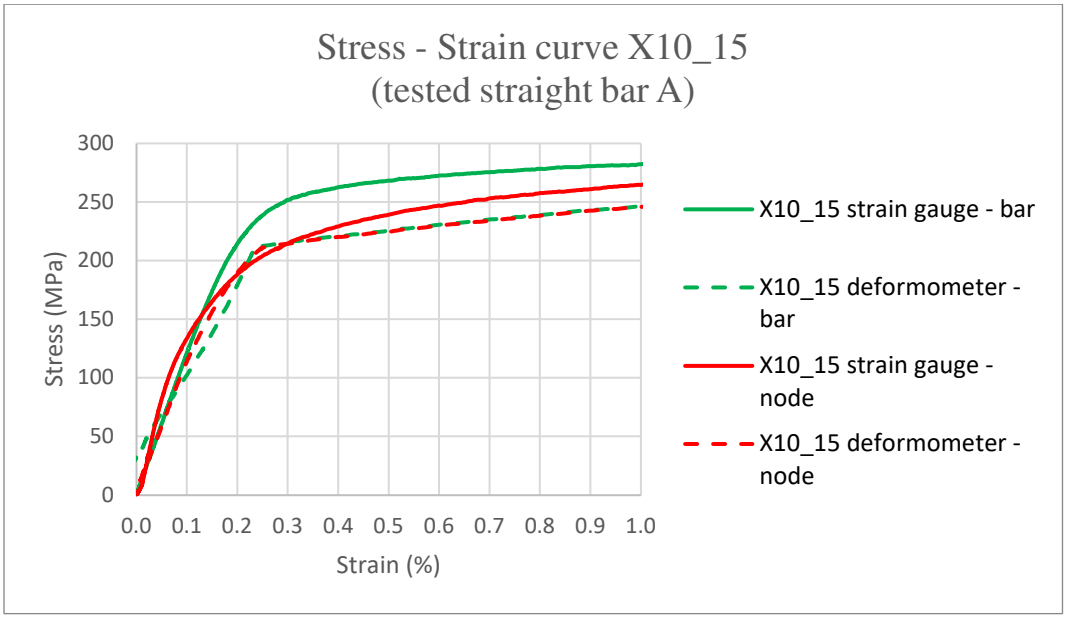

Figure 6.26 A zoom of the effective stress-strain curves (up to 1% strain) for tensile tests on WAAM crossed-bars (X10_15) tested along the straight bar A with information about both bar and intersection from linear deformometers and strain gauges.

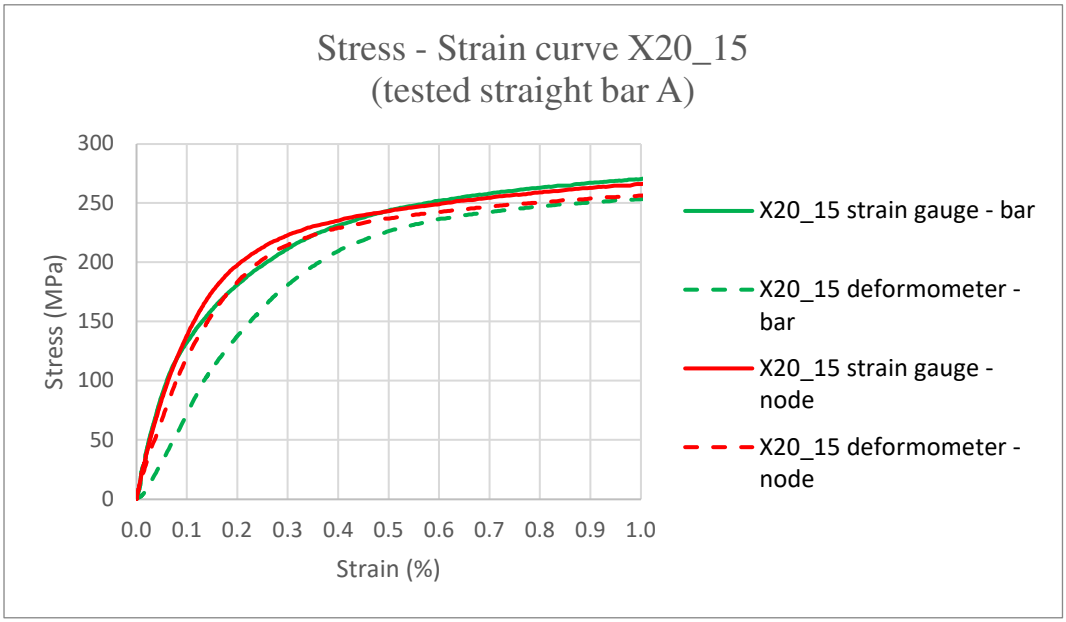

Figure 6.27 A zoom of the effective stress-strain curves (up to 1% strain) for tensile tests on WAAM crossed-bars (X20_15) tested along the straight bar A with information about both bar and intersection from linear deformometers and strain gauges.

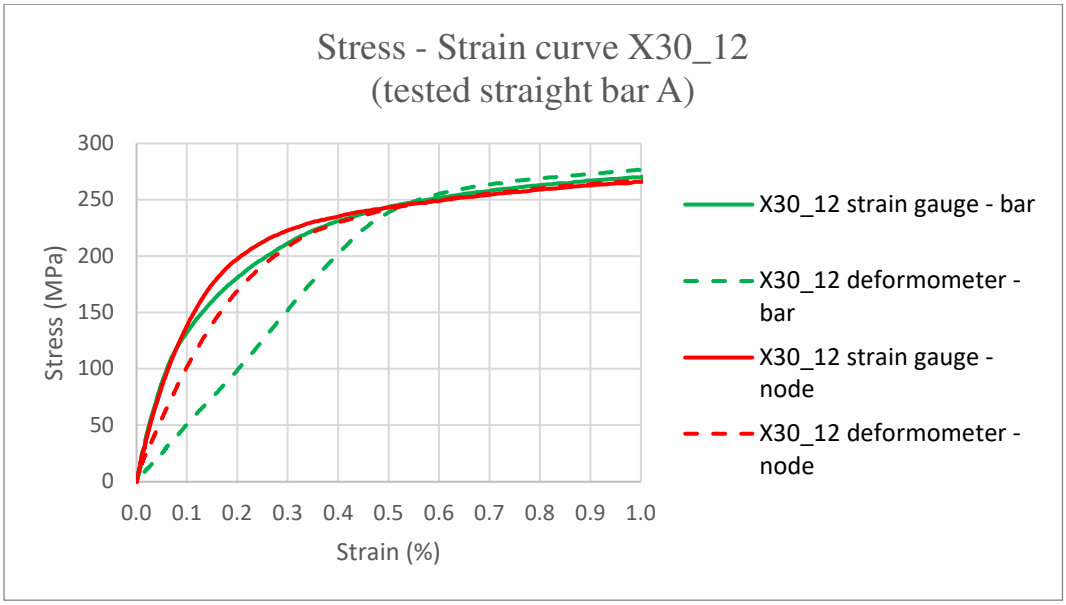

Figure 6.28 A zoom of the effective stress-strain curves (up to 1% strain) for tensile tests on WAAM crossed-bars (X30_12) tested along the straight bar A with information about both bar and intersection from linear deformometers and strain gauges.

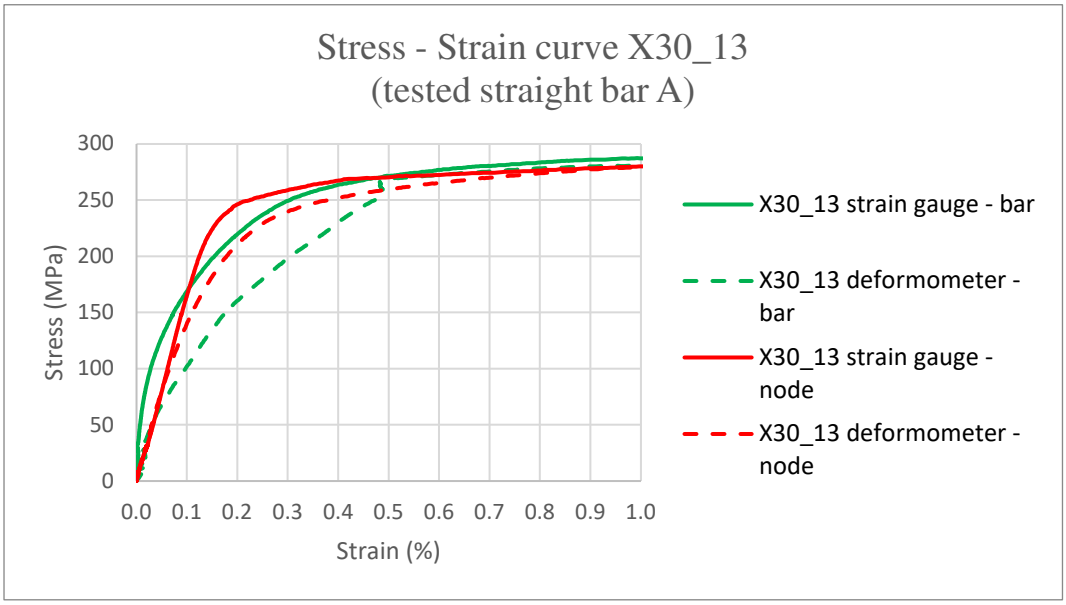

Figure 6.29 A zoom of the effective stress-strain curves (up to 1% strain) for tensile tests on WAAM crossed-bars (X30_13) tested along the straight bar A with information about both bar and intersection from linear deformometers and strain gauges.

The WAAM crossed-bars "X30_3" was tested along the inclined bar B, which has an inclination of 30° of the longitudinal axis of the bar with respect to the build direction. The effective stress-strain curves of WAAM crossed-bars referred to linear deformometers and strain gauges are reported on the same graph (Figure 6.30): one of both measuring systems was positioned on the bar and the others on the node (in particular, the linear deformometer of gauge length of 25 mm on the bar and the other one of gauge length of 50 mm on the node).

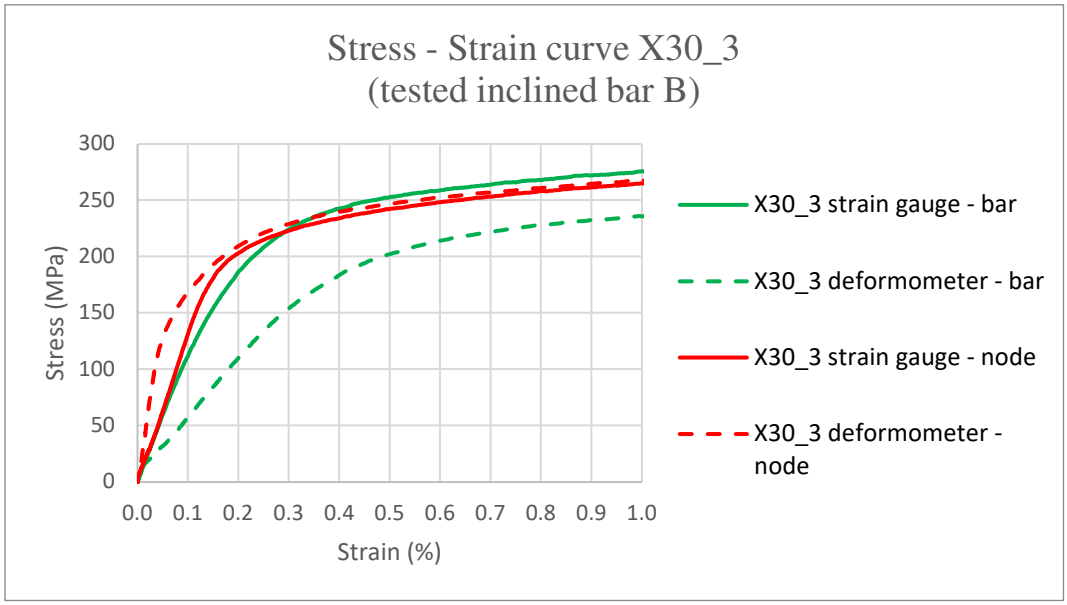

Figure 6.30 A zoom of the effective stress-strain curves (up to 1% strain) for tensile tests on WAAM crossed-bars (X30_3) tested along the bar B with information about both bar and intersection from linear deformometers and strain gauges.

The stress-strain curves obtained from tensile tests on WAAM crossed-bars specimens in case of strain gauges as monitoring systems are compared in order to detect whether the crossed-bars inclination affects the key mechanical parameters, although the analyzed information are derived from the straight bar A, hence the one with the vertical build direction coincident with the longitudinal axis. In particular, the monitoring systems placed on the bar of the straight bar A with the node should provide a response in line between each other, due to the same longitudinal axis inclination. Instead of, the monitoring systems placed on the intersection provide information which can be adopted to exhibit the possible influence of the bar inclination on the mechanical response of the intersection point, consequently on the tensile response of the entire WAAM crossed-bars specimen.

In the Figure 6.31, the effective stress-strain curves of WAAM crossed-bars referred to the results collected by means of only strain gauges are reported on the same graph (located both on the bar and on the node).

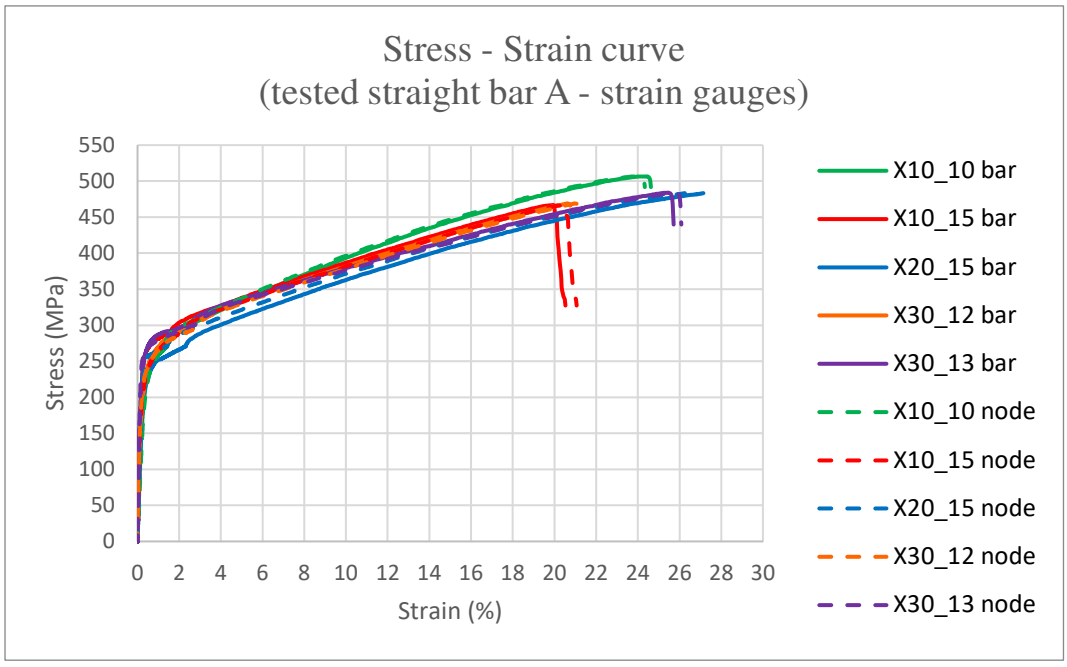

Figure 6.31 Effective stress-strain curves for tensile tests on WAAM crossed-bars for different orientations tested along the straight bar A with information about both bar and node by means of strain gauges.

The Figure 6.32 reports a zoom of the effective stress-strain curves of WAAM crossed-bars (for strain up to 1%).

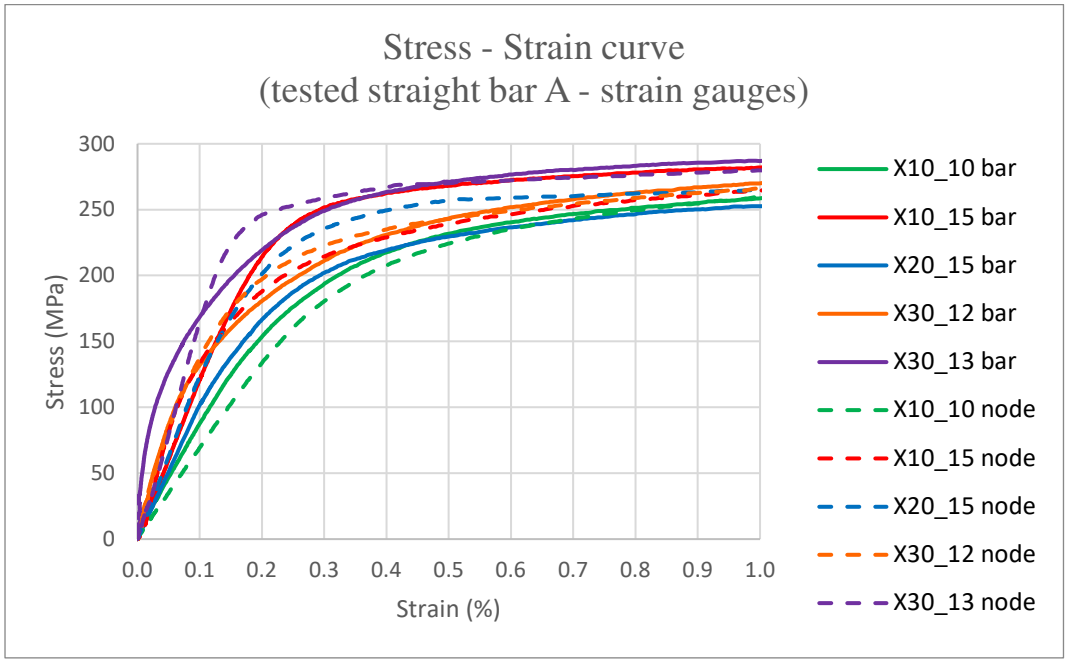

Figure 6.32 A zoom of the effective stress-strain curves (up to 1% strain) for tensile tests on WAAM crossed-bars for different orientations tested along the straight bar A with information about both bar and node by means of strain gauges.

6.4. Tensile test on single bars

The following step of the current research is focused to assess the behavior of single bars derived from the WAAM crossed-bars specimens already tested in the previous Section 6.3. The bars are the ones not involved in the performed tests (Figure 6.33), however they were tested in traction in order to compare the behavior of bars with intersection with the ones without it, with the objective to study how the intersection influences the overall behavior of the element.

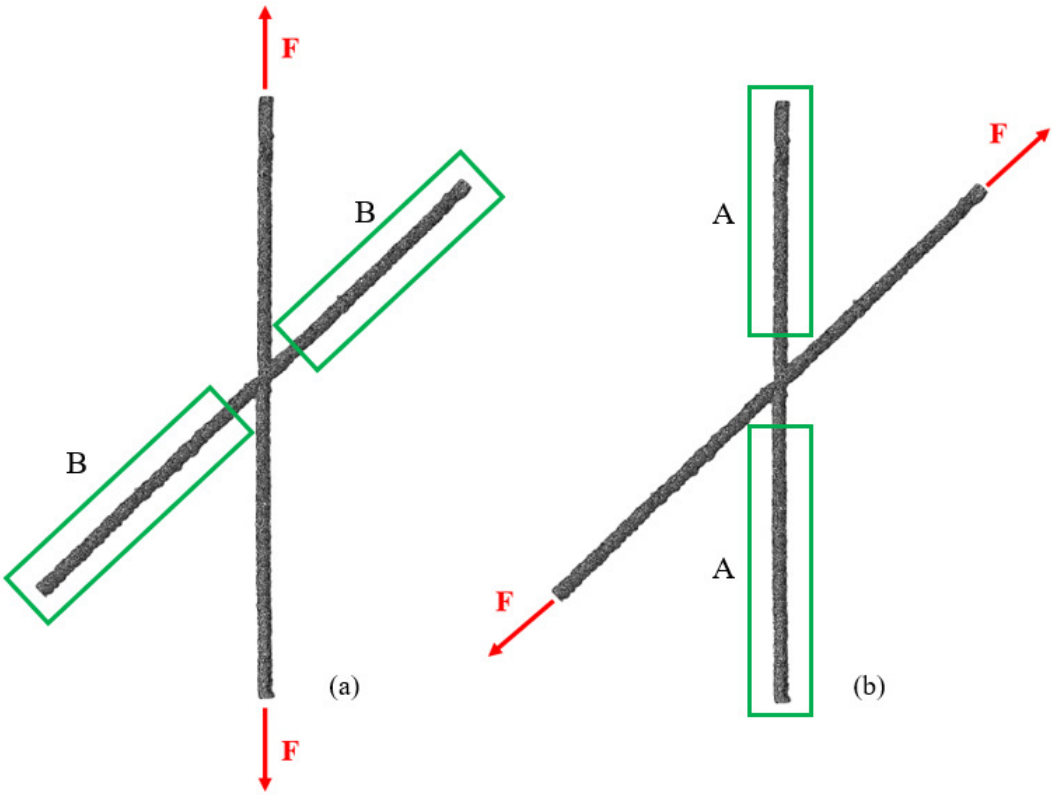

Figure 6.33 Tensile test along the bars enclosed in the green boxes.

The relative direction of the tested portion with respect to the printing layers deposited is taken into account also into this tests phase. The possible cases during the testing phase are two, depending on the tested bar: bar B has a longitudinal axis inclined by a certain angle, respectively 10°, 20° and 30° (referred to by name X10, X20, X30) with respect to the vertical direction, otherwise straight bar A has a longitudinal axis aligned along the vertical direction, coincident with the printing direction.

Geometrical characterization and tensile tests were carried out over a total of 20 specimens. Between them, 6 were X10, 6 of X20 and 8 of X30 series of specimens.

6.4.1. Geometrical characterization

As exposed in the section 6.2, the possible measuring systems to be adopted performing the geometrical characterization are three. Among these, in this section the only one used is the volume-based measurements.

Hereafter, the geometrical characterization is performed on single bars which belong to WAAM crossed-bars already characterized. Hence, the characterization has the objective to present an effective diameter only related to this portion of the entire WAAM specimen.

6.4.1.1. X10

The effective cross-sectional area, A_{eff}, is derived using an average value as obtained from volumetric measurements on as-built specimens. The Table 6.26 presents the volume-based measures of the effective diameter. Additionally, the average, standard deviation and covariance values are reported.

Specimen	**Dry Weight**	**Hydrostatic specific Weight**	**Volume**	**A_{av}**	**d_{av}**
-	**[g]**	**[g]**	**[m^3]**	**[mm^3]**	**[mm]**
X10_2_A2	20.84	18.48	0.002	23.63	5.48
X10_3_A1	20.67	18.13	0.003	24.93	5.63
X10_4_A1	19.44	17.03	0.002	24.88	5.63
X10_8_B1	20.14	17.97	0.002	22.17	5.31
X10_9_B2	19.43	17.32	0.002	21.56	5.24
X10_11_B1	20.58	18.31	0.002	22.28	5.33
Average	20.18	17.87	0.002	23.24	5.44
Stand. Dev.	0.57	0.52	0.0001	1.33	0.16
COV [%]	2.82	2.94	6.29	5.72	2.85

Table 6.26 Volume-based measures of the diameter of single bars X10.

6.4.1.2. X20

The Table 6.27 presents the volume-based measures of the effective diameter. Additionally, the average, standard deviation and covariance values are reported.

Specimen	**Dry Weight**	**Hydrostatic specific Weight**	**Volume**	**A_{av}**	**d_{av}**
-	**[g]**	**[g]**	**[m^3]**	**[mm^3]**	**[mm]**
X20_2_A1	22.17	19.27	0.003	26.42	5.80
X20_3_A2	23.59	20.58	0.003	27.17	5.88
X20_4_A2	21.62	18.79	0.003	26.26	5.78
X20_8_B2	22.57	19.53	0.003	26.49	5.81
X20_9_B2	21.67	18.84	0.003	26.02	5.76
X20_11_B1	23.38	20.38	0.003	26.72	5.83
Average	22.50	19.57	0.003	26.51	5.81
Stand. Dev.	0.77	0.70	0.0001	0.37	0.04
COV [%]	3.41	3.56	2.92	1.38	0.69

Table 6.27 Volume-based measures of the diameter of single bars X20.

6.4.1.3. X30

The Table 6.28 presents the volume-based measures of the effective diameter. Additionally, the average, standard deviation and covariance values are reported.

Specimen	**Dry Weight**	**Hydrostatic specific Weight**	**Volume**	**A_{av}**	**d_{av}**
-	**[g]**	**[g]**	**[m^3]**	**[mm^3]**	**[mm]**
X30_1_A1	23.85	20.8	0.003	26.57	5.82
X30_1_A2	21.72	18.95	0.003	24.56	5.59
X30_2_A1	22.73	19.84	0.003	26.21	5.78
X30_2_A2	24.16	21.08	0.003	25.72	5.72
X30_7_B1	22.59	19.73	0.003	24.60	5.60
X30_7_B2	21.09	18.4	0.003	24.07	5.54
X30_8_B1	23.46	20.46	0.003	26.37	5.79
X30_8_B2	22.66	19.75	0.003	24.92	5.63
Average	22.78	19.88	0.003	25.38	5.68
Stand. Dev.	0.97	0.85	0.0001	0.90	0.10
COV [%]	4.26	4.25	4.34	3.53	1.77

Table 6.28 Volume-based measures of the diameter of single bars X30.

6.4.2. Results

The tensile tests were performed on a universal testing machine of 500 kN load capacity, as for all the previous WAAM specimens tested. They were tested under displacement-control with a velocity corresponding to a load rate of 2 MPa/s according to (ISO6892-1 2009).

The longitudinal elongation of each specimen has been measured using a Linear Variable Differential Transformer (LLVDT). In this case, only one monitoring system was adopted, based on the specimen configuration composed of only a single bar. A linear deformometer of gauge length of 25 mm was adopted to evaluate the strains, detecting the effective strain of the specimens up to yielding.

Young's modulus (E), 0.2% proof stress ($R_{p,02}$), ultimate tensile strength (UTS), elongation to failure ($A_{\%}$) were evaluated from the effective stress-strain curves.

Figure 6.6 shows the adopted testing setup.

Figure 6.34 Experimental tensile test setup in case of WAAM single bars specimens.

The adopted notation indicates the tested specimen plus the letter referred to the bar on which the tensile test was performed and a number, taking into account both the bars obtained from the same WAAM crossed-bar (e.g. X10_2_A2 is obtained from the straight bar A of the specimen number 2 belonging to the specimen type with the bar inclination of 10°, and the tested bar was the second one).

6.4.2.1. X10

The tensile tests were performed obtaining information to be interpreted by means of the effective cross-sectional area. The effective stress values (σ_{eff}) were computed according to the Equation (10), while the effective strain values were computed according to the Equation (11), considering a gauge length of 25 mm. The information are then organized in an effective stress-strain curve of WAAM single bars derived from the WAAM crossed-bars. In particular, the stress-strain curves related to the same single bar typology (same relative direction of the single bar longitudinal axis with respect to the printing layers deposited) are reported on the same graph, in order to compare WAAM single bars obtained from the same batch of WAAM crossed-bars.

The results are reported for both the testing method, referring to the tensile test performed on the bar A (named as “straight bar”, the build direction is coincident with the longitudinal axis of the bar) and the one performed on the bar B (named as “inclined bar”, the longitudinal axis of the bar is inclined of 10° with respect to the build direction).

In the Figure 6.35, the reported results refer to the tensile test performed on the straight bar A (the build direction is coincident with the longitudinal axis of the bar), referring to the results collected by means of a linear deformometer of gauge length of 25 mm positioned on the bar.

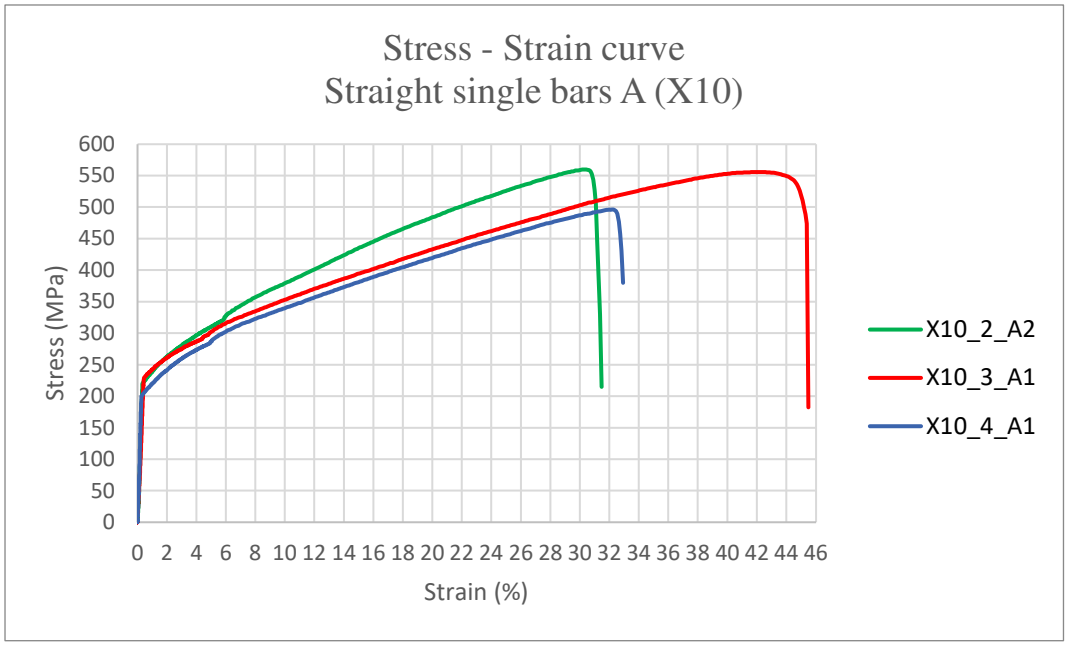

Figure 6.35 Effective stress-strain curves for tensile tests on WAAM single bars tested along the direction A obtained from crossed-bars X10.

To explore the first part of the tensile test, exhibiting the Young's modulus and the 0.2% proof stress values, a zoom of the effective stress-strain curves of WAAM single bars (for strain lower than 1%) is reported in Figure 6.36.

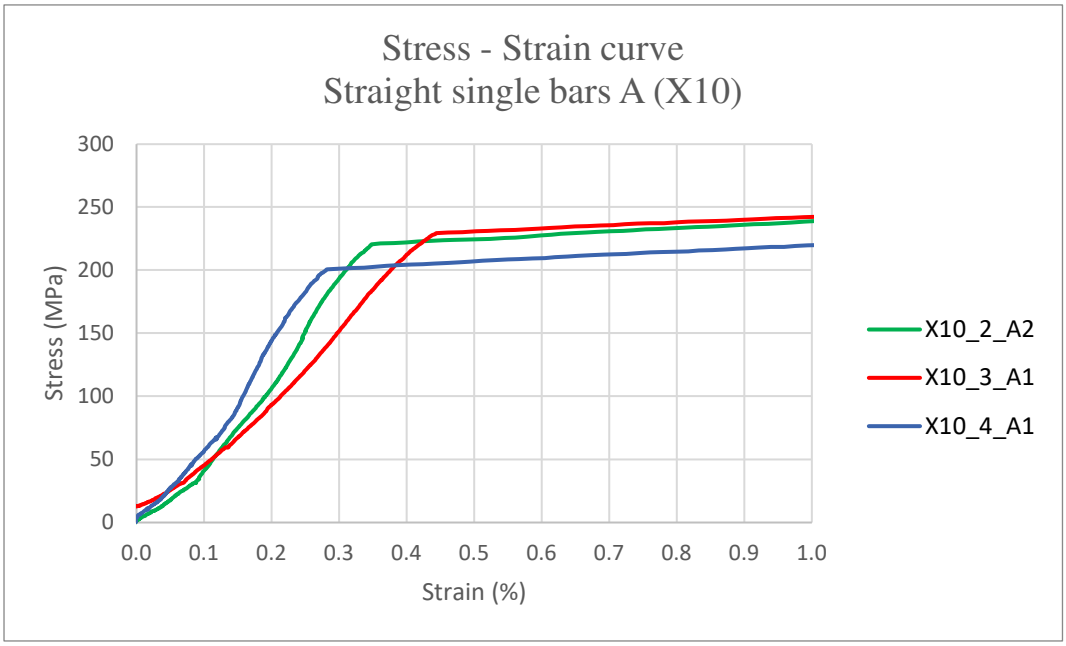

Figure 6.36 A zoom of the effective stress-strain curves (up to 1% strain) for tensile tests on WAAM single bars tested along the direction A obtained from crossed-bars X10.

Young's modulus (E), 0.2% proof stress ($R_{p,02}$), ultimate tensile strength (UTS), elongation to failure ($A_{\%}$) and yield-to-tensile strength ratio ($R_{p,02}$/UTS) were evaluated from the effective stress-strain curves. These main mechanical parameters are reported in Table 6.29.

Straight bar A	**E**	**Rp,02**	**UTS**	**A%**	**Rp,02/UTS**
	[GPa]	**[MPa]**	**[MPa]**	**[%]**	**[-]**
X10_2_A2	79.91	224	559.92	32.99	0.40
X10_3_A1	55.36	236.93	555.79	46.47	0.43
X10_4_A1	80.41	207.25	496.22	34.06	0.42

Table 6.29 Key effective mechanical parameters from tensile tests on WAAM single bars tested along the direction A obtained from crossed-bars X10.

Straight bar A (X10)		
E_{av}(bar)	**[GPa]**	71.89
UTS_{av}	**[MPa]**	537.31

Table 6.30 Mean values of Young's modulus and ultimate tensile strength from tensile tests on WAAM single bars tested along the direction A obtained from crossed-bars X10.

In the Table 6.30, the coefficient of variation of the Young's modulus is 16.26%. The variation in terms of ultimate tensile strength of the straight bar A is 5.42%.

In the Figure 6.37, the reported results refer to the tensile test performed on the inclined bar B (the longitudinal axis of the bar is inclined of 10° with respect to the build direction), referring to the results collected by means of a linear deformometer of gauge length of 25 mm positioned on the bar.

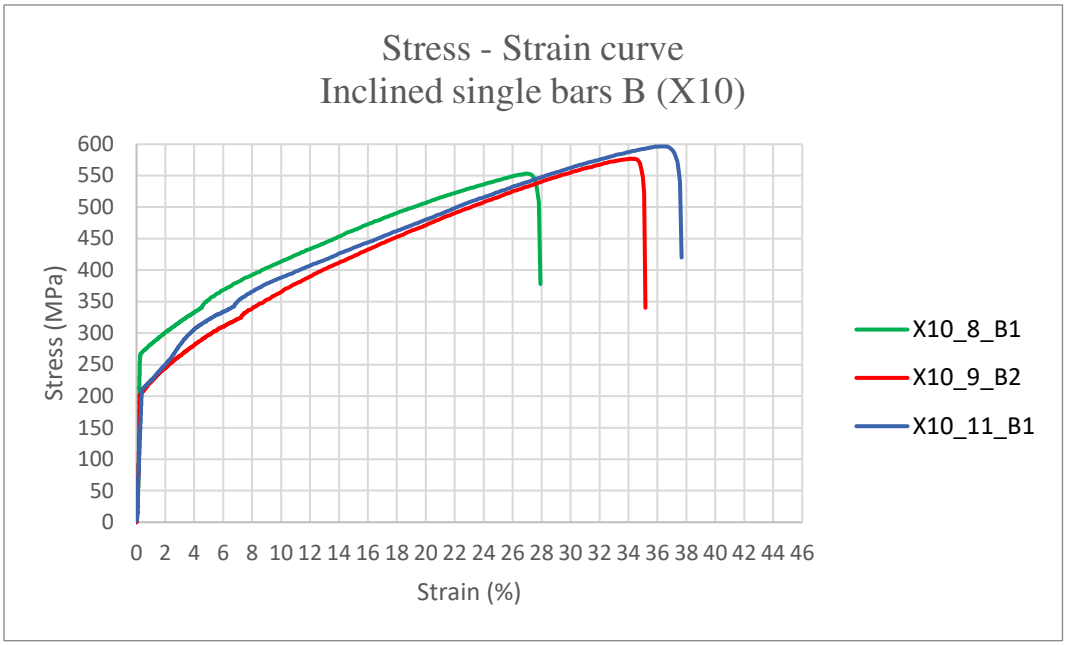

Figure 6.37 Effective stress-strain curves for tensile tests on WAAM single bars tested along the direction B obtained from crossed-bars X10.

A zoom of the effective stress-strain curves of WAAM single bars (for strain lower than 1%) is reported in Figure 6.38 to explore the first part of the tensile test.

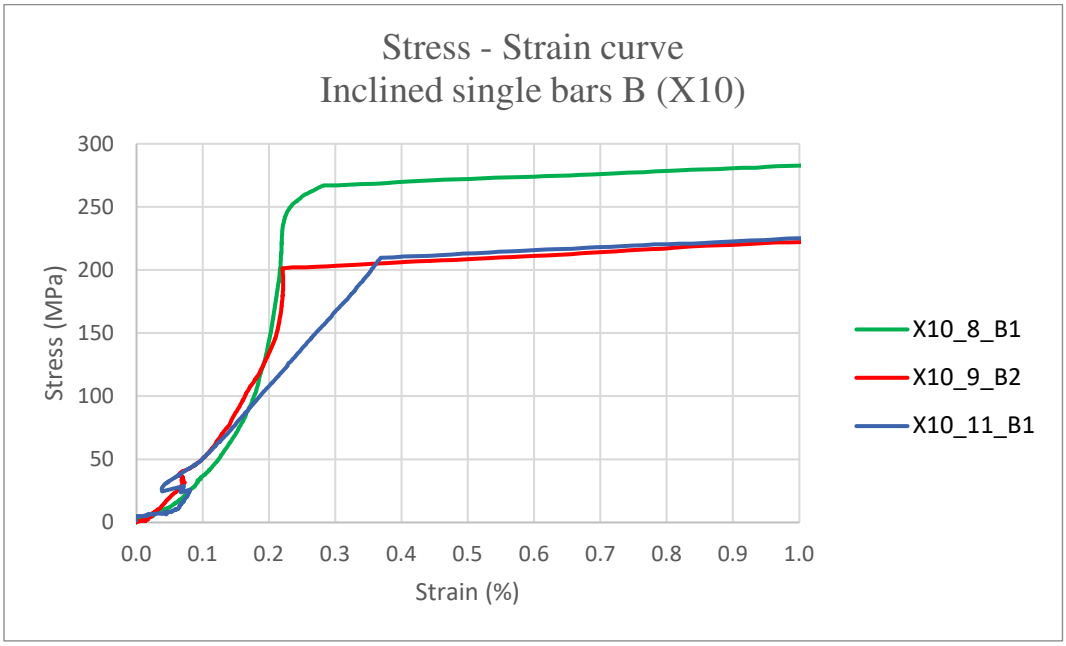

Figure 6.38 A zoom of the effective stress-strain curves (up to 1% strain) for tensile tests on WAAM single bars tested along the direction B obtained from crossed-bars X10.

Young's modulus (E), 0.2% proof stress ($R_{p,02}$), ultimate tensile strength (UTS), elongation to failure ($A_{\%}$) and yield-to-tensile strength ratio ($R_{p,02}$/UTS) were evaluated from the effective stress-strain curves. These main mechanical parameters are reported in Table 6.31.

Inclined bar B	**E**	**Rp,02**	**UTS**	**A%**	**Rp,02/UTS**
	[GPa]	**[MPa]**	**[MPa]**	**[%]**	**[-]**
X10_8_B1	101.51	277.53	553.37	28.96	0.50
X10_9_B2	74.81	203.31	576.89	36.23	0.35
X10_11_B1	53.78	212.04	596.44	38.61	0.36

Table 6.31 Key effective mechanical parameters from tensile tests on WAAM single bars tested along the direction B obtained from crossed-bars X10.

Inclined bar B (X10)		
E_{av}(bar)	**[GPa]**	76.70
UTS_{av} [MPa]	**[MPa]**	575.57

Table 6.32 Mean values of Young's modulus and ultimate tensile strength from tensile tests on WAAM single bars tested along the direction B obtained from crossed-bars X10.

In the Table 6.32, the coefficient of variation of the Young's modulus is 25.46%. The variation is terms of ultimate tensile strength of the inclined bar B is 3.06%.

6.4.2.2. X20

The effective stress values (σ_{eff}) were computed according to the Equation (10), while the effective strain values were computed according to the Equation (11), considering a gauge length of 25 mm. The information are then organized in an effective stress-strain curve of WAAM single bars derived from the WAAM crossed-bars. In particular, the stress-strain curves related to the same single bar typology (same relative direction of the single bar longitudinal axis with respect to the printing layers deposited) are reported on the same graph, in order to compare WAAM single bars obtained from the same batch of WAAM crossed-bars.

The results are reported for both the testing method, referring to the tensile test performed on the bar A (named as "straight bar", the build direction is coincident with the longitudinal axis of the bar) and the one performed on the bar B (named as "inclined bar", the longitudinal axis of the bar is inclined of 20° with respect to the build direction).

In the Figure 6.39, the reported results refer to the tensile test performed on the straight bar A (the build direction is coincident with the longitudinal axis of the bar), referring to the results collected by means of a linear deformometer of gauge length of 25 mm positioned on the bar.

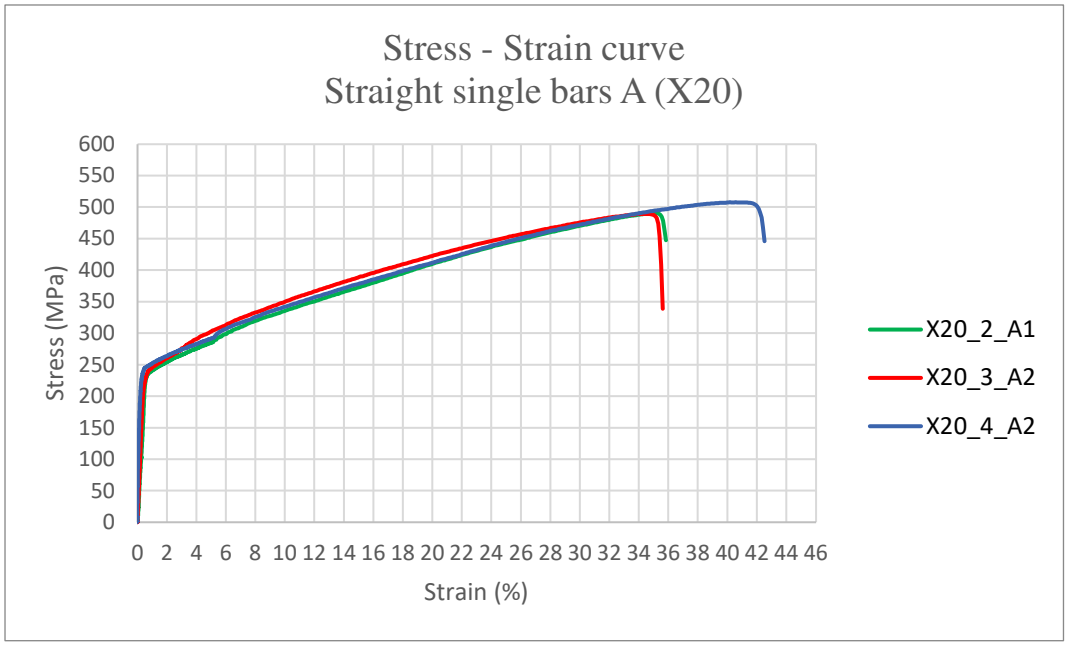

Figure 6.39 Effective stress-strain curves for tensile tests on WAAM single bars tested along the direction A obtained from crossed-bars X20.

To explore the first part of the tensile test, exhibiting the Young's modulus and the 0.2% proof stress values, a zoom of the effective stress-strain curves of WAAM single bars (for strain lower than 1%) is reported in Figure 6.40.

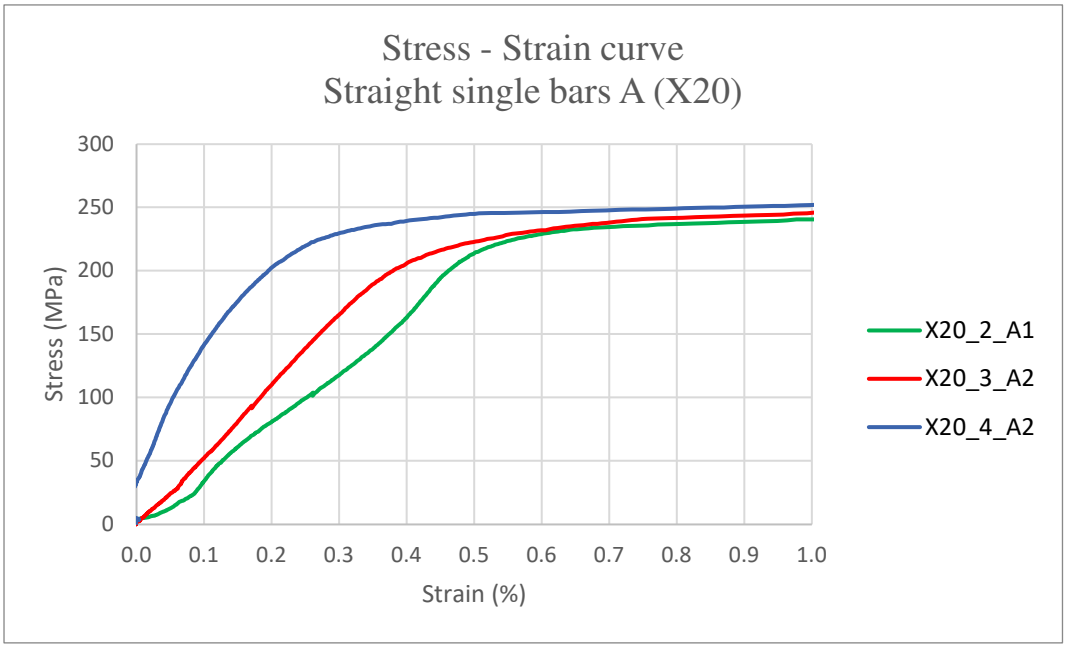

Figure 6.40 A zoom of the effective stress-strain curves (up to 1% strain) for tensile tests on WAAM single bars tested along the direction A obtained from crossed-bars X20.

Young's modulus (E), 0.2% proof stress ($R_{p,02}$), ultimate tensile strength (UTS), elongation to failure ($A_{\%}$) and yield-to-tensile strength ratio ($R_{p,02}$/UTS) were evaluated from the effective stress-strain curves. These main mechanical parameters are reported in Table 6.33.

Straight bar A	**E**	**Rp,02**	**UTS**	**A%**	**Rp,02/UTS**
	[GPa]	**[MPa]**	**[MPa]**	**[%]**	**[-]**
X20_2_A1	50.60	248.25	490.88	35.83	0.51
X20_3_A2	60.34	234.46	489.35	35.60	0.48
X20_4_A2	89.28	245.00	507.70	42.53	0.48

Table 6.33 Key effective mechanical parameters from tensile tests on WAAM single bars tested along the direction A obtained from crossed-bars X20.

Straight bar A (X20)		
E_{av}(bar)	**[GPa]**	66.74
UTS_{av}	**[MPa]**	495.98

Table 6.34 Mean values of Young's modulus and ultimate tensile strength from tensile tests on WAAM single bars tested along the direction A obtained from crossed-bars X20.

In the Table 6.34, the coefficient of variation of the Young's modulus is 24.61%. The variation in terms of ultimate tensile strength of the straight bar A is 1.68%.

In the Figure 6.41, the reported results refer to the tensile test performed on the inclined bar B (the longitudinal axis of the bar is inclined of 20° with respect to the build direction), referring to the results collected by means of a linear deformometer of gauge length of 25 mm positioned on the bar.

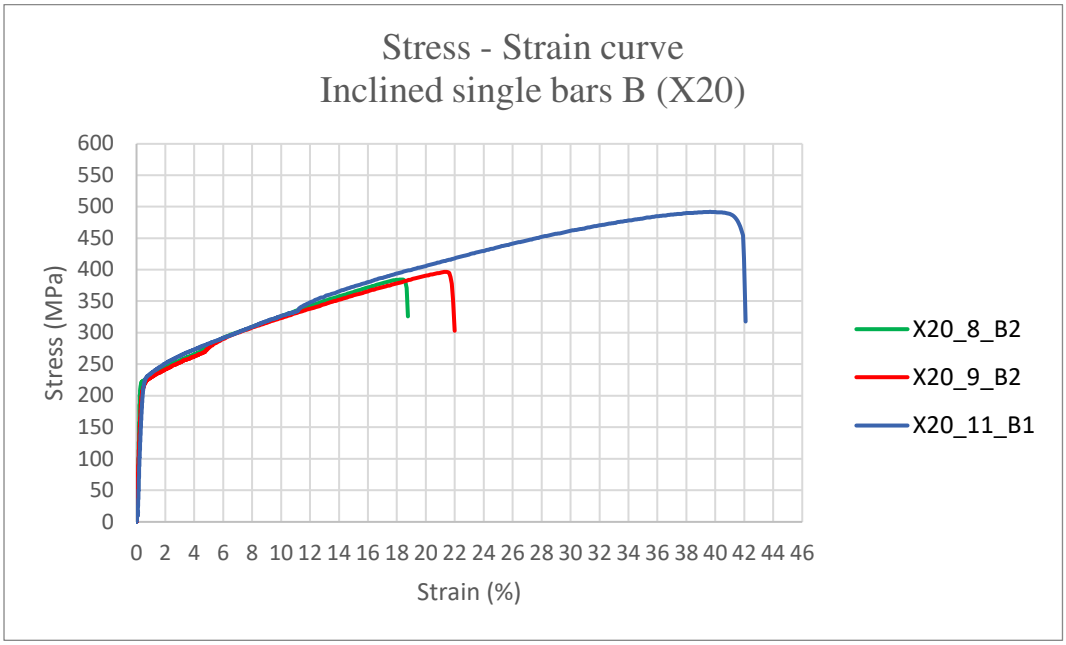

Figure 6.41 Effective stress-strain curves for tensile tests on WAAM single bars tested along the direction B obtained from crossed-bars X20.

A zoom of the effective stress-strain curves of WAAM single bars (for strain lower than 1%) is reported in Figure 6.42 to explore the first part of the tensile test.

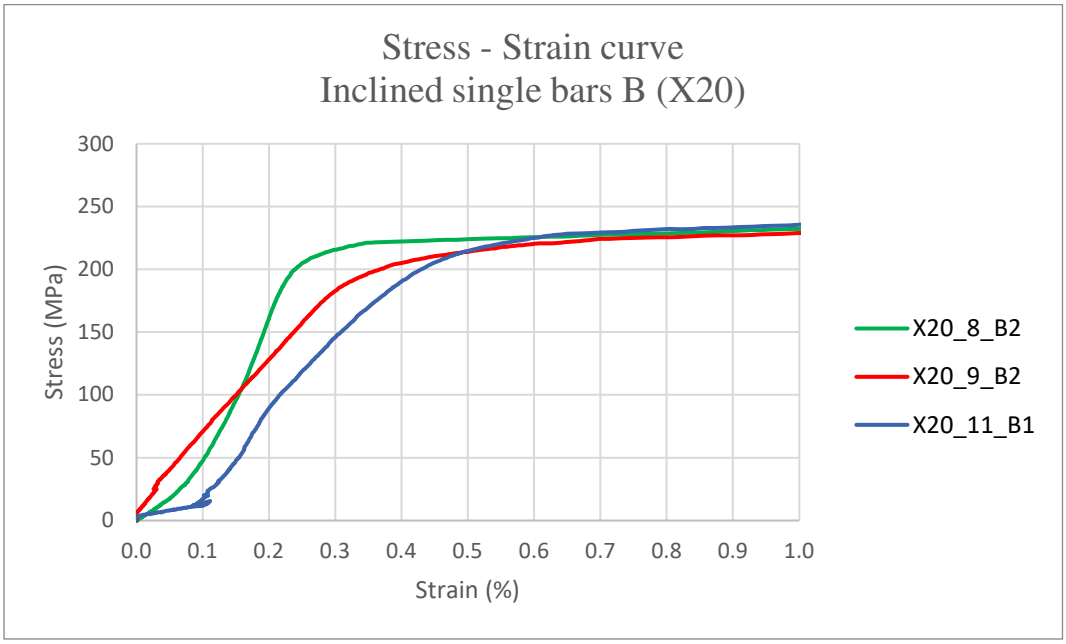

Figure 6.42 A zoom of the effective stress-strain curves (up to 1% strain) for tensile tests on WAAM single bars tested along the direction B obtained from crossed-bars X20.

Young's modulus (E), 0.2% proof stress ($R_{p,02}$), ultimate tensile strength (UTS), elongation to failure ($A_{\%}$) and yield-to-tensile strength ratio ($R_{p,02}$/UTS) were evaluated from the effective stress-strain curves. These main mechanical parameters are reported in Table 6.35.

Inclined bar B	**E**	**Rp,02**	**UTS**	**A%**	**Rp,02/UTS**
	[GPa]	**[MPa]**	**[MPa]**	**[%]**	**[-]**
X20_8_B2	103.00	221.55	384.39	18.75	0.58
X20_9_B2	55.24	222	396.43	22.98	0.56
X20_11_B1	64.02	217.94	491.81	42.08	0.44

Table 6.35 Key effective mechanical parameters from tensile tests on WAAM single bars tested along the direction B obtained from crossed-bars X20.

Inclined bar B (X20)		
E_{av}(bar)	**[GPa]**	74.09
UTS_{av} [MPa]	**[MPa]**	424.21

Table 6.36 Mean values of Young's modulus and ultimate tensile strength from tensile tests on WAAM single bars tested along the direction B obtained from crossed-bars X20.

In the Table 6.36, the coefficient of variation of the Young's modulus is 28.02%. The variation is terms of ultimate tensile strength of the inclined bar B is 11.33%.

6.4.2.3. X30

The effective stress values (σ_{eff}) were computed according to the Equation (10), while the effective strain values were computed according to the Equation (11), considering a gauge length of 25 mm. The information are then organized in an effective stress-strain curve of WAAM single bars derived from the WAMM crossed-bars. In particular, the stress-strain curves related to the same single bar typology (same relative direction of the single bar longitudinal axis with respect to the printing layers deposited) are reported on the same graph, in order to compare WAAM single bars obtained from the same batch of WAAM crossed-bars.

The results are reported for both the testing method, referring to the tensile test performed on the bar A (named as "straight bar", the build direction is coincident with the longitudinal axis of the bar) and the one performed on the bar B (named as "inclined bar", the longitudinal axis of the bar is inclined of 30° with respect to the build direction).

In the Figure 6.43, the reported results refer to the tensile test performed on the straight bar A (the build direction is coincident with the longitudinal axis of the bar), referring to the results collected by means of a linear deformometer of gauge length of 25 mm positioned on the bar.

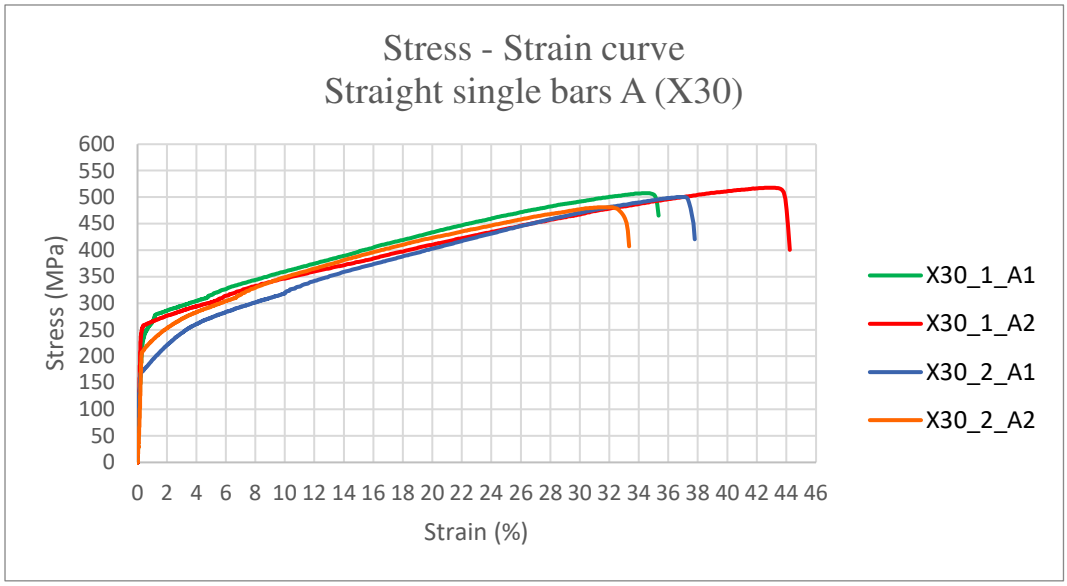

Figure 6.43 Effective stress-strain curves for tensile tests on WAAM single bars tested along the direction A obtained from crossed-bars X30.

To explore the first part of the tensile test, exhibiting the Young's modulus and the 0.2% proof stress values, a zoom of the effective stress-strain curves of WAAM single bars (for strain lower than 1%) is reported in Figure 6.44.

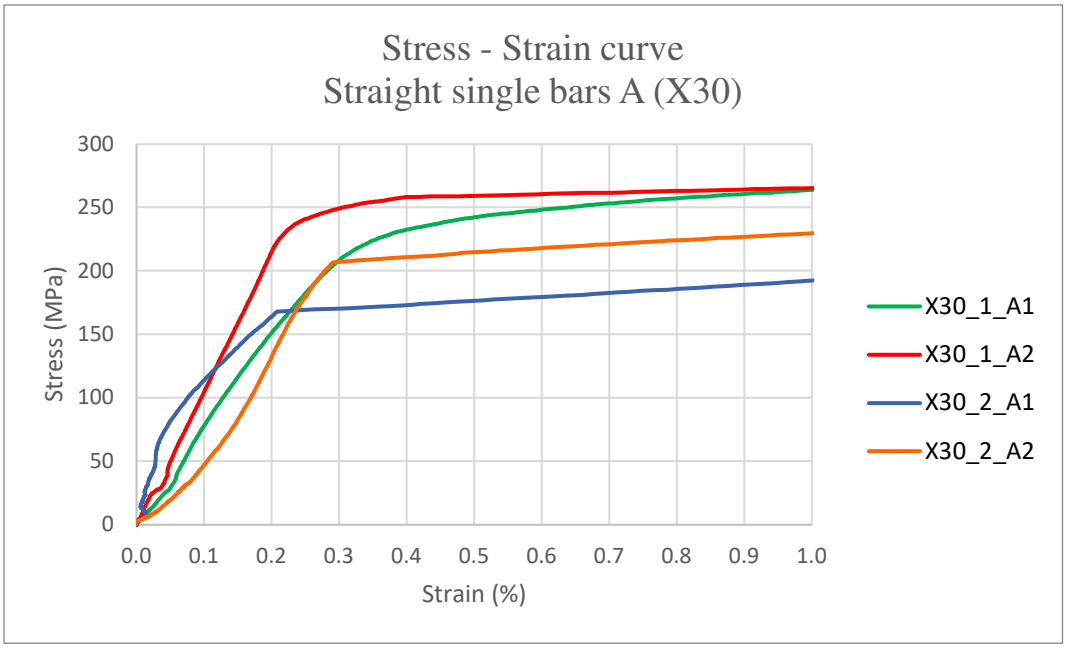

Figure 6.44 A zoom of the effective stress-strain curves (up to 1% strain) for tensile tests on WAAM single bars along the direction A obtained from crossed-bars X30.

Young's modulus (E), 0.2% proof stress ($R_{p,02}$), ultimate tensile strength (UTS), elongation to failure ($A_{\%}$) and yield-to-tensile strength ratio ($R_{p,02}$/UTS) were evaluated from the effective stress-strain curves. These main mechanical parameters are reported in Table 6.37.

Straight bar A	E	Rp,02	UTS	A%	Rp,02/UTS
	[GPa]	[MPa]	[MPa]	[%]	[-]
X30_1_A1	94.84	248.25	507.50	36.58	0.49
X30_1_A2	112.56	249.55	517.85	46.68	0.48
X30_2_A1	116.03	173.6	500.48	37.88	0.35
X30_2_A2	104.86	209.8	481.18	33.44	0.44

Table 6.37 Key effective mechanical parameters from tensile tests on WAAM single bars tested along the direction A obtained from crossed-bars X30.

Straight bar A (X30)		
E_{av}(bar)	[GPa]	107.07
UTS_{av}	[MPa]	501.75

Table 6.38 Mean values of Young's modulus and ultimate tensile strength from tensile tests on WAAM single bars tested along the direction A obtained from crossed-bars X30.

In the Table 6.38, the coefficient of variation of the Young's modulus is 7.60%. The variation in terms of ultimate tensile strength of the straight bar A is 2.67%.

In the Figure 6.45, the reported results refer to the tensile test performed on the inclined bar B (the longitudinal axis of the bar is inclined of 30° with respect to the build direction), referring to the results collected by means of a linear deformometer of gauge length of 25 mm positioned on the bar.

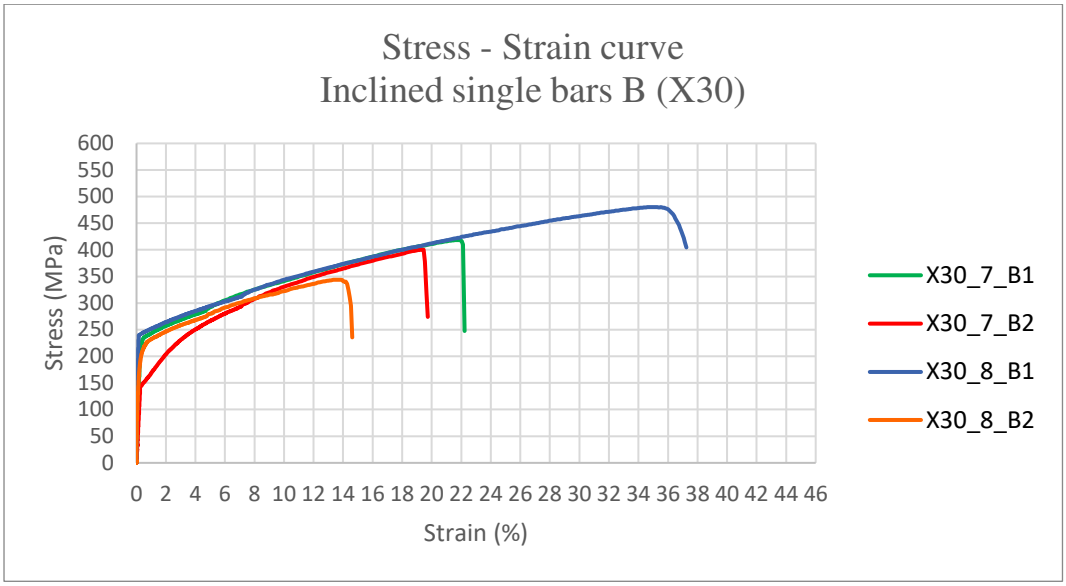

Figure 6.45 Effective stress-strain curves for tensile tests on WAAM single bars tested along the direction B obtained from crossed-bars X30.

A zoom of the effective stress-strain curves of WAAM single bars (for strain lower than 1%) is reported in Figure 6.46 to explore the first part of the tensile test.

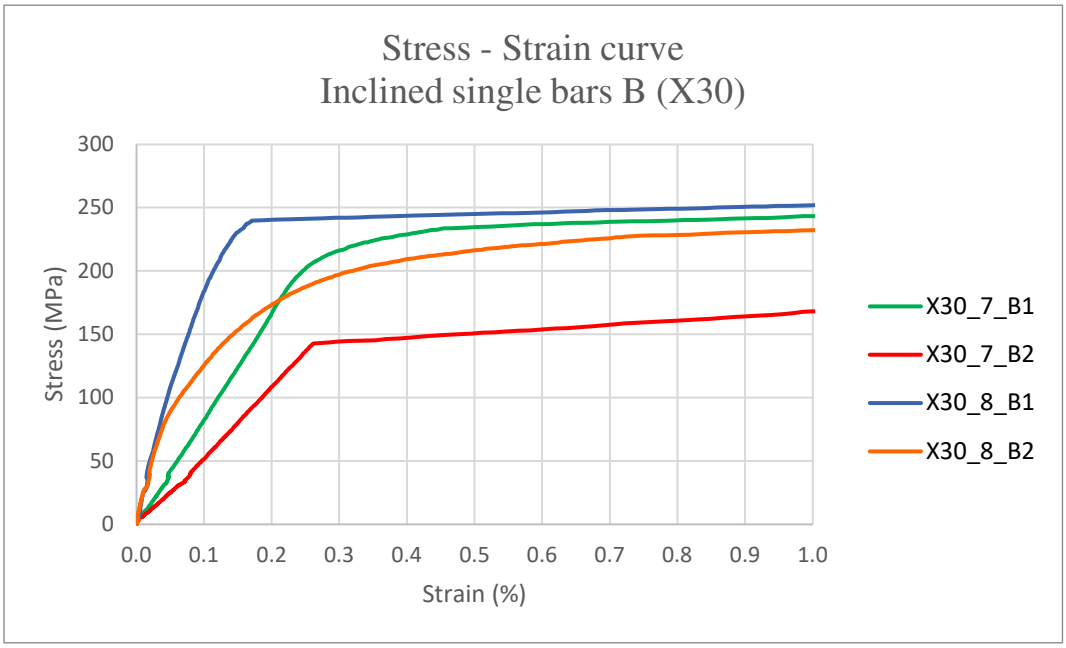

Figure 6.46 A zoom of the effective stress-strain curves (up to 1% strain) for tensile tests on WAAM single bars tested along the direction B obtained from crossed-bars X30.

Young's modulus (E), 0.2% proof stress ($R_{p,02}$), ultimate tensile strength (UTS), elongation to failure ($A_{\%}$) and yield-to-tensile strength ratio ($R_{p,02}$/UTS) were evaluated from the effective stress-strain curves. These main mechanical parameters are reported in Table 6.39.

Inclined bar B	**E**	**Rp,02**	**UTS**	**A%**	**Rp,02/UTS**
	[GPa]	**[MPa]**	**[MPa]**	**[%]**	**[-]**
X30_7_B1	85.36	223.86	418.68	22.21	0.53
X30_7_B2	76.50	140.1	400.78	19.73	0.35
X30_8_B2	175.16	188.76	344.19	14.62	0.55

Table 6.39 Key effective mechanical parameters from tensile tests on WAAM single bars tested along the direction B obtained from crossed-bars X30.

Inclined bar B (X30)		
E_{av}(bar)	**[GPa]**	112.34
UTS_{av} [MPa]	**[MPa]**	411.01

Table 6.40 Mean values of Young's modulus and ultimate tensile strength from tensile tests on WAAM single bars tested along the direction B obtained from crossed-bars X30.

In the Table 6.40, the coefficient of variation of the Young's modulus is 39.67%. The variation is terms of ultimate tensile strength of the inclined bar B is 11.82%.

6.5. Summary of experimental characterization

The results of the tensile tests performed on WAAM crossed-bars and their single bars are analyzed to characterize the behavior of the crossed-bars (straight bar or inclined one with the contribution of the intersection) with respect to the mechanical behavior only related to the single bars, not affected by the intersection.

Firstly, the Table 6.41 reports the values of the average (μ) and coefficient of variation (COV) registered for the key effective mechanical parameters, with a focus on the Young's modulus and ultimate tensile strength values, considering the four inclinations of the bars (straight bar A has the vertical build direction coincident with the longitudinal axis of the bar, inclined bars B with the longitudinal axis of the bar inclined of 10°, 20° or 30° with respect to the vertical build direction).

Specimen	E		UTS	
	μ [GPa]	COV [%]	μ [MPa]	COV [%]
Straight bar A with node	97.00	32.26%	446.13	11.38%
Straight bar A node	129.60	16.65%		
Straight bar A	81.90	27.15%	511.68	5.01%
Inclined bar B (X10) with node	86.72	13.54%	460.53	7.06%
Inclined bar B (X10) node	166.08	9.60%		
Inclined bar B (X10)	76.70	25.46%	575.57	3.06%
Inclined bar B (X20) with node	101.58	12.41%	364.44	18.64%
Inclined bar B (X20) node	185.69	52.60%		
Inclined bar B (X20)	74.09	28.02%	424.21	11.33%
Inclined bar B (X30) with node	105.08	35.54%	327.41	25.47%
Inclined bar B (X30) node	205.16	50.97%		
Inclined bar B (X30)	112.34	39.67%	411.01	11.82%

Table 6.41 Mean values and coefficient of variation of key mechanical parameters from tensile tests (Young's modulus and ultimate tensile strength.) on both WAAM crossed-bars and single bars derived from them.

The values in the Table 6.41 allow some observations regarding the variability of such parameters. Young's modulus values exhibited large coefficient of variation, in the range of 10-50%, especially pointing the attention on the node of the bars and single bars without the node. The latter are the ones that should be compared to the WAAM single bars printed with three different build angles (Section 6.2), which were in the range 20-30%, and they can be assumed in line with these results. The ultimate tensile strength values exhibited coefficient of variation in the range of 7-25% in case of bars with intersection, smaller taking into account the corresponding single bars. In particular, the inclined bars B with the intersection present increasing variabilities associated to an increased inclination of the longitudinal axis with respect to the vertical build direction. In addition, the same can be observed among the inclined single bars without the node, although these present a reduced variability.

The Figures 6.47 and 6.48 compare the key effective mechanical parameters for the four longitudinal axis inclinations of the bars which provide the WAAM crossed-bars, classifying all the straight bars A with the node (the build direction is coincident with the longitudinal axis of the bar) in one batch, and the other inclined bars B with the node (the longitudinal axis of the bar is inclined with respect to the build direction) based on their three different inclinations. Consequently, the four categories are: straight bar A, inclined bars B of 10°, of 20° and of 30°, taken into account for both the straight bars with the intersection and the single bars derived from them, therefore referred to the behavior of WAAM steel bars without any intersection, only referred to the variation of inclination.

The Figure 6.47 reports the histogram in which the mean Young's modulus values are compared, associated to their standard deviation. The average values of Young's modulus exhibit higher values when the computation is performed on the node by means of the linear deformometer placed on it, therefore also the bars with the node exhibits higher values, considering its influence, with respect to the average value computed only on the single bars, considering all the four categories, with the only exception of the 30° inclined bar, although its standard deviation is very high, 37.35 in case of bars with node and 44.57 without it.

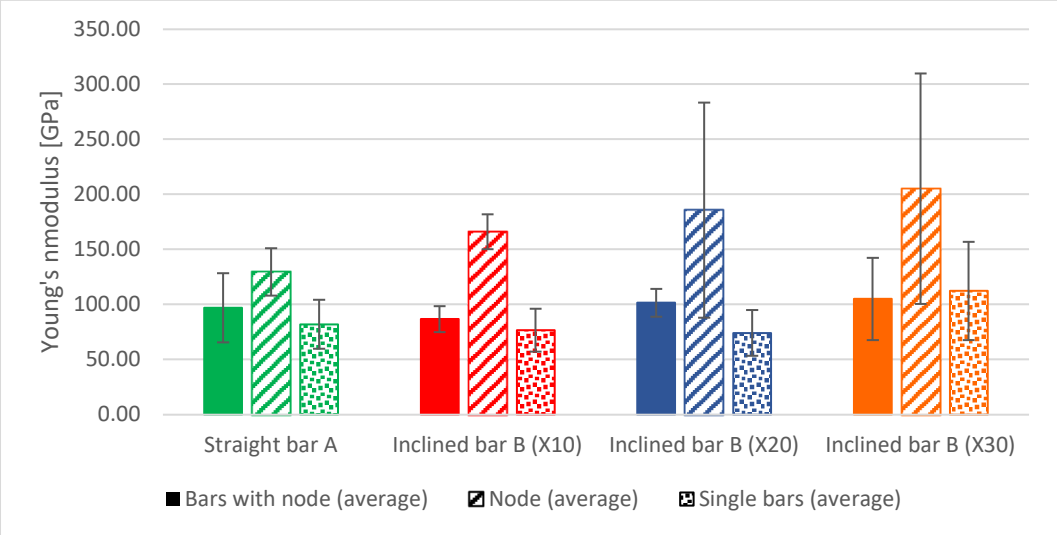

Figure 6.47 Histogram with mean values of Young's modulus (E) derived from the results of the tensile tests on both WAAM crossed-bars and single bars derived from them.

The same is carried out in the Figure 6.48, in which the histogram presents the mean values of the ultimate tensile strength for each of the four categories, associated to their standard deviation. The average ultimate tensile strength values decrease in case of bars with node with respect to the case without it, furthermore, the values decrease with a larger inclination of the longitudinal axis with respect to the vertical build direction, hence proceeding from 10° (X10) up to 30° (X30). In addition, the standard deviation increases for higher inclination, as with the variability. Overall, the bars printed at low build angles, as with straight bars A and inclined bars B of 10°, register good strength properties in terms of ultimate tensile strength.

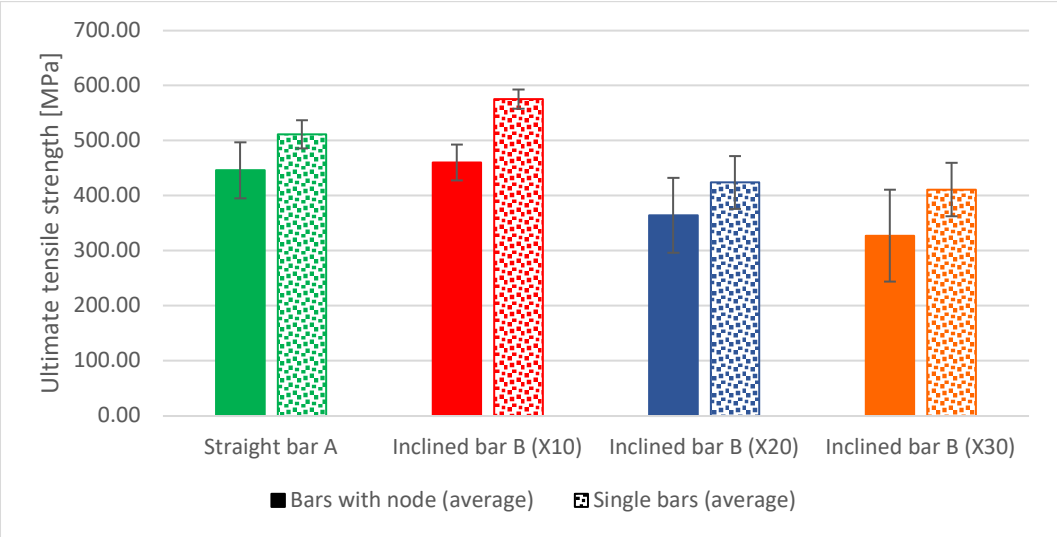

Figure 6.48 Histogram with mean values of ultimate tensile strength (UTS) derived from the results of the tensile tests on both WAAM crossed-bars and single bars derived from them.

The Table 6.42 reports the relative ratios for some key mechanical parameters (Young's modulus and ultimate tensile strength) derived from the results of the tensile tests by means of deformometers, both in case of WAAM-crossed bars in which the deformometer is located on the bar and in case of WAAM single bars realized from the crossed ones. These ratios are evaluated in order to point out the influence on the overall behavior due to the intersection between the two bars of the WAAM crossed-bars. The notation presented in the table refers to the inclination of the bar: A is related to the straight bar, hence with no inclination (X0), instead of B is related to the inclined bar, with the notation of the different batch (X10, X20 and X30). The Young's modulus presents values always larger than 1, with the only exception of the most inclined bar X30, this emphasizes the higher value provided in case of the intersection compared to the case without it. The ultimate tensile strength reports what is already revealed in the histogram, hence how this mechanical parameters decreases with the addition of the intersection, with values of the relative ratio in line considering the different inclinations.

Influence of intersection - ratio of bar with and without it		
Relative ratio	**E**	**UTS**
	[-]	[-]
A (X0)	1.18	0.87
B (X10)	1.13	0.80
B (X20)	1.37	0.86
B (X30)	0.94	0.80

Table 6.42 Relative ratios of the key mechanical parameters (Young's modulus and ultimate tensile strength) with respect to the intersection.

7. Conclusions

The thesis presents the overarching design process from the concept to the fabrication of a diagrid column realized using Wire-and-Arc Additive Manufacturing (WAAM) technology, encompassing the manufacturing constraints proper of WAAM "dot-by-dot" printing strategy, ensuring sufficient structural performances under service load. The WAAM technology was employed for its high-speed printing capabilities, making it adequate to realize large-scaled free forms and shapes without ideally almost any constraints in terms of geometry and dimensions. The diagrid lattice structures ensure geometrical versatility, and using the computational design, by means of algorithmic processes, new structural solutions are generated.

The diagrid structure presents unbalanced outward forces of the internal actions, due to the absence of horizontal hoops at the level of control cross-section, causing secondary bending moments, which increase the stresses in the diagonal bars. The structural verification proves the better structural performances of the final design realized with an "atomized" hyperboloidal shaped column with respect to the "atomized" tubular one.

The subsequent fabrication points out the high role of the adopted printing process parameters in the accuracy of the outcome. The aim is to have an outcome consistent with the digital model, reducing the geometrical and mechanical imperfections.

The efficient use of these WAAM technology to realize diagrid lattice structures require the mechanical characterization of WAAM-produced bars and their intersections, in order to elaborate ad-hoc calibrated partial safety factors for structural design that could properly account for the inherent mechanical variabilities associated to a specific set of WAAM printing parameters. To this aim, the present research was focused also on the mechanical response of "dot-by-dot" WAAM steel bars, as results belonging to an extensive experimental campaign. In particular, the focus was on the mechanical response of as-built "dot-by-dot" WAAM crossed-bars under tensile loading in terms of effective mechanical parameters. The aim was the effect of the intersection on the mechanical

parameters, also referred to different inclinations of the bars constituting the crossed ones. The results of the tensile tests revealed a significant inherent variability of all the key effective mechanical parameters with coefficient of variation values ranging from 7% up to 25% for ultimate tensile strength in case of bars with intersection, instead of from 10% up to 35% for Young's modulus for the same bars. In particular, the average value of Young's modulus is higher in case of intersections with respect to the average value computed on the corresponding single bars, instead of the opposite behavior is shown in case of the average ultimate tensile strength, where the relative ratio between the values related to the bar with the intersection and the one without it exhibits values in line considering the four different inclinations. Furthermore, the ultimate tensile strength values decrease proceeding from an inclination of 10° to 30° of the longitudinal axis of the bar.

References

Adriaenssens, S., Block, P., Veenendaal, D., Williams, C. *Shell Structures for Architecture: Form Finding and Optimization.* Abingdon: Routledge, 2014.

Anton, A., Yoo, A., Bedarf, P., Reiter, L.. Wangler, T., Dillenburger, B. «Vertical Modulations: Computational Design for Concrete 3D Printed Columns.» In *ACADIA 19: Ubiquity and Autonomy. Proceedings of the 39th Annual Conference of the Association for Computer Aided Design in Architecture*, di K., Briscoe, D., Odom, C. Bieg, 596 - 605. Association for Computer Aided Design in Architecture (ACADIA), 2019.

Attaran, M. «The rise of 3-D printing: the advantages of additive manufacturing over traditional manufacturing.» *Bus. Horizon 60(5)*, 2017: 677-688.

Beckh, M. *Hyperbolic Structures: Shukhov's Lattice Towers-Forerunners of Modern Lightweight Construction.* Wiley-Blackwell, 2014.

Bruggi, M., Laghi, V., Trombetti, T. «Simultaneous design of the topology and the build orientation of Wire-and-Arc Additively Manufactured structural elements.» *Comput. Struct.* 242 (2021): 106370.

Buchanan, C., Gardner, L. «Metal 3D printing in construction: A review of methods, research, applications, opportunities and challenges.» *Engineerring Structures* 180 (2019): 332-348.

Buchanan, C., Matilainen, V.P., Salminen, A., Gardner, L. «Structural performance of additive manufactured metallic material and cross-sections.» *J. Constr. Steel Res.* 136 (2017): 35-48.

Buyle, M., Braet, J., Audenaert, A. «Life cycle assessment in the construction sector: A review.» *Renewable and Sustainable Energy Reviews* 26 (2013): 379-388.

Carpo, M. *The Digital Turn in Architecture 1992-2012.* Hoboken: John Wiley & Sons, 2013.

Cascone, F., Faiella, D., Tomei, V., Mele, E. «A Structural Grammar Approach for the Generative Design of Diagrid-Like Structures.» *Buildings* 11, n. 3 (2021).

DebRoy, T., Wei, H.L., Zuback, J.S., Mukherjee, T., Elmer, J.W., Milewski, J.O., Beese, A.M., Wilson-Heid, A., De, A., Zhang, W. «Additive manufacturing of metallic components – process, structure and properties.» *Prog. Mater. Sci.* 92 (2018): 112-224.

Despeisse, M., Ford, S.J. «The role of additive manufacturing in improving resource efficiency and sustainability.» *IFIP Advances in Information and Communication Technology* 460 (2015): 129-136.

Feucht, T., Lange, J. «3-D-printing with steel: Additive manufacturing of connection elements.» *Adv. Eng. Mater. Struct. Syst. Innov. Mech. Appl. - Proc. 7th Int. Conf. Struct. Eng. Mech. Comput. 2019*, 2019: 419–424.

Feucht, T., Lange, J., Waldschmitt, B., Schudlich, A.K., Klein, M., Oechsner, M. «Welding Process for the Additive Manufacturing of Cantilevered Components with the WAAM.» In *Advanced Joining Processes*, di L.F.M., Martins, P.A.F., El-Zein, M.S. da Silva, 67-78. Singapore: Springer Singapore, 2020.

Ford, S., Despeisse, M. «Additive manufacturing and sustainability: an exploratory study of the advantages and challenges.» *Journal of Cleaner Production* 137 (2016): 1573-1587.

Fronius International GmbH, Pettenbach, Austria. «TPS 320i/400i/500i/600i Operating Manual.» s.d.

Galjaard, S., Hofman S. & Ren S. «New Opportunities to Optimize Structural Designs in Metal by Using Additive Manufacturing.» In *Adv. Archit. Geom. 2014*, di P. Block, J. Knippers, N.J. Mitra W. Wang, 79-93. Springer International Publishing, Cham, 2015.

Gao, W., Zhang, Y., Ramanujan, D., Ramani, K., Chen, Y., Williams, C.B., Wang, C.C.L., Shin, Y.C., Zhang, S., Zavattieri, P.D. «The status, challenges, and future of additive manufacturing in engineering.» *Computer-Aided Design* 69 (2015): 65-89.

Gardner, L. & Kyvelou, P. & Herbert, G. & Buchanan, C. «Testing and initial verification of the world's first metal 3D printed bridge.» *J. Constr. Steel Res.* 172 (2020).

Giannatsis, J., Dedoussis, V. «Additive fabrication technologies applied to medicine and health care: a review.» *Int. J. Adv. Manuf. Technol.* 40 (1-2) (2009): 116-127.

Gordon, J.V. & Haden, C.V. & Nied, H.F. & Vinci, R.P. & Harlow, D.G. «Fatigue crack growth anisotropy, texture and residual stress in austenitic steel made by wire and arc additive manufacturing.» *Mater. Sci. Eng. A.* 724 (2018): 431–438.

Grasshopper. s.d. www.grasshopper3d.com.

Guan, K., Wang, Z., Gao, M., Li, X., Zeng, X. «Effects of processing parameters on tensile properties of selective laser melted 304 stainless steel.» *Mater. Des.* 50 (2013): 581–586.

Heimig, T., Kerber, E., Stumm, S., Mann, S., Reisgen, U., Brell-Cokcan, S. «Towards robotic steel construction through adaptive incremental point welding.» *Construction Robotics* 4 (2020): 49-60.

Huang, S.H., Liu, P., Mokasdar, A., Hou, L. «Additive manufacturing and its societal impact: a literature review.» *International Journal of Advanced Manufacturing Technology* 67 (2013): 1191-1203.

Huang, X, Xie, Y.M. «Optimal design of periodic structures using evolutionary topology optimization.» *Structural and Multidisciplinary Optimization* 36 (2008): 597-606.

International, ASTM. «ISO/ASTM 52900:2015: Standard Terminology for Additive Manufacturing Technologies - General Principles - Terminology.» ASTM International, 2015.

ISO6892-1. *Metallic materials - Tensile testing - Part 1: Method of test at room temperature Matériaux méetalliques - Essai de traction - Partie 1: Méthode d'essai à température ambiante COPYRIGHT PROTECTED DOCUMENT.* 2009.

Joosten, S.K. «Printing a Stainless Steel Bridge: an Exploration of Structural Properties of Stainless Steel Additive Manufactured for Civil Engineering Purposes.» *University of Technology Delft*, 2015.

Kanyilmaz, A., Berto, F. «Robustness-oriented topology optimization for steel tubular joints mimicking bamboo structures.» *Mater. Des. \& Process. Commun.* 1, n. 1 (2019).

Keller, J.B. «The shape of the strongest column.» *Arch. Ration. Mech. Anal.* 5 (1960): 275-285.

Khoshnevis, B. «Automated construction by contour crafting - related robotics ans information technologies.» *Autom. ConStruct.* 13 (1) (2004): 5-19.

Kim, I.S., Son, K.J., Yang, Y.S., Yaragada, P.K.D.V. «Sensitivity analysis for process parameters in GMA welding processes using a factorial design method.» *Int. J. Mach. Tools Manuf.* 43 (2003): 763-769.

Krivoshapko, S.N. «Static, vibration, and buckling analyses and applications to one-sheet hyperboloidal shells of revolution.» *Appl. Mech. Rev.* 55 (2002): 241-269.

Kyvelou, P. & Slack, H. & Daskalaki Mountanou, D. & Wadee, M.A. & Ben Britton, T. & Buchanan, C. & Gardner, L. «Mechanical and microstructural testing of wire and arc additively manufactured sheet material.» *Mater. Des.* 192 (2020).

Laghi, V., Gasparini, G., Trombetti, T., Palermo, M. Strucutral pole. Italy Patent IT102021000032411. 12 23, 2021c.

Laghi, V., Palermo, M., Bruggi, M., Gasparini, G., Trombetti, T. «Blended structural optimization approach for Wire-and-Arc Additively Manufactured beams.» *Prog. in Addit. Manuf.*, 2022 (under review).

Laghi, V., Palermo, M., Gasparini, G., Girelli, V., Trombetti, T. «Experimental results for structural design of Wire-and-Arc Additive Manufactured stainless steel members.» *Journal of Constructional Steel Research* 167 (2020b).

Laghi, V., Palermo, M., Gasparini, G., Girelli, V.A., Trombetti, T. «Geometrical characterization of Wire-and-Arc Additive Manufactured steel elements.» *VBRI Press Adv. Mater. Lett.* 10 (2019): 695-699.

Laghi, V., Palermo, M., Gasparini, G., Girelli, V.A., Trombetti, T. «On the influence of the geometrical irregularities in the mechanical response of Wire-and-Arc Additively Manufactured planar elements.» *J. Constr. Steel Res.* 178 (2021b): 1 - 23.

Laghi, V., Palermo, M., Gasparini, G., Trombetti, T. «Computational design and manufacturing of a half-scaled 3D-printed stainless steel diagrid column.» *Addit. Manuf.* 36 (2020a): 101505.

Laghi, V., Palermo, M., Gasparini, G., Trombetti, T. "Flexural mechanical response of Wire-and-Arc Additively Manufactured stainless steel bars." *ASCE Journ. of Struct. Eng.*, 2022 (under review).

Laghi, V., Palermo, M., Silvestri, S., Gasparini, G., Trombetti, T. «Experimental behaviour of Wire-and-Arc Additively Manufactured stainless steel rods.» 2021a: 1-2.

Laghi, V., Palermo, M., Tonelli, L., Gasparini, G., Ceschini, L., Trombetti, T. «Tensile properties and microstructural features of 304L austenitic stainless steel produced by wire-and-arc additive manufacturing.» *Int. J. Adv. Manuf. Technol.* 106 (2020c): 3693–3705.

Laghi, V., Palermo, M., Tonelli, L., Gasparini, G., Girelli, V.A., Ceschini, L., Trombetti, T. «Mechanical response of dot-by-dot wire-and-arc additively manufactured 304L stainless steel bars under tensile loading.» *Constr. Build. Mater.* 318 (2022): 125925.

Liberini, M., Astarita, A., Campatelli, G., Scippa, A., Montevecchi, F., Venturini, G., Durante, M., Boccarusso, L., Minutolo, F.M.C., Squillace, A. «Selection of optimal process parameters for Wire Arc Additive Manufacturing.» *Procedia CIRP* 62 (2017): 470-474.

Lincoln Electric. n.d. https://www.lincolnelectric.com/en/.

Liu, H., Hu, Y. «Welding.» In *Encyclopedia of Materials: Metals and Alloys*. 2022.

Mele, E., Toreno, M., Brandonisio, G., De Luca, A. «Diagrid structures for tall buildings: case studies and design considerations.» *Struct. Des. Tall Spec. Build.* 23 (2014): 124–145.

Montuori, G.M., Mele, E., Brandonisio, G., De Luca, A. «Geometrical patterns for diagrid buildings: exploring alternative design strategies from the structural point of view.» *Eng. Struct.* 71 (2014): 112-127.

Moon, K.S., Connor, J.J., Fernandez, J.E. «Diagrid structural systems for tall buildings: characteristics and methodology for preliminary design.» *Struct. Des. Tall Spec. Build.* 16 (2007): 205-230.

Müller, J. & Grabowski, M. & Müller, C. & Hensel, J. & Unglaub, J. & Thiele, K. & Kloft, H. & Dilger, K. «Design and Parameter Identification of Wire and Arc Additively Manufactured (WAAM) Steel Bars for Use in Construction.» *Metals (Basel)* 9, n. 7 (2019): 725.

MX3D Webpage. *MX3D.* n.d. www.mx3d.com.

Oerlikon. n.d. https://www.oerlikon.com/en/.

Raspall, F., Banon, C., Tay, J.C. «AIRTABLE. Stainless steel printing for functional space frames.» *Comput. Archit. Des. Res. Asia* 1 (2019): 113-122.

Rhinoceros 5. n.d. www.rhino3d.com.

Rodrigues, T.A. & Duarte, V. & Miranda, R.M. & Santos, T.G. & Oliveira, J.P. «Current status and perspectives on wire and arc additive manufacturing (WAAM).» *Materials (Basel)* 12 (2019).

Ryan, E.M., Sabin, T.J., Watts, J.F., Whiting, M.J. «The influence of build parameters and wire batch on porosity of wire and arc additive manufactured aluminium alloy 2319.» *J. Mater. Process. Technol.* 262 (2018): 577-584.

Saadlaoui, Y., Milan, J.L., Rossi, J.M., Chabrand, P. «Topology optimization and additive manufacturing: Comparison of conception methods using industrial codes.» *J. Manuf. Syst.*, 2017.

SAP2000. n.d. www.csiamerica.com/products/sap2000.

Scotti, F. M., Teixeira,F. R., da Silva, L. J., de Araújo, D. B., Reis, R. P., Scotti, A. «Thermal management in WAAM through the CMT Advanced process and an active cooling technique.» *Journal of Manufacturing Processes*, 2020: 23-35.

Selvi, S., Vishvaksenan, A., Rajasekar, E. «Cold metal transfer (CMT) technology - An overview.» 2018.

Silvestru, V., Ariza, I., Vienne, J., Michel, L., Aguilar Sanchez, A. M., Angst, U., Rust, R., Gramazio, F., Kohler, M., Taras, A. «Performance under tensile loading of point-by-point wire and arc additively manufactured steel bars for structural components.» 2021.

Snooks, R., Jahn, G. «Closeness: On the Relationship of Multi-agent Algorithms and Robotic Fabrication.» In *Robotic Fabrication in Architecture, Art and Design 2016*, di D., Saunders, R., Burry, J. Reinhardt, 218-229. Springer International Publishing, 2016.

Song, B., Zhao, X., Li, S., Han, C., Wei, Q., Wen, S., Liu, J., Shi, Y. «Differences in microstructure and properties between selective laser melting and traditional manufacturing for fabrication of metal parts: a review.» *Front. Mech. Eng. China* 10 (2015): 111-125.

Symes, M.D., Kitson, P.J., Yan, J., Richmond, C.J., Cooper, G.J.T., Bowman, R.W., Vilbrandt, T., Cronin, L. «Integrated 3D-printed reactionware for chemical synthesis and analysis.» *Nature Chemistry* 4 (2012): 349-354.

Thomas, C.L., Gaffney, T.M., Kaza, S., Lee, C.H. «Rapid prototyping of large scale aerospace structures.» *IEEE Conference on Aerospace Applications.* Aspen, CO, USA: IEEE, 1996. 219-230.

Thomas, S., Li, Q., Steven, G. "Finite periodic topology optimization with oriented unit-cells." *Structural and Multidisciplinary Optimization 64*, 2021: 1765-1779.

Thompson, M.K., Moroni, G., Vaneker, T., Fadel, G., Campbell, R.I., Gibson, I., Bernbard, A., Schulz, J., Graf, P., Ahuja, B., Martina, F. «Design for Additive Manufacturing: Trends, opportunities, considerations, and constraints.» *CIRP Annals* 65 (2) (2016): 737-760.

Van Bolderen, G.S. «Exploration of Stability of 3D-Printed Steel Members.» *University of Technology Delft*, 2017.

Vantyghem, G., De Corte, W., Shakour, E., Amir, O. «3D printing of a post-tensioned concrete girder designed by topology optimization.» *Autom. Constr.* 112 (2020): 103084.

Wang, H., Du, W., Zhao, Y., Wang, Y., Hao, R., Yang, M. «Joints for treelike column structures based on generative design and additive manufacturing.» *J. Constr. Steel Res.* 184 (2021).

Wang, W., Munro, D., Wang, C.C.L., Van Keulen, F., Wu, J. «Space-time topology optimization for additive manufacturing.» *Struct. Multidiscip. Optim.* 61 (2020): 1-18.

Wang, Z., Palmer, T.A., Beese, A.M. «Effect of processing parameters on microstructure and tensile properties of austenitic stainless steel 304L made by directed energy deposition additive manufacturing.» *Acta Mater.* 110 (2016): 226-235.

Williams, S.W., Martina, F., Addison, A.C., Ding, J., Pardal, G., Colegrove, P. «Wire + Arc Additive Manufacturing.» *Materials Science and Technology* 32 (7) (2016): 641-647.

Wong, K.V., Hernandez, A. «A Review of Additive Manufacturing.» *ISRN Mechanical Engineering* 2012 (2012): 1-10.

Wu, B., Pan, Z., Ding, D., Cuiuri, D., Li, H., Fei, Z. «The effects of forced interpass cooling on the material properties of wire arc additively manufactured Ti6Al4V alloy.» *J. Mater. Process. Technol.* 258 (2018): 97-105.

Wu, W., Xue J., Wang L., Zhang Z., Hu Y., Dong C. «Forming process, microstructure, and mechanical properties of thin walled 316L stainless steel using speed-cold-welding additive manufacturing.» *Metals (Basel)* 9, n. 1 (2019).

Wu, W., Xue, J., Wang, L., Zhang, Z., Hu, Y., Dong, C. «Forming process, microstructure, and mechanical properties of thin-walled 316L stainless steel using speed-cold-welding additive manufacturing.» *Metals (Basel)* 9, n. 1 (2019).

Xiong, J., Li, Y., Li, R., Yin, Z. «Influences of process parameters on surface roughness of multi-layer single-pass thin-walled parts in GMAW-based additive manufacturing.» *J. Mater. Process. Technol.* 252 (2018): 128-136.

Zhou, W., Cao, Z., Zhang, J. «Experiment and analysis on reinforced concrete spatial connection in diagrid tube.» *Struct. Des. Tall Spec. Build.* 25 (2016): 179-192.